This is to certify that the

dissertation entitled

Mechanical Working of $(Al_2O_3)_p$/Al Composite

presented by

Jae Chul Lee

has been accepted towards fulfillment
of the requirements for

Ph.D. degree in Materials Science

K. N. Subramanian

Major professor

Date March 22, 1993

MECHANICAL WORKING OF $(Al_2O_3)_p$/Al COMPOSITE

By

Jae Chul Lee

A DISSERTATION

submitted to

Michigan State University

in partial fullfillment of the requirements

for the degree of

DOCTOR OF PHILOSOPHY

Department of Materials Science and Mechanics

1993

GENERAL ABSTRACT

Mechanical working of $(Al_2O_3)_p$/Al composite

By

Jae Chul Lee

Interface of $(Al_2O_3)_p$/Al composite was characterized using X-ray diffractometry and energy dispersive X-ray spectroscopy. Reaction mechanisms for the formation of the interfacial products were investigated on the basis of the thermodynamic consideration and the experimental observations.

Variations in the elastic and the tensile properties of this composite, as a function of reduction ratio, at cold and hot rolling conditions are presented.

The failure behavior and the property variations are explained on the basis of the microstructural observations. Theoretical modelings developed are able to predict the observed variations in the properties.

Acknowledgement

There are many people without whose help and advice this project could not have been successful.

I would like to take this oppertunity to sincerely thank my Advisor, Dr. K.N.Subramanian, for his guidance and effort during the research. I also wish to acknowledge my graduate committee members, Dr. N.Altiero, Dr. D.S.Grummon, Dr. P.Duxbery, for their contributions. I will always value and remember the warm relationship and the encouragement given to me by Dr. E.D.Case, Dr. K.Mukerjee, and my MSM friends.

Finally, I reserve my deepest and most sincere gratitude to my family members for their endless sacrifice and endurance during my study.

CONTENTS

LIST OF FIGURES

Chapter II.

Chapter III.

Chapter IV

Chapter VII.

Appendix I.

Appendix IV.

Appendix V.

LIST OF TABLES

CHAPTER I

INTRODUCTION

Since the early 1960s, with the impetus of high temperature structural applications, various kinds of metal matrix composites have been investigated by incorporating high strength ceramic materials such as alumina(Al_2O_3), silicon carbide(SiC), and boron carbide(B_4C), either as whiskers or as fibers, into molten metals [1,2]. Most of these studies deal with continuous fiber-reinforced composites. Among those, Al alloy composites reinforced with continuous graphite fiber, SiC fiber, and B_4C fiber were particularly promising for structural applications. Although these composites are as light as aluminum and its alloys, they possess a significant improvement in strength and stiffness [3-9], fatigue resistance [10-12], damping capacity [13], and wear resistance [14,15], in addition to high temperature properties [15-17] as compared to the unreinforced alloys. Particularly, strength and stiffness of SiC fiber reinforced Al-alloy matrix composites (SiC_f/Al composites) are comparable to those of titanium and its alloys [18,19], and enable them to replace titanium forgings. However, the cost of such continuous reinforcements prevent the composites from the practical applications in spite of their attractive mechanical properties to the engineers and designers. In addition, their severe anisotropy in mechanical properties acts as one of the main drawbacks for wider commercial uses. For example, the

transverse strength of these composites are only about 10 % of the longitudianl one. Moreover, it is difficult to fabricate, and shape them into their final configurations.

In 1973, as the new technology for making β-SiC whisker by pyrolizing the rice hull was developed, silicon carbide whiskers (SiC_w) could be made much cheaper, finer, and purer than previous ones. Since then, especially during the early 1980's, discontinuously reinforced metal matrix composites, such as Al alloy composites reinforced with various ceramic particles including SiC, Al_2O_3, and B_4C (in the form of either particulate or whisker), have been studied extensively due to their potential in automotive, structural, and aeronautical applications. In addition, these composites can be manufactured relatively easily and economically using conventional melting and casting techniques. Different types of casting methods have been developed to fabricate these composites; Near-net shapes of track shoes and pistons could be produced by using squeeze casting method [20]. The basic principle of the squeeze casting is to forge a liquid composite into a closed die to reduce the porosity due to the shrinkage and gas, and to make the products solidify rapidly under high pressure of 50 to 100 MPa. Rheocasting (or compocasting), which consists of vigorously agitating a semisolid composite before casting [21] have been proven to be effective in increasing the volume fraction of the reinforcement within the composite without serious flocculation.

Recently, it has been found that nearly all commercially important ceramic reinforcements including SiC and Al_2O_3 show a poor wettability by molten aluminum and its alloys [23-26]. As a result of the poor

wettability of ceramic particles by molten matrix alloys, the direct incorporation of such reinforcements into molten aluminum alloys causes flocculation. Under such conditions, extensive clusterings or agglomerations of the reinforcements can occur due to surface tension effects. This phenomenon becomes more significant as the particle size becomes smaller than 40 μm [27,28], and the difference in density between the matrix alloy and reinforcements becomes larger [15]. Such clusters of the reinforcements not only cause poor overall mechanical properties and machinability [28], but also result in anisotropy of particulate-reinforced composites in their as-manufactured state and prohibit their wider use for practical applications. If the distribution of the reinforcements can be made more uniform, more isotropic properties can be achieved.

Various processing techniques have been developed to overcome this problem. The following methods have been found to be effective in preventing significant particulate clusters or agglomerations in aluminum alloy matrix.

1) **Matrix modification** by adding some alloying elements, such as Li, Cu, Si, or Mg, has been proved to be effective in improving the wettability of the reinforcements with the molten matrix [14,27,29-35].
2) **Preheating** the reinforcements before introducing into molten matrix allows their uniform distribution in the matrix [31,33,36,37].
3) **Coating of particulates**, such as graphite or alumina with Ni or Cu, can improve their wettability by the molten aluminum alloys [38-40].

For further understanding of the mechanical behavior of particulate reinforced aluminum alloy composites, the factors contributing the tensile properties, important operating strengthening mechanisms, and the experimentally observed behaviors are provided in APPENDIX I. and II.

Unlike polymer matrix composites and continuous fiber reinforced composites, which are usually formed into the final shapes, metal matrix composites containing discontinuous reinforcements can be shaped into their final configurations by using the conventional mechanical workings such as forging, extrusion, and rolling, etc. Such components as the connecting rod for internal combustion engine, and compressor blade were successfully forged from bar stock which was extruded from a cast billet [22]. Since such mechanical working to obtain the final shape can alter the size, shape, and distribution of clustered reinforcements, all these parameters are expected to have influence on the mechanical properties of the resultant composite system. Thus, **Mechanical working** of the composites can be used as another means for providing the uniform distribution of particulate reinforcements.

Although significant number of investigations have been focussed on the characterization of the interface [43-46], mechanical properties at room and elevated temperatures[47,48], and various processing techniques [49,50] of such composites, relatively few studies [6,18,41,43] have been carried out to study the effects of mechanical working on the tensile and the elastic properties of the particulate reinforced aluminum alloy.

The objectives of the research are to investigate

1) the failure behavior of the particulate reinforced aluminum alloy under uniaxial tension,
2) the effect of both cold and hot rolling on the elastic and the tensile properties of the aluminum alloy reinforced with Al_2O_3 particulates,
3) interface characterization, and the role of the interface on the tensile properties of the aluminum alloy reinforced with Al_2O_3 particulates, and
4) the effects of texture, particulate cracking, interfacial debonding, and grain size that result due to mechanical working on the elastic properties.

The rest of this dissertation consists of the paper publications and the format adopted in this dissertation is to maintain the integrity of the individual publications.

REFERENCES

1. I.Ahmad, V.P.Greco and J.M.Barranco, "Reinforcement of nickel with some high strength filament", J. Composite Materials, 1, 19, (1967).

2. E.G.Wolff, "Hydrodynamic Alignment of discontinuous Fibers in a Matrix" Fiber Science and Technology, Elsevier publishing co. Essex. England, (1969).

3. N.Tsangarakis, B.O.Andrews and C.Cavallaro, "Mechanical properties of some silicon carbide reinforced aluminium composite", J. Composite Materials, 21, 481-492, (1987).

4. T.G.Nieh and D.J.Chellman, "Modulus measurements in discontinuous reinforced aluminium composites", Scr. Metall., 18, 925-928, (1984).

5. R.J.Arsenault and S.B.Wu, "A comparison of PM vs. melted SiC/Al composites", Scr. Metall., 22, 767-772, (1988).

6. R.J.Arsenault, "The strength of aluminium alloy 6061 by fibre and platelet silicon carbide", Mat. Sci. Eng., 64, 171-181, (1981).

7. Y.Flom and R.J.Arsenault, "Interfacial bond strength in an aluminium alloy 6061-SiC composites", J. Metals, 38, 31-34, (7.1986).

8. V.C.Nardone, "Assessment of models used to predict the strength of discontinuous silicon carbide reinforced aluminium alloys", Scr. Metall., 21, 1313-1318, (1987).

9. R.H.Jones, C.A.Lavender and M.T.Smith, "Yield strength-fracture toughness relationship in metal matrix composites", Scr. Metall., 21, 1565-1570, (1987).

10. W.A.Longsdon and P.K.Liaw, "Tensile, fracture toughness and fatigue crack growth rate properties of silicon carbide whisker and particulate reinforced aluminium metal matrix composites", Engineering Fracture Mechanics, 24, NO.5, 737-751, (1986).

11. T.Christman and S.Suresh, "Effects of SiC reinforced and aging treatment on fatigue crack growth in an Al-SiC composites", Mat. Sci. Eng., 102, 211-216, (1988).

12. J.K.Shang, W.Yu and R.O.Ritchie, "Role of silicon carbide particles in fatigue crack growth in SiC particulate reinforced aluminium alloy composites" Mat. Sci. Eng., 102, 181-192, (1988).

13. H.J.Heine, "Cast aluminium metal matrix composites are here", Foundary management & technology, 116, 25-30, (7.1988).

14. F.M.Hosking, F.F.Portillo, R.Wunderlin and R.Mehrabian, "Composites of aluminium alloy : fabrication wear behavior", J. Mater. Sci., 17, 477-498, (1982).

15. F.A.Girot,J.M.Quenisset and R.Naslain, "Discontinuously reinforced aluminium matrix composites", Composite Science and Technology, 30, 155-184, (1987).

16. V.C. Nardone and J.R. Strife, "Analysis of the creep behavior of silicon carbide reinforced 2124 Al (T4)" Metall. Trans. A, 18, 109-114, (1987).

17. K.S.Ravichandran and E.S.Dwarakadass, "Advanced aerospace Al alloy" J. Metals, 39, 28-32, (6.1987).

18. F.Dolowy, "Increasing focus on silicon carbide reinforced aluminium composites", Light Metal Age, 44, 7-14, (6.1986).

19. D.Hughes, "Textron unit makes reinforced titanium, aluminium parts", Aviation week and space technology, 129, 91-95, (11.1988).

20. M.A.H.Howes, "Ceramic reinforced MMC fabricated by squeeze casting", J. Metals, 38, 28-29, (3.1986).

21. F.A.Girot, L.Albingre, J.M.Quenisset and R.Naslain, "Rheocasting Al matrix composites", J. Metals, 39, 18-21, (11.1987).

22. T.R.Pritchett, "Advenced technology aluminium materials for aerospace application", Light metal age, 44, 10-14, (10.1986).

23. A.Mortensen, J.A.Cornie, and M.C.Flemings, "Solidification prossing of metal matrix composites", J. Metals, 40, 12-19, (1988).

24. T.Choh and T.Oki, "Wettability of SiC to aluminium and aluminium alloys", The Institute of Metals, 378-385, (1987).

25. V.Laurent, D.Chatain and N.Eustathopoulus, "Wettability of SiC to aluminium and Al-Si alloys", J. Mater. Sci., 22, 244-250, (1987).

26. A.Banergi and P.Rohatgi, "Cast aluminium alloy containing dispersions of TiO_2 and ZrO_2 particles", J. Mater. Sci., 17, 335-342, (1982).

27. S.Deonath, R.Bhatt and P.Rohatgi, "Preparation of cast aluminium alloy-mica particle composites", J. Material Science, 15, 1241-1251, (1980).

28. G.Mott and P.K.Liaw, "Correlation of mechanical and ultrasonic properties of Al-SiC metal matrix composites", Metall. Trans. A, 19, 2233-2246, (1988).

29. B.C.Pai, S.Pay, K.V.Prabhakar and P.K.Rohatgi, "Fabrication of aluminium - alumina (magnesia) particulate composites in foundaries using magnesium addition to the metals", Mat. Sci. Eng., 24, 31-44, (1976).

30. P.K.Rohatgi, B.C.Pai and S.C.Panda, "Preparation of cast aluminium -silica particulate composites", J. Mater. Sci., 14, 2277-2283, (1979).

31. M.K.Surrapa and P.K.Rohatgi, "Preparation and properties of cast aluminium - ceramic composites", J. Mater. Sci., 16, 983-993, (1981).

32. T.W.Clyne, M.G.Bader, G.R.Cappleman and P.A.Hubert, "The use of δ-alumina fibre for metal matrix composites", J. Mater. Sci., 20, 85-96, (1985).

33. C.G.Levi, G.J.Abbaschian, and R.Mehrabian, "Interface reactions during fabrication of aluminum alloy-alumina composites" Metall. Trans. A, 9, 697-711, (1978).

34. D.Webster, "Effect of Lithium on the mechanical properties and microstructure of SiC whisker reinforced aluminum alloy" Metall.Trans. A, 13, 1511-1519, (1982).

35. V.Laurent, D.Chatain, and N.Eustathopoulous, "Wettability of SiC by aluminum and Al-Si alloys", J. Mater. Sci., 22, 244-250, (1987).

36. B.P.Krishman, M.K.Surrpa, and P.K.Rohatgi, "The UPAL process : a direct method of preparing cast aluminium alloy - graphite particle composites", J. Material Science, 16, 1209-1216, (1981).

37. T.P.Murali, M.K.Surrapa, and P.K.Rohatgi, "Preparation and properties of Al-alloy coconut shell char particulate composites", Metall. Trans. B, 13, 485-494, (1982).

38. P.K.Rohatgi, B.C.Pai, and S.C.Panda, J. Mater. Sci. Lett., 15, 1558-1592, (1980).

39. R.L.Mehan, "Fabrication and properties of mechanical Sapphire whisker - aluminum composite", J. Comp. Mat., 4, 90-101, (1970).

40. R.Mehrabin, R.G.Riek,and M.C.Flemings, Metall. Trans. A, 5, 1899-1905, (1974).

41. T.G.Nieh and R.F.Karlak, "Hot-rolled silicon carbide - aluminium composites", J. Mater. Sci. Lett., 2, 119-122, (1983).

42. J.R.Picken, T.J.Langan, R.O.England, and M.Liebson, "A study of the hot working behavior of SiC - Al alloy composites and their matrix alloys by hot torsion testing", Metall. Trans. A, 18, 303-312, (1987).

43. K.Kannikeswaran and R.Y.Lin, "Trace element effects on Al-SiC interface", J. Metals, 39, 17-19, (9.1987).

44. R.J.Arsenault, "Interface in metal matrix composites", Scr. Metall., 18, 1131-1134, (1984).

45. T.Iseki, T.Kameda, and T.Murayama, "Interfacial reactions between SiC and aluminium during joining", J. Mater. Sci., 19, 1692-1698, (1984).

46. S.G.Fishman, "Interface in composites", J. Metals, 38, 26-27, (3.1986).

47. S.V.Nair, J.K.Tien, and R.C.Bates, "SiC-reinforced aluminum metal matrix composites", International Metals Review, 30, No.6, 275-290, (1985).

48. D.L.McDanels, "Analysis of stress-strain, fracture, and ductility behavior of aluminum matrix composites containing discontinuous silicon carbide reinforcement", Metall. Trans. A, 16, 1105-1115, (1985).

49. R.J.Arsenault and S.B.Wu, "A comparision of PM vs. melted SiC/Al composites", Scr. Metall., 22, 767-772, (1988).

50. W.R.Hoover, "Commercialization of Duralcan aluminum composites", Proceedings of the fifth annual ASM/EDS advanced composites conference, Detroit, Michigan, Oct. 1989, 211-217, published by ASM International, Materials Park, Ohio, (1989).

CHAPTER II.

INTERFACE IN Al_2O_3 PARTICULATE REINFORCED ALUMINUM ALLOY COMPOSITE AND ITS ROLE ON THE TENSILE PROPERTIES.

This chapter is based on the paper that has been submitted to Journal of Materials Science. The following is the abstract from the original paper.

The interface characterization of the Al alloy reinforced with Al_2O_3 particulates [$(AL_2O_3)_p$/Al composite] was performed using X-ray diffractometry and energy dispersive X-ray spectroscopy. Layer of $MgAl_2O_4$ single crystals was observed at $(Al_2O_3)_p$/Al interface in the as-received extruded composites. Such $MgAl_2O_4$ formed at the surface of $(Al_2O_3)_p$ are believed to grow by consuming some amount of $(Al_2O_3)_p$. Upon loading, interfacial debonding was observed to occur at the boundary between $MgAl_2O_4$ and the Al alloy, or along the $MgAl_2O_4$ layer itself. These experimental observations are correlated with the tensile properties of such composites.

1. INTRODUCTION

Interfacial characteristics can be considered as one of the most important factors in determining the mechanical properties of composites, since strong interfacial bond is essential for the effective load transfer from matrix to reinforcement to achieve higher strength of the composites. Such a strong bond is usually achieved by the formation of adequately thin reaction layer at the interface under favorable wetting condition of the molten matrix onto the reinforcement. However, it has been reported that nearly all commercially important ceramic reinforcements, including SiC, Al_2O_3, B_4C, etc., exhibit poor wettability by molten matrix [1-6]. Molten pure Al does not wet Al_2O_3 even at 900°C [7,8]. Addition of alloying elements, such as Li or Mg, has proved to be an effective method to enhance the wettability of the ceramic reinforcements by the molten matrix. Some of these alloying elements can react with the reinforcements to produce chemical reaction products at the interface, which might be either beneficial or undesirable for the composite strengthening. For example, the formation of a thick intermetallic compound layer at the interface will cause crack initiation at the interface (i.e. interfacial debonding) upon loading due to the stress concentration at the brittle interface, resulting in low strength and ductility of the composite. In contrast, interfacial bond can be improved by the formation of spinels, which is believed to promote the bond strength between metals and ceramics [9,10].

Significant studies, using electron diffraction [7,11-14], Auger spectroscopy [7,9], and energy dispersive X-ray spectroscopy (EDS)

[9,12,14], have been carried out to characterize the structure and the chemistry of the interface in the Al alloy composites reinforced with Al_2O_3 fiber. Although the interfacial bond in these composites was found to be achieved by the formation of $MgAl_2O_4$ spinel [7,9-15], studies to demonstrate the detailed morphology of $MgAl_2O_4$ and the structure of the reaction layer have not yet been reported in the literature. The aim of the present study is to characterize the interfacial reaction layer in $(Al_2O_3)_p$/Al composite, and to investigate its influence on the resultant tensile properties.

2. EXPERIMENTAL PROCEDURES

2.1 Material

Cast Duralcan composite (W6A 10A), 6061 aluminum alloy reinforced with 10 % of $(Al_2O_3)_p$, and obtained as extruded cylindrical bars with a diameter of 2", was used for the present study. The composite was T6 heat treated prior to the microstructural studies and tensile testing. Details of the heat treatment procedures used are as follows:

a. Solution treatment: 560°C x 1 hr.

b. Room Temperature aging : 24°C x 65 hrs.

c. Artificial aging: 170°C x 14 hrs.

2.2 Sample preparation and Microstructural studies

The heat treated specimens were polished with diamond compound on a lapping wheel. The polished surfaces were then etched lightly with dilute Keller's regent to reveal the outer contours of the interface and the precipitates in the matrix. The interface region in the polished surfaces and the fracture surface of the fractured tensile test specimens were examined using SEM and EDS. X-ray line scanning across the interface, and X-ray dot mapping of the interfacial region, were performed using EDS operated at 15 KV.

Electrochemical dissolution, with 33% HNO_3 - 67% Methanol, was employed to dissolve away the conductive Al matrix along with the precipitates, such as $CuAl_2$, Mg_2Si, etc, present within the matrix. This process helped to obtain the nonconductive phases present at the interface for further study. The crystal structures of these phases

were determined by X-ray diffractometry. Since the volume fraction of the reaction product layer at the interface is relatively small as compared to that of $(Al_2O_3)_p$, a slow scan speed (0.4°/Min) was used to obtain sharp and strong enough X-ray diffraction peaks corresponding to the reaction products formed at the interface. (Direct X-ray scanning of the composite surface was not effective for identifying the interfacial reaction products due to their small volume fraction in the composite). The detailed morphologies of $(Al_2O_3)_p$ and the reaction products at the interface were examined using SEM.

Tensile testing of dog-bone type specimens, cut out from the composite, were carried out using an Instron with a constant cross-head speed (1cm/min) at room temperature. The fracture surfaces, and side surfaces of the fractured tensile test specimens, were examined using SEM to understand the fracture behavior exhibited by such composites. Observations made on the fracture surfaces of the tensile tested specimens, and on the surfaces of electropolished composite scratched with a metal scriber, helped to identify the phase boundary where interfacial debonding occurred.

3. RESULTS AND DISCUSSION

3.1 Interface characterization

The SEM image obtained from the polished surface, as shown in Fig.1(a), clearly shows the interfacial reaction layer as well as the precipitates in the matrix. Such a reaction layer can also be observed from the fracture surfaces of the tensile test specimens, as shown in Fig.1(b). The jagged shape of the interface region can be seen clearly from both these micrographs. EDS analyses employed on this interfacial region (Fig.2) shows relatively strong Mg peak as well as noticeably weak Si peak, indicating that the interfacial reaction products consist of Mg and Si.

Electrolytic polishing of the specimens, carried out to reveal the individual $(Al_2O_3)_p$ showed the detailed shape of $(Al_2O_3)_p$. These $(Al_2O_3)_p$ have a blocky platelet shape with an aspect ratio of about 2, and are either fully or partially covered with small crystals, as shown in Fig.3. The results obtained from the X-ray diffractometry (Fig.4) show that the type of $(Al_2O_3)_p$ is α-Al_2O_3 having corundum structure, and the small crystals formed at the surface of $(Al_2O_3)_p$ are $MgAl_2O_4$ with spinel structure. As can be seen in the magnified views of individual $(Al_2O_3)_p$ given in Figs.5 and 6, $MgAl_2O_4$ formed at the surface of $(Al_2O_3)_p$ are pyramid-like (or octahedral-shaped) crystals with an average size of about 1 μm. Based on the shape of these individual $MgAl_2O_4$ spinel regions, they are believed to be single crystals. The micrographs also reveal that the roots of $MgAl_2O_4$ are located well below the surface of $(Al_2O_3)_p$. Furthermore, it is noted that the inner surface contour of Al_2O_3, which surrounds

each $MgAl_2O_4$ crystal, matches the outer contour of the $MgAl_2O_4$. Such microscopic features, as can be seen in Figs.5(a) and 6, indicate that these crystals might have grown at Al_2O_3 substrates at the expense of some amount of Al_2O_3. Infrequently, however, some $MgAl_2O_4$ crystals have been found in the matrix near $(Al_2O_3)_p$, as shown in Fig.7. Such a microscopic feature indicates strong interfacial bond between $MgAl_2O_4$ (spinel) and Al_2O_3 (corundum). The fracture surfaces of $(Al_2O_3)_p$ reveal the well-bonded interface between Al_2O_3 and $MgAl_2O_4$ (Fig.8).

Fairly thick $MgAl_2O_4$ layer, about 1 μm thick, observed at the interfacial region is probably due to prolonged contact between $(Al_2O_3)_p$ and the molten Al during manufacture of the composite. X-ray dot mapping [Fig.9(a)] and line scanning across the interface [Fig.9(b)] were carried out on $(Al_2O_3)_p$/Al composite using EDS in this study. Strong X-ray signal indicating the presence of Mg near the interface observable in Fig.9(a), is due to the $MgAl_2O_4$ layer.

Si has been reported to be present either in the form of Mg_2Si precipitates near the interface, or as Si rich amorphous layer, in these composites [11-14,16]. The presence of Si at the interfacial region could not be clearly noted from the results obtained using elemental X-ray dot mapping (due to its slightly higher contribution as compared to the matrix) as shown in Fig.9(a). However, the corresponding line scanning pattern across the interface shows the presence of small amount of Si at the interface region, as shown in Figs.2 and 9(b). The techniques employed in this study could not characterize the Si-containing phase, segregated at the interface.

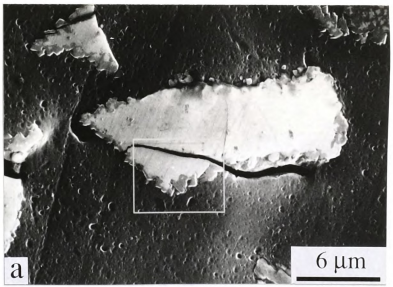

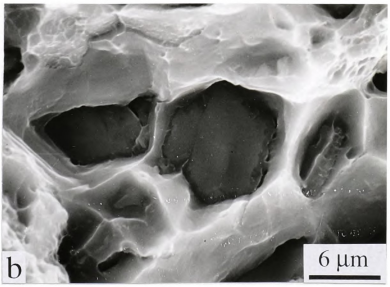

Fig.1(a) Micrograph taken from the polished surface. The reaction layer at the interface, and some precipitates in the matrix can be seen. The crack inside the region marked by the rectangle is due to the tensile loading applied in a direction indicated by the arrow. Note that the crack formed within the particulate propagates around the reaction layer.

(b) Micrograph taken from the fracture surface. The jagged reaction layer is evident at the interface. Smooth fracture surface of $(Al_2O_3)_p$ indicates that $(Al_2O_3)_p$ probably is single crystal.

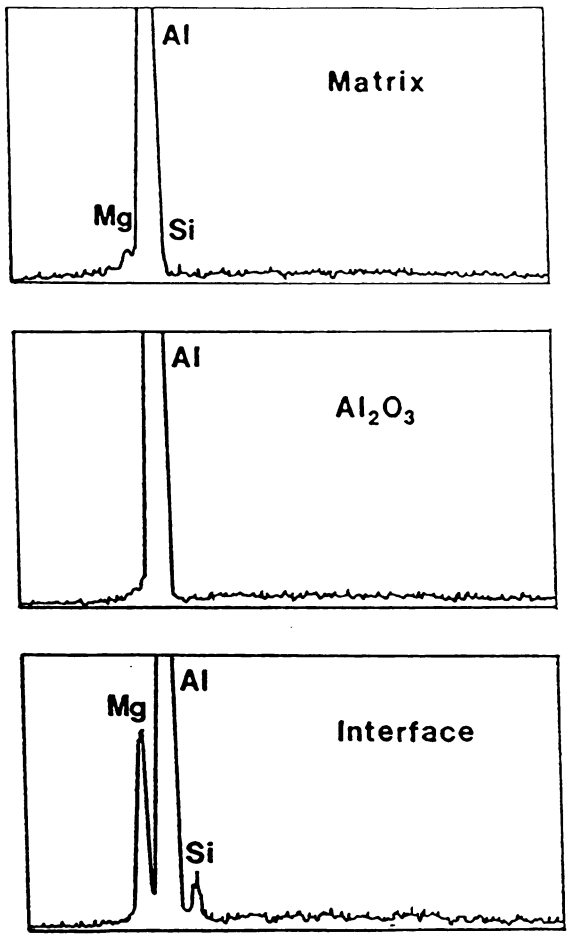

Fig.2 EDS analyses of
a) matrix b) $(Al_2O_3)_p$ and c) interfacial region.

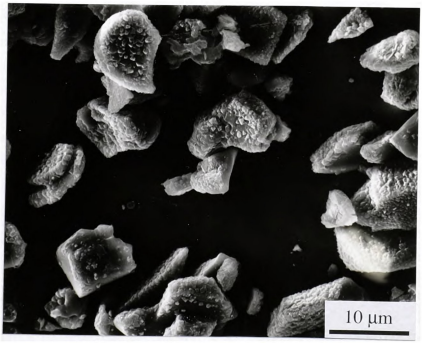

Fig.3 Surface of $(Al_2O_3)_p$/Al composite showing individual $(Al_2O_3)_p$. Most $(Al_2O_3)_p$ are fully, and some partially, covered with small crystals. (Electrolytic polishing was carried out to remove the conductive matrix)

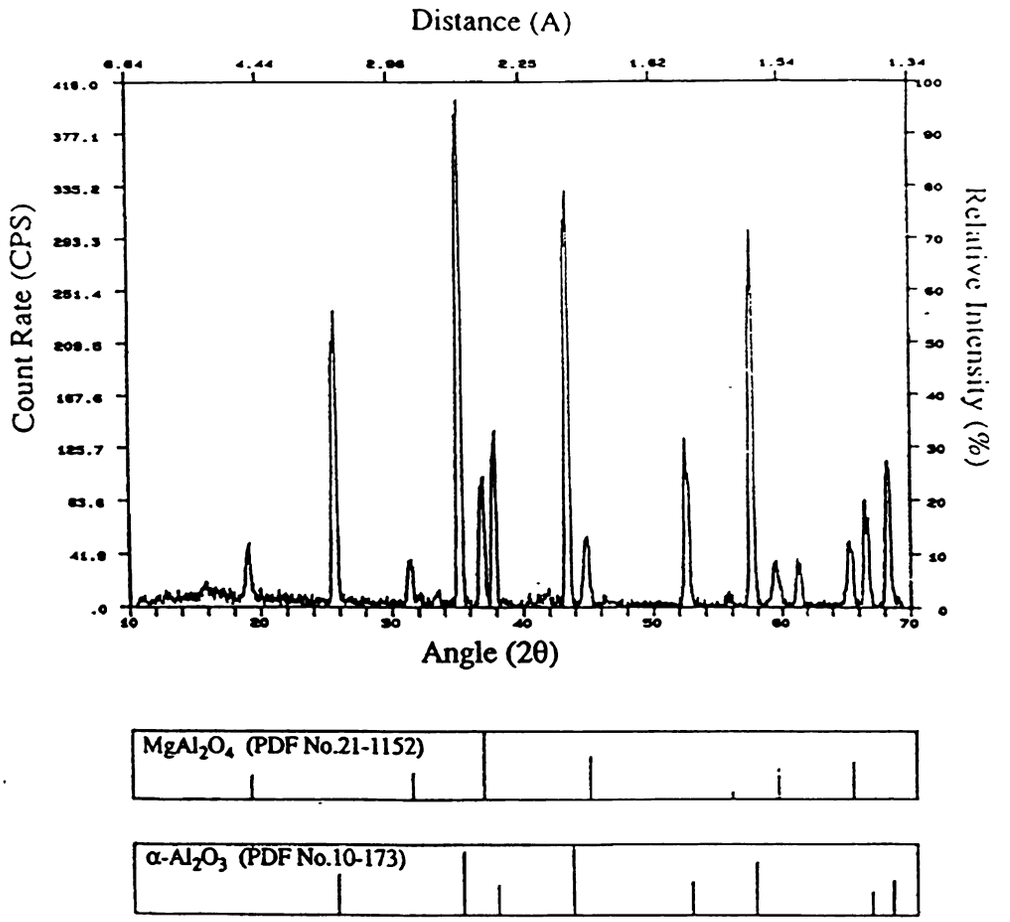

Fig.4 X-ray diffraction peaks indicating that the type of the reinforcement is α-Al_2O_3 and the crystals formed at the surface of Al_2O_3 are spinel ($MgAl_2O_4$).

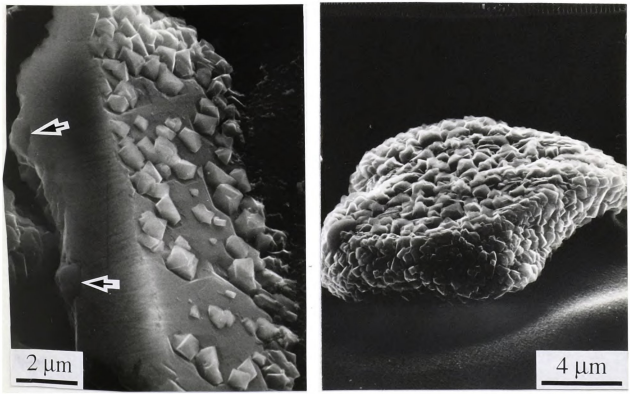

Fig.5(a) $(Al_2O_3)_p$ partially covered with $MgAl_2O_4$. The roots of the crystals are embedded in Al_2O_3 at locations indicated by the arrows. The flat surface on $(Al_2O_3)_p$ is due to mechanical polishing, and the dark background is the matrix.

(b) $(Al_2O_3)_p$ fully covered with $MgAl_2O_4$ crystals.

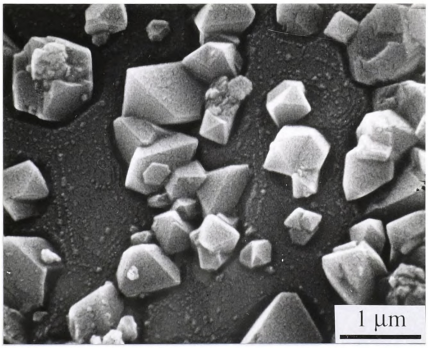

Fig.6 $MgAl_2O_4$ single crystals, grown at the surface of $(Al_2O_3)_p$, observed at a higher magnification (X20,000). Notice the groove around individual $MgAl_2O_4$ crystals at regions indicated by the arrows. The flat dark background is the surface of $(Al_2O_3)_p$.

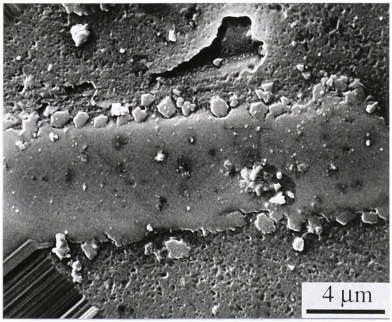

Fig.7 $MgAl_2O_4$ crystals infrequently formed in the vicinity of $(Al_2O_3)_p$.
Note that $MgAl_2O_4$ crystals, similar to the one indicated in the figure, are not in contact with $(Al_2O_3)_p$.

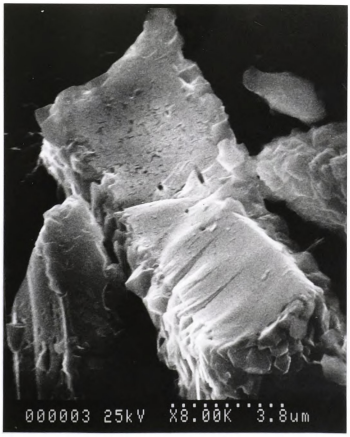

Fig.8 The river patterns extending from $MgAl_2O_4$ to Al_2O_3 on the fracture surface of $(Al_2O_3)_p$ illustrate the existence of well-bonded interface between Al_2O_3 and $MgAl_2O_4$.

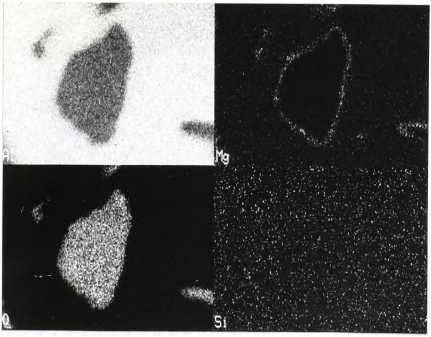

Fig.9(a) Elemental X-ray dot maps obtained from the particulate and interfacial region. The presence of Si at the interfacial region is not clear since the concentration of Si in this region is only slightly higher than that in the matrix.

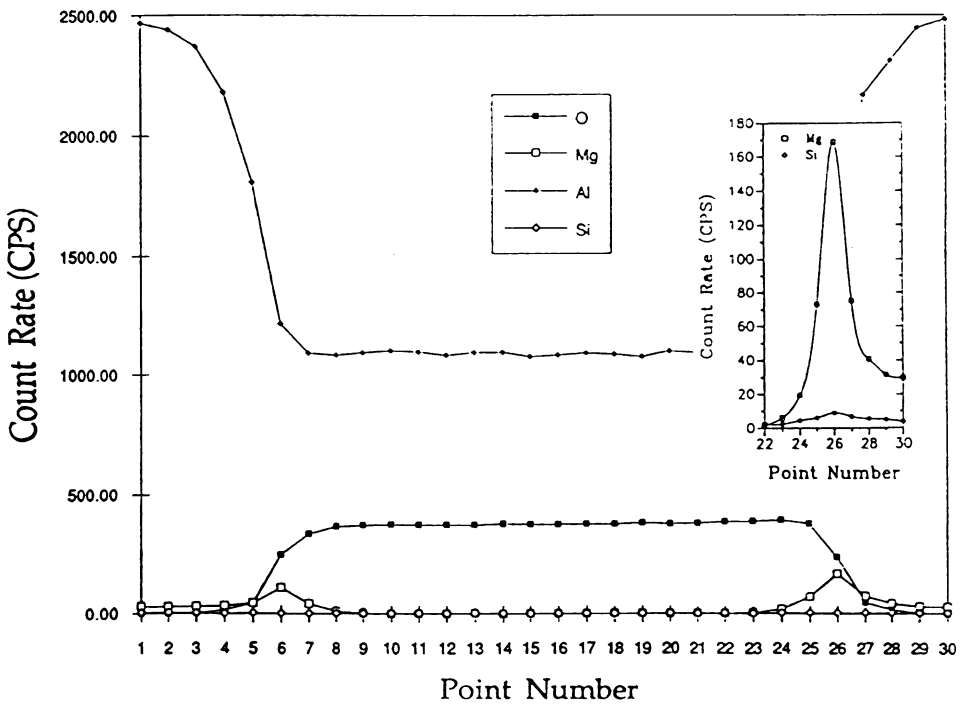

Fig.9 (continued)
(b) EDS line scans for Al, O, Mg, and Si across the interface. Line scans was carried out for 30 different points at intervals of 0.375 μm.

3.2 Formation of the interfacial products

Based on thermodynamic considerations, following reactions have been suggested for the formation of the $MgAl_2O_4$ at the $(Al_2O_3)_p$/Al interface in this type of composite [9,11,12,15]:

$$\{Mg\} + 2\{Al\} + 2\{O_2\} = [MgAl_2O_4] \quad (1)$$

$$[MgO] + [Al_2O_3] = [MgAl_2O_4] \quad (2)$$

$$\{Mg\} + \frac{4}{3}[Al_2O_3] = [MgAl_2O_4] + \frac{2}{3}\{Al\} \quad (3)$$

$$2[SiO_2] + 2\{Al\} + \{Mg\} = [MgAl_2O_4] + 2\{Si\} \quad (4)$$

where the symbols { } and [ ] in above equations correspond to those in solution in the melt and those present as solid phase in the melt, respectively. All of the reactions listed above have large enough thermodynamic driving forces for the formation of $MgAl_2O_4$ spinel.

Although both the phase boundary and the grain boundary regions provide heterogeneous nucleation sites, most of the $MgAl_2O_4$ crystals were found to be present mainly at the $(Al_2O_3)_p$/Al phase boundary. Based on this observation, reaction (1) seems to be less likely. Reaction (2) has to occur as a solid state reaction between two ceramic materials, which kinetically will be very slow [9].

The micrographs given in Figs.5(a) and 6, indicate that $MgAl_2O_4$ crystals usually have their roots embedded into $(Al_2O_3)_p$ and appear to have been formed by consuming some amount of Al_2O_3. Presence of grooves around the $MgAl_2O_4$ crystals, existing at the surface of

$(Al_2O_3)_p$ obtained by electrochemical dissolution, may correspond to pure Al resulting from this reaction that have been dissolved during electrochemical dissolution. Such observations tend to favour reaction (3).

However, reaction (4), which describes the formation of $MgAl_2O_4$ in the absence of Al_2O_3 substrate, is a possible mechanism that can explain the observed presence of Mg and Si near the interface. Presence of some $MgAl_2O_4$ crystals in the matrix region near the interface, as shown in Fig.7 may be due to reaction (4). The source of SiO_2 required for this reaction may arise from Si and O_2 present in the molten Al.

On the basis of the microscopic observations, reaction (3) is believed to be the most likely mechanism for the formation of the $MgAl_2O_4$ layer at the interface, since the features supporting it have been observed much more frequently than those supporting reaction (4).

3.3 Role of the interface on the tensile properties

Several studies have been carried out to investigate the failure behavior of metal matrix composites reinforced with ceramic particulates [17-19]. Based on these studies, the low ductility exhibited by such composites can be attributed to 'particulate cracking' and 'interfacial debonding' that occur upon loading. A typical fracture surface of $(Al_2O_3)_p$/Al composite showing these significant microscopic features are given in Fig.10.

Particulate cracking [Fig.11(a)], which acts as a dominant failure mechanism operative in this composite, occurs as a result of the stress concentration at $(Al_2O_3)_p$ under the applied tension [19]. The jagged edges of $(Al_2O_3)_p$, produced as a result of the severe interfacial reaction, will cause stress concentration and aid particulate cracking.

In addition to particulate cracking, significant amount of interfacial debonding could be observed at the side-surfaces of the fractured tensile test specimens. Since a distinct $MgAl_2O_4$ layer, with a thickness of about 1 μm was found to be present at $(Al_2O_3)_p$/Al interface, interfacial debonding can occur either at

i) $(Al_2O_3)_p/MgAl_2O_4$ phase boundary,

ii) $MgAl_2O_4$/Al phase boundary, or

iii) $MgAl_2O_4$ layer itself (by fracturing individual crystals).

Among them, the first one has never been observed during the course of this study, indicating strong interfacial bond between $(Al_2O_3)_p$ and $MgAl_2O_4$. Interfacial debonding at $MgAl_2O_4$/Al phase boundary, as illustrated in Figs.11(b) and (c), was observed frequently. Debonding resulting from the fracture of $MgAl_2O_4$ crystals present in the

interfacial reaction layer [Fig.11(d)] was noticed less frequently. These results are schematically illustrated in Fig.11(e). Further evidence of the above observations was also obtained by scratching the electropolished surface of the composite with a metal scriber. Such a procedure was found to pull out $(Al_2O_3)_p$ along with $MgAl_2O_4$ crystals, leaving the dimple-like matching region (corresponding to $MgAl_2O_4$ crystals that have been pulled out) in the matrix. This matrix region, from which $(Al_2O_3)_p$ is pulled out, is usually devoid of $MgAl_2O_4$, as can be observed in the micrograph given in Fig.12.

Strength and ductility of $(Al_2O_3)_p$/Al composites are considerably lower than those of SiC_p/Al composites having the same volume fraction of reinforcements [20-23], although mechanical properties of SiC_p and $(Al_2O_3)_p$ reinforcements are similar to each other [24,25]. Slight differences in thermal history, morphology and size of the reinforcements can not provide sufficient reasoning for the observed differences. In SiC_p/Al composites, particulate cracking has been found to be more predominant than interfacial debonding [13,19]. However, in $(Al_2O_3)_p$/Al composite, significant interfacial debonding occurs in addition to particulate cracking. When interfacial debonding occurs, load transfer from the matrix to the reinforcement becomes less effective during further loading. The lower strength and ductility of $(Al_2O_3)_p$/Al composites as compared to SiC_p/Al composite can be explained on the basis of less effective load transfer due to interfacial debonding.

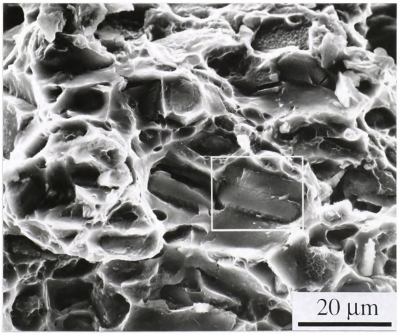

Fig.10 Fracture surface of T6 heat treated $(Al_2O_3)_p$/Al composite showing the particulate cracking [C] and interfacial debonding [D]. Limited plastic deformation of the matrix can also be seen. The fracture strain of the specimen was about 7 %.

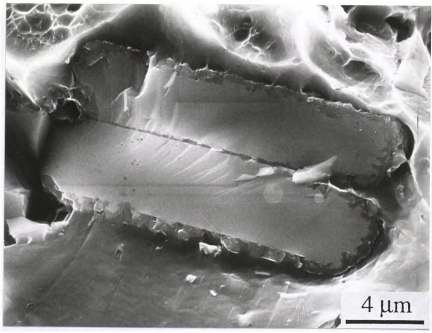

Fig.11(a) Fracture surface of $(Al_2O_3)_p$ with the reaction layer around it. Note that the surface of $(Al_2O_3)_p$ at the interface region is relatively straight indicating that $MgAl_2O_4$ crystals in this region are not grown at the expense of $(Al_2O_3)_p$. Such cases were noticed infrequently.

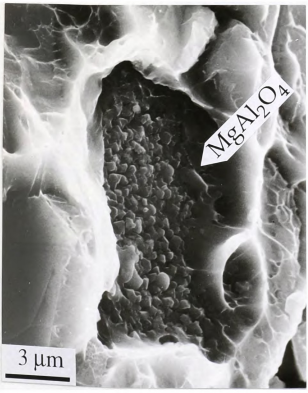

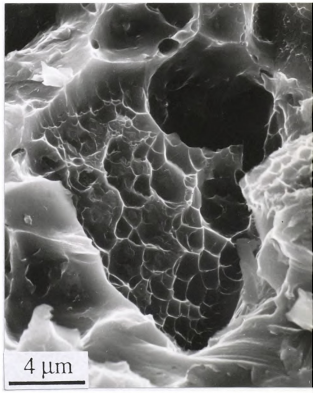

Fig.11 (continued)

(b) Outer surface of $(Al_2O_3)_p$ covered with $MgAl_2O_4$ crystal layer, indicating interfacial debonding along the $MgAl_2O_4$/Al phase boundary.

(c) Matrix region from which $MgAl_2O_4$ layer is debonded. Few $MgAl_2O_4$ crystals stuck to the matrix can be noted at the regions indicated by the arrows.

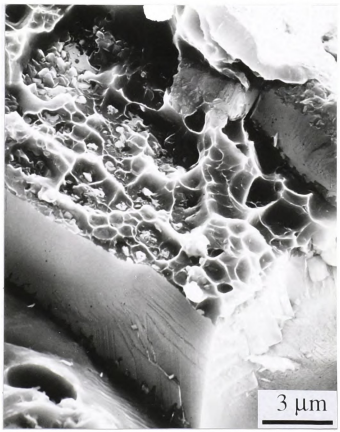

Fig.11 (continued)
(d) Outer surface of $(Al_2O_3)_p$ when interfacial debonding occurrs at $MgAl_2O_4$ layer itself. The roots of $MgAl_2O_4$ can be observed from the sub-surface of $(Al_2O_3)_p$.

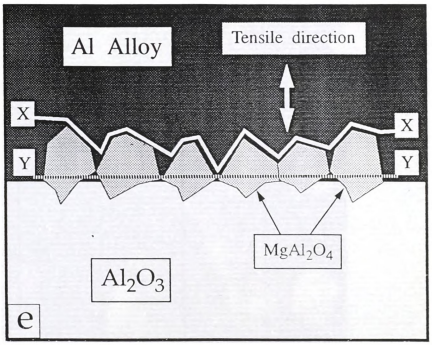

X-X : Interfacial debonding along $MgAl_2O_4$/Al phase boundary

Y-Y : Interfacial debonding along $MgAl_2O_4$ layer itself

Fig.11 (continued)
(e) Schematic illustration of interfacial debonding: Line (XX) represents interfacial debonding along $MgAl_2O_4$/Al phase boundary corresponding to micrographs given in (b) and (c). Line (YY) represents interfacial debonding along $MgAl_2O_4$ layer itself corresponding to micrograph given in (d).

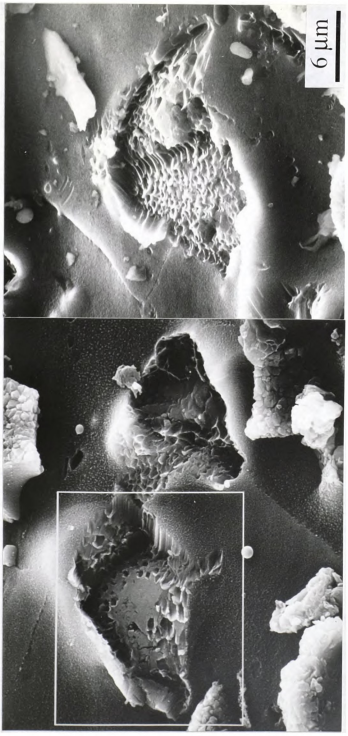

Fig.12 Matrix region from which $(Al_2O_3)_p$ is pulled out by scratching the surface of the electropolished composite.
The dimples are due to the interfacial debonding between the Al alloy and $MgAl_2O_4$ layer.

4. SUMMARY

4.1 Characterization of the interface

The chemical reaction products found to exist at the interface of $(Al_2O_3)_p$/Al composites consist of a layer containing single crystals of $MgAl_2O_4$ spinel. Each $(Al_2O_3)_p$ is fully (or almost fully) covered with $MgAl_2O_4$ single crystals, about 1 μm in size. Based on the microstructural and thermodynamic considerations, each $MgAl_2O_4$ single crystal is believed to have grown at the surface of $(Al_2O_3)_p$ by the reaction between $(Al_2O_3)_p$ and Mg in the molten matrix segregated at the interface region. The reaction between SiO_2 and molten matrix, however, is believed to be a less significant reaction for the formation of $MgAl_2O_4$ crystals observed in the interface region.

4.2 Role of the interface on the tensile properties

Observations on the side surfaces of the fractured tensile specimens of $(Al_2O_3)_p$/Al composite have shown that interfacial debonding as well as particulate cracking play significant roles in the fracture of this composite. Among the various possibilities, interfacial debonding due to the fracture along $MgAl_2O_4$/Al phase boundary was found to occur more frequently than that due to the cracking of $MgAl_2O_4$ layer. Significant interfacial debonding that occurs in $(Al_2O_3)_p$/Al composites during tensile loading can be the contributing factor to their inferior tensile properties as compared to those of SiC_p/Al composites.

5. REFERENCES

1. F.M Hosking, F.F.Portillo, R.Wunderlin, and R.Mehrabian, "Composites of Aluminum alloy", J. Mater. Sci., 17, 477-498, (1982).

2. S.Deonath, R.Bhatt, and P.Rohatgi, "Preparation of cast aluminum alloy-mica particle composites", J. Mater. Sci., 15, 1241-1251, (1980).

3. B.C.Pai, S.Pay, K.V.Prabhakar, and P.K.Rohatgi, Mat. Sci. Eng., 24, 31-44, (1976).

4. P.K.Rohatgi, B.C.Pai, ad S.C.Panda, "Preparation of cast aluminum-silica particle composites", J. Mater. Sci., 14, 2277-2283, (1979).

5. M.K.Surrpa, and P.K.Rohatgi, "Preparation and properties of cast aluminum-ceramic composites", J. Mater. Sci., 16, 983-993, (1981).

6. T.W.Clyne, M.G.Bader, G.R.Cappleman, and P.A.Hubert, "The use of δ-alumina fiber for the metal matrix composites", J. Mater. Sci., 20, 85-96, (1985).

7. A.Munitz, M.Metzger, and R.Mehrabian, "The interface phase in Al-Mg/Al_2O_3 composites", Metall. Trans. A, 10, 1491-1497, (1979).

8. R.E.Tressler, COMPOSITE MATERIAL; Vol.1 Interface in metal matrix composites, edited by A.G.Metcalfe, pp296, Academic press, New York and London, (1974).

9. C.G.Levi, G.J.Abbaschian, and R.Mehrabian, "Interface interactions during fabricatiion of aluminum alloy-alumina fiber composites", Metall. Trans. A., 9, 697-711, (1978).

10. P.K.Rohatgi, J. Metals, 43, 10-15, (4.1991).

11. B. Hallstedt, Z.K.Liu, and J.Argen, "Fibre-matrix interactions during fabrication of Al_2O_3-Mg Metal matrix composites", Mat. Sci. Eng. A, 129, 135-145, (1990).

12. R.Molins, J.D.Bartout, and Y.Bienvenu, "Microstructural and analytical characterization of Al_2O_3-(Al-Mg) composite interfaces", Mat. Sci. Eng. A, 135. 111-117, (1991).

13. G.M.Janowski and B.J.Pletka, "The influence of interfacial structure on the mechanical properties of liquid-phase-sintered aluminum-ceramic composites", Mat. Sci. Eng. A, 129, 65-76, (1990).

14. H.Hino, M.Komatsu, Y.Hirasawa, and M.Sasaki, "Effect of reaction products on mechanical properties of alumina short fiber reinforced magnesium alloy", Proceedings of the Fifth Annual ASM/EDS Advanced Composites Conference, Detroit, Michigan, Oct. 1989, pp 201-208, published by ASM International, Materials Park, Ohio, (1989).

15. B.F.Quigley, G.J.Abbaschian, R.Wunderlin, and R.Mehrabian, "A method for fabrication of aluminum-alumina composites", Metall. Trans. A, 13, 93-100, (1982).

16. J.P.Lucas, J.J.Stephens, and F.A.Greulich, "The effect of reinforcement stability on composition redistribution in cast aluminum metal matrix composites", Mat. Sci. Eng. A, 131, 221-230, (1991).

17. S.R.Nutt and J.M.Duva, "A failure mechanism in Al-SiC composits", Scr. Metall., 20, 1055, (1986).

18. T.Christman, A.Needleman, S.R.Nutt, and S.Suresh, "On the microstructural evolution and microstructural modelling of deformation of a whisker reinforced metal matrix composites", Mat. Sci. Eng. A, 107, 49, (1989).

19. J.C.Lee and K.N.Subraminian, "Failure behavior of particulate reinforced Aluminum alloy composites under uniaxial tension", J. Mater. Sci., (in press).

20. T.G.Nieh and D.J.Chellman, "Modulus measurements in discontinuous reinforced aluminum composites", Scr. Metall., 18, 925-928, (1984).

21. Data provided by DWA Composite Specialities Inc., "Increasing focus on the silicon carbide reinforced aluminum composites", Light Metal Age, 7-14, (6.1986).

22. W.A.Hoover, "Commerciallization of Duralcan aluminum composites", Proceedings of the fifth annual ASM/EDS advanced composites conference, Detroit, Michigan, Oct. 1989, 211-217, published by ASM International, Materials Park, Ohio, (1989).

23. W.C.Harrigan, Jr., Gaebler, E.Davis, and E.J.Levin, "The effect of hot rolling on the mechanical properties of SiC-reinforced 6061 aluminum", Proceedings of a symposium sponsored by the Composite Materials Committee of the Metallurgical Society of AIME and the Materials Science Division of American Society for Metals, held at the 111th AIME Annual Meeting, Dallas, Tx, 1982, 169-180, published by Metallurgical Society of AIME, Warrendale, Pa, (1983).

24. F.A.Girot, J.M.Quenisset, and R.Naslain, "Discontinuously reinforced aluminum matrix composites", Composite Science and Technology, 30, 155-184, (1987).

25. D.W.Richerson, Modern ceramic engineering; properties, processing, and use in design., Marcell Dekker, INC. New York, (1982).

CHAPTER III.

FAILURE BEHAVIOR OF PARTICULATE REINFORCED ALUMINUM ALLOY COMPOSITES UNDER UNIAXIAL TENSION

This chapter is based on the paper that has been published in Journal of Materials Science, vol.27, 5453-5462, 1992. The following is the abstract from the original publication.

Tensile tests were carried out at room temperature on 6061-aluminum alloy reinforced with SiC and Al_2O_3 particulates. Although a significant increase in strength could be achieved by introducing ceramic reinforcements into the aluminum alloy matrix, it is associated with a substantial decrease in fracture strain. In order to understand the reason for the inferior ductility of such composites, analytical solutions were obtained using a simple composite model. SEM studies were carried out on the side surfaces of the fractured specimens to verify the proposed failure behavior. Failure modes observed to operate in such composites under uniaxial tension are described.

Note : Detailed derivations for some of the equations used in this chapter are provided in APPENDIX III.

1. INTRODUCTION

The addition of moderate amounts of SiC particulate [SiC_p] and Al_2O_3 particulate [$(Al_2O_3)_p$], usually less than 30 % by volume, into molten Al alloy has been found to result in significant increases in the strength and elastic modulus [1-7], fatigue resistance [8-10], and wear resistance [11], as well as improved high temperature properties [12-14] of the composites. However, it also results in substantial decrease in the ductility, and consequently the fracture toughness of the composites. This has been the main drawback for the wide use of such metal matrix composites reinforced with ceramic reinforcements. Several studies have been carried out to improve the ductility and the fracture toughness of ceramic reinforced metal matrix composites by modified processing techniques [3,8,15-20]. Large differences in the properties between the reinforced and the unreinforced Al alloys still exist due to large differences in the properties of the matrix and the reinforcements. Poor ductility and fracture toughness of such metal matrix composites are attributed to the operative failure mechanisms.

Nutt and Duva [21], in their <u>in situ</u> TEM studies on SiC whisker reinforced Al matrix composites (SiC_w/Al composites), observed that the void nucleated at the corner of the whisker ends and grew towards the centers of the whisker ends. However, the void formation along the long sides of the SiC_w/Al interface, which are parallel to the tensile direction, was not observed. Based on the above experimental results, void nucleation at the SiC_w/Al interface (i.e interfacial debonding) was proposed as the important failure mechanism in the SiC_w/Al composites [21-23].

You et al [24] proposed another failure mechanism of the SiC_p/Al composite on the basis of the observations on the tensile fracture surfaces. In their study, the numbers of the cracked SiC_p and the debonded interfaces were counted at the fracture surface. From this analysis, the number of the cracked SiC_p was found to be more than twice the number of the debonded interfaces. Extensive plastic deformation in the matrix between SiC_p was also observed from the side-surfaces of the tensile specimen, at regions adjacent to the fracture surface. Based on the above observations, they proposed the matrix failure of the composite due to nucleation, growth and coalescence of voids as a dominant failure mechanism of the SiC_p/Al composites. As a consequence, the cracking of SiC_p and debonding of SiC_p/Al interface were attributed to the matrix failure.

Based on the examination of fractographs of pulled-out SiC_w that are coated with the matrix material, Christman et al [9,25] have proposed ductile failure in the matrix near the SiC_w as one of the operating failure mechanisms of such composites.

Janowski and Pletka [26] had studied interfacial microstructures of Al alloy composites reinforced with SiC_p and $(Al_2O_3)_p$ and their effect on the tensile properties of such composites. Failure modes present in particulate reinforced composites were observed to change depending on the characteristics of the interfacial microstructures. Amorphous reaction layers formed at $(Al_2O_3)_p$/Al interface were found to degrade interfacial bonding, and thereby result in inferior strength and ductility of such composites.

The purpose of the present investigation is to study the general failure behavior of particulate reinforced metal matrix composites under uniaxial tension.

2. EXPERIMENTAL PROCEDURE

The materials used in this study, 6061 Al alloys reinforced with 10 % (by volume) of SiC_p and $(Al_2O_3)_p$, were obtained as extruded cylindrical bars from DURALCAN Aluminum Co. Sheet tensile specimens were machined with the tensile direction oriented both parallel (longitudinal) and perpendicular (transverse) to the extrusion direction, and polished with abrasive papers and rotating laps. They were then T6 heat treated according to conditions listed in Table 1. Oxidation layer formed during heat treatment was removed by polishing with diamond abrasives.

Tensile tests were carried out with an Instron operated at a constant cross-head speed of 0.1 cm/min in air at room temperature. The fracture surface and the side surfaces of tensile specimens were examined by optical and scanning electron microscopic techniques.

Table 1. T6 heat treatment condition used in the present study.

procedure	SiC_p/Al composite	$(Al_2O_3)_p$/Al composite
Solution treatment	530 °C x 70 min.	560 °C x 60 min.
R.T aging	24 °C x 48 hr.	24 °C x 65 hr.
Artificial aging	200 °C x 10 hr.*	170 °C x 14 hr.**

* : overaged condition
** : peak aged condition

3. RESULTS

Some of tensile properties of the reinforced and the unreinforced Al alloy are presented in Table 2. Although considerable increase in the elastic modulus and strength result due to reinforcements, they are accompanied by substantial decrease in the fracture strain. In order to understand the reasons for the inferior ductility of the composite, studies were carried out to characterize the interfacial debonding and particulate cracking. Significant number of debonded interfaces could be observed from the subsurface of the fractured specimens, as shown in Fig.1, for which deep etching was carried out. Such interfacial debondings were formed in a direction perpendicular to the tensile loading as shown in Fig.1 b) and c).

Finely polished tensile specimens were prepared and tested with an Instron to observe the particulate cracking and possible matrix failure at the composite surface. Observations made on the side-surfaces of the fractured tensile specimens, especially in regions adjacent to fracture, revealed significant amounts of microcracks at SiC_p, as shown in Fig.2. Microcracks initiated from the matrix were not observed in the present study. Most of the cracks were formed at SiC_p and $(Al_2O_3)_p$ in the form of interfacial debonding and particulate cracking, or sometimes in the form of ductile failure near the reinforcement. Although severe plastic deformation can be observed in the matrix near the region of cracked SiC_p, particulate crackings were found to always precede the matrix failure. The micrographs exhibiting the initiation of cracks in SiC_p and $(Al_2O_3)_p$ in the tensile specimens are shown in Fig.3 a) and b).

Table 2. The tensile properties of the reinforced and the unreinforced Al alloy (T6 heat treated)

Material	direction*	E (GPa)	σ_{ys}(MPa)	σ_{uts}(MPa)	ϵ_f
SiC_p/Al	T	-	269.5	323.0	2.8
	L	-	302.0	368.6	5.3
$(Al_2O_3)_p$/Al	T	80.6**	285.0	345.2	2.5
	L	79.9**	301.5	364.5	9.0
6061 Al		68.0**	265.5	310.5	20.0

* T : Transverse direction
L : Longitudinal direction
** : Values obtained by sonic resonance test

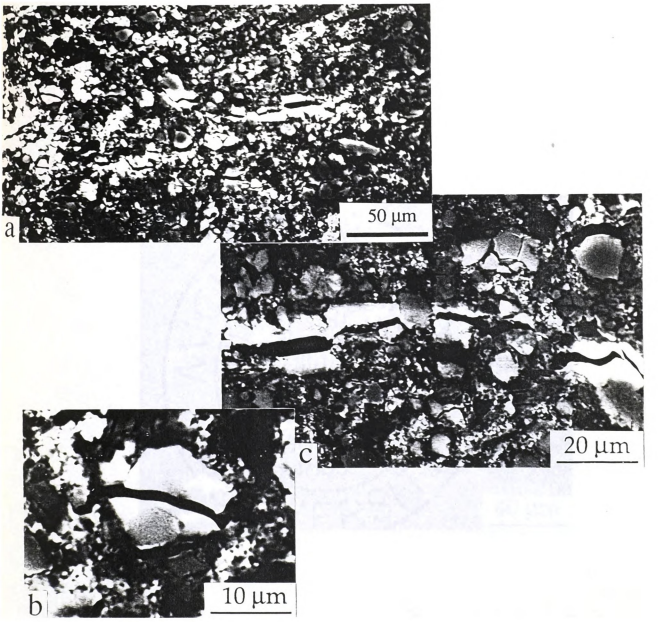

Fig.1 a) SEM micrograph showing crack development in a tensile specimen of SiC_p/Al composite. (etched with HCl to reveal the subsurface region).
b) Interfacial debonding and particulate cracking.
Note the crack propagation into matrix in front of particulate crack.
c) Joining of particulate crack and debonded interface.

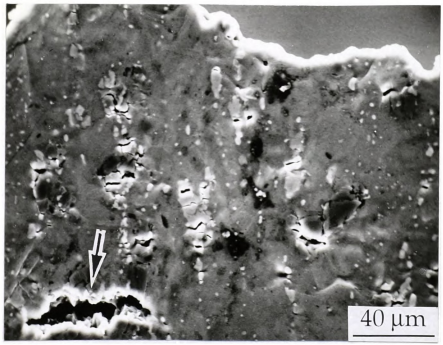

Fig.2 SEM micrograph of the fractured SiC_p/Al composite showing void formation due to joining of opened cracks indicated by arrow. Note that cracks are formed perpendicular to the tensile direction and the number of particulate cracks are significantly more than the debonded interfaces.

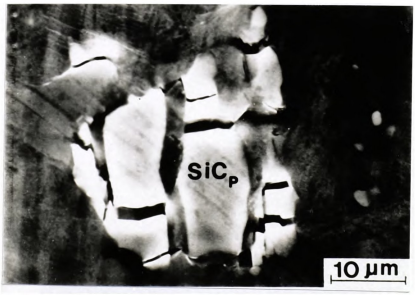

Fig.3 a) Particulate crackings in SiC_p/Al composite which are opened up due to tensile loading. Note that the arrow marks indicate the initiation of the crack propagation into matrix.

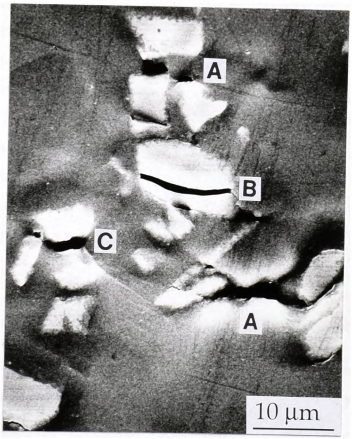

Fig.3 b) Particulate crackings and interfacial debonding in $(Al_2O_3)_p/Al$ composite caused by tensile loading.
A : interfacial debonding
B : particulate cracking
C : matrix adherent to $(Al_2O_3)_p$

4. THEORETICAL BACKGROUND

Most of the three-dimensional engineering problems can be analyzed using two-dimensional approach, since most failures are initiated at free surfaces, where the largest stresses develop. Consider a large thin plate having a circular inclusion, whose elastic constants and thermal expansion coefficient are different from those of the matrix. Uniform uniaxial loading is applied at infinity on the composite system as shown in Fig.4.a). One can solve this problem by superposing the stress function due to uniaxial loading and stress function due to the inelastic strain caused by thermal expansion mismatch as in Fig.4.b). Although the solutions for the problems given in sec. 4.1 and 4.2 can be found elsewhere [27], detailed calculation steps with slightly different method will be presented in order to utilize the intermediate solutions to the analysis.

4.1 Large plate having a circular inclusion with different elastic constants subjected to uniaxial tension.

Consider a plate having a small circular elastic inclusion of radius 'a', which is subjected to uniaxial tension. Under such conditions, the boundary conditions at infinity (r = ∞) are given by

$$\left.\begin{aligned} \sigma_{rr}(\infty,\theta) &= \sigma_0\ (1+\cos 2\theta)/2 \\ \sigma_{r\theta}(\infty,\theta) &= -\sigma_0\ \sin 2\theta/2 \\ \sigma_{\theta\theta}(\infty,\theta) &= \sigma_0\ (\ 1-\cos 2\theta\ )/2 \end{aligned}\right\} \quad 1)$$

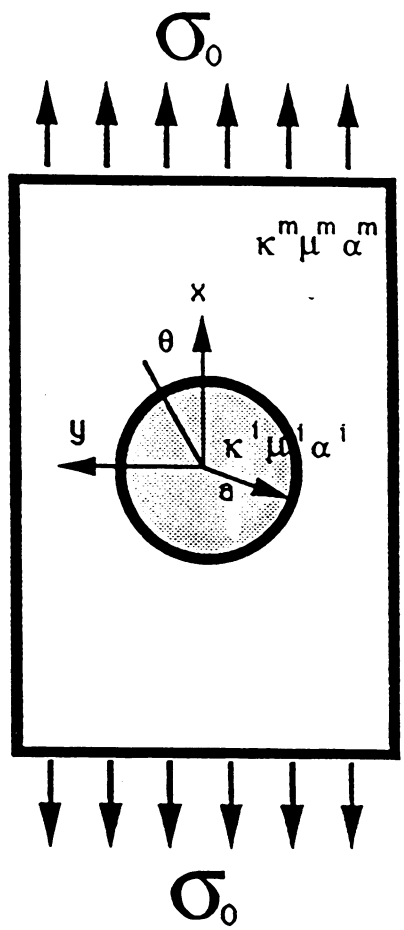

Fig.4 a) Two dimensional composite model; a large thin plate having a circular inclusion with different elastic constants (κ,μ) and thermal expansion coefficients (α) subjected to uniaxial tension, σ_0, where μ = shear modulus, α = thermal expansion coefficient, κ = (3-4ν) for plane strain, κ = (3-ν)/(1+ν) for plane stress.

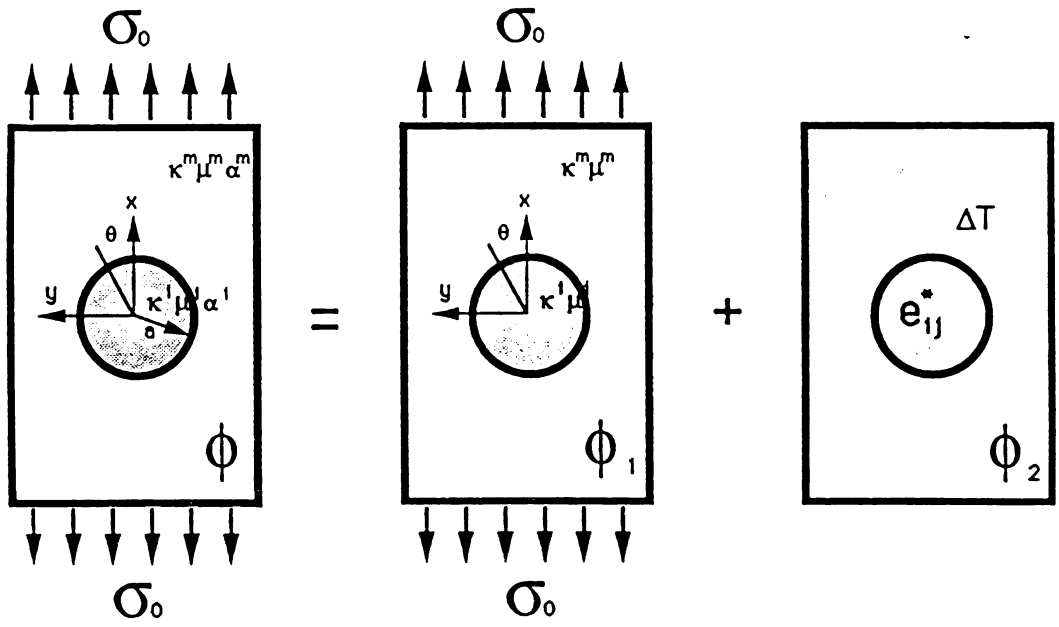

Fig.4 b) Schematics illustrating the superposition of stresses caused by external loading and thermal expansion coefficient mismatch.

The Airy stress function (Φ) for this case can be given as a linear combination of function of polar coordinates r and θ. Matrix part of this function, Φ^{m^1} is

$$\Phi^{m^1}(r,\theta) = \frac{\sigma_0}{4} r^2(1-\cos 2\theta) + \frac{\sigma_0}{4} \left[A\, a^2 \log r + B\, a^2 \cos 2\theta + C\, a^4 \frac{\cos 2\theta}{r^2} \right]$$

where A, B, and C are constants, and superscript m^1 denotes matrix under applied uniaxial loading. One can notice that the first term in Eq 2) describes the undisturbed field (when there in no inclusion in the matrix), and the last three terms describe the local disturbance due to the discontinuity (i,e inclusion) in the elastic medium. However, according to the Saint Venant's principle, the disturbance caused by discontinuity will be negligible at distances which are larger compared to the radius of the discontinuity.

The Airy stress function for the inclusion can be given as

$$\Phi^{i^1}(r,\theta) = \frac{\sigma_0}{4} \left[D\, r^2 + E\, r^2 \cos 2\theta + \frac{F}{a^2} r^4 \cos 2\theta \right] \qquad 3)$$

where D, E, and F are constants, and the superscript i^1 denotes inclusion under applied uniaxial loading. The stress components (σ_{ij}) can be obtained directly from the given Airy stress functions, and the corresponding strain (e_{ij}) and displacement components (u_i) can be determined from the Hooke's law and strain-displacement relationships, respectively. Thus, the resultant stresses and displacements in the matrix and the inclusion are;

$$\sigma_{rr}^{m1} = (\sigma_0/2)[\ 1 + Aa^2/r^2 + (\ 1-2Ba^2/r^2-3Ca^4/r^4\ )\cos 2\theta\ ] \qquad 4.a$$

$$\sigma_{r\theta}^{m1} = (-\sigma_0/2)[\ 1 + Ba^2/r^2 + 3Ca^4/r^4\ ]\sin 2\theta \qquad 4.b$$

$$\sigma_{\theta\theta}^{m1} = (\sigma_0/2)[\ 1 - Aa^2/r^2 - (\ 1-3Ca^4/r^4)\cos 2\theta\ ] \qquad 4.c$$

$$u_r^{m1} = (\sigma_0/8\mu^m)[\ (\kappa^m-1)r - 2Aa^2/r + \{\ 2r + B(\kappa^m+1)a^2/r + 2Ca^4/r^3\ \}\cos 2\theta\ ] \qquad 4.d$$

$$u_\theta^{m1} = (\sigma_0/8\mu^m)[\ -2r - B(\kappa^m-1)a^2/r + 2Ca^4/r^3\ ]\sin 2\theta \qquad 4.e$$

$$\sigma_{rr}^{i1} = (\sigma_0/2)[\ D - E\cos 2\theta\ ] \qquad 4.f$$

$$\sigma_{r\theta}^{i1} = (\sigma_0/2)[\ E + 3Fr^2/a^2\ ]\sin 2\theta \qquad 4.g$$

$$\sigma_{\theta\theta}^{i1} = (\sigma_0/2)[\ D + (\ E + 6Fr^2/a^2\ )\cos 2\theta\ ] \qquad 4.h$$

$$u_r^{i1} = (\sigma_0/8\mu^i)[\ D(\kappa^i-1)r - \{\ 2Er - F(\kappa^i-3)r^3/a^2\ \}\cos 2\theta\ ] \qquad 4.i$$

$$u_\theta^{i1} = (\sigma_0/8\mu^i)[\ 2Er + F(\kappa^i+3)r^3/a^2\ ]\sin 2\theta. \qquad 4.j$$

In order to determine the constants in Eq 4), appropriate boundary conditions for the composite system should be set up at the interface, assuming perfect interfacial bonding. Since the stresses and the displacements have to be continuous at the interface, Boundary conditions at matrix-inclusion interface (r = a) are

$$\sigma_{rr}^{m1}(a,\theta) = \sigma_{rr}^{i1}(a,\theta)$$

$$\sigma_{r\theta}^{m1}(a,\theta) = \sigma_{r\theta}^{i1}(a,\theta)$$

$$u_r^{m1}(a,\theta) = u_r^{i1}(a,\theta), \quad \text{and} \tag{5}$$

$$u_\theta^{m1}(a,\theta) = u_\theta^{i1}(a,\theta).$$

Solving the boundary conditions, one can obtain the constants as

$$\left.\begin{aligned} A &= [\ (\kappa^m-1)-\Gamma(\kappa^i-1)\ ]/[\ \Gamma(\kappa^i-1)+2\ ] \\ B &= 2\ (\ \Gamma-1\ )/(\ \Gamma+\kappa^m\ ) \\ C &= (\ 1-\Gamma\ )/(\ \Gamma+\kappa^m\ ) \\ D &= [\ \kappa^m+1\ ]/[\ \Gamma(\kappa^i-1)+2\ ] \\ E &= -(\ \kappa^m+1\ )/(\ \Gamma+\kappa^m\ ) \\ F &= 0 \end{aligned}\right\} \tag{6}$$

where $\Gamma = \mu^m/\mu^i$.

4.2 Large plate having a circular inclusion with different thermal expansion coefficient

If the system involves inelastic strain caused by thermal expansion coefficient mismatch, it will produce inelastic stress on the body. Some important results will be listed without derivation, since the exact solutions for this problem can be found elsewhere [27]. The compressive stress (-P) at the inclusion/matrix interface, resulting from thermal expansion mismatch, is obtained as

$$P = [\ 4\mu^m\mu^i(1+\eta)\Delta\alpha\Delta T\ ]/[\ 2\mu^i+(\kappa^i-1)\mu^m\ ]. \tag{7}$$

Stress components for the matrix and inclusion are determined as

$$\sigma_{rr}^{m^2}(r,\theta) = -Pa^2/r^2 \qquad 8.a$$

$$\sigma_{\theta\theta}^{m^2}(r,\theta) = Pa^2/r^2 \qquad 8.b$$

$$\sigma_{r\theta}^{m^2}(r,\theta) = 0 \qquad 8.c$$

$$\sigma_{rr}^{i^2}(r,\theta) = -P \qquad 8.d$$

$$\sigma_{\theta\theta}^{i^2}(r,\theta) = -P \qquad 8.e$$

$$\sigma_{r\theta}^{i^2}(r,\theta) = 0 \qquad 8.f$$

where superscripts m^2 and i^2 represent matrix and inclusion parts under inelastic contribution due to thermal expansion coefficient mismatch.

Hence, from the results in the Sec. 4.1 and 4.2, the total stress and displacement should be the sum of the elastic and the inelastic terms;

$$\sigma_{ij}^{I} = \sigma_{ij}^{i^1} + \sigma_{ij}^{i^2} \qquad 9.a)$$

$$\sigma_{ij}^{M} = \sigma_{ij}^{m^1} + \sigma_{ij}^{m^2} \qquad 9.b)$$

$$u_i^{I} = u_i^{i^1} + u_i^{i^2} \qquad 9.c)$$

$$u_i^{M} = u_i^{m^1} + u_i^{m^2}. \qquad 9.d)$$

Above stress components evaluated in the polar coordinate can be transformed into the stress components in the Cartesian coordinate using t transformation laws;

$$\sigma_{xx} = \sigma_{rr}\cos^2\theta - 2\sigma_{r\theta}\cos\theta\sin\theta + \sigma_{\theta\theta}\sin^2\theta \qquad 10.a)$$

$$\sigma_{yy} = \sigma_{rr}\sin^2\theta + 2\sigma_{r\theta}\cos\theta\sin\theta + \sigma_{\theta\theta}\cos^2\theta \qquad 10.b)$$

$$\sigma_{xy} = (\sigma_{rr} - \sigma_{\theta\theta})\cos\theta\sin\theta + \sigma_{r\theta}(\cos^2\theta - \sin^2\theta). \qquad 10.c)$$

5. ANALYSIS and DISCUSSION

5.1 Stress concentration and load transfer

When a discontinuity is present in a body, local stress disturbances will be developed near the discontinuity. However, the extent and shape of stress disturbance near the discontinuity depend on the geometry of the discontinuity, and the difference in the elastic constants and thermal expansion coefficients between the matrix and the discontinuity. For example, when a large thin plate having a discontinuity with smaller elastic modulus than the matrix (such as a hole) is subjected to uniaxial tension, stress concentration will occur at the matrix near the equator of the hole, and decrease rapidly at distances away from the hole. However, in case of a large thin plate having a discontinuity with an elastic modulus higher than that of the matrix, stress concentration occurs at the discontinuity rather than in the matrix. Such stress disturbances for SiC inclusion in an Al alloy matrix are illustrated in Figs.5 and 6. The elastic constants and thermal expansion coefficients of 6061 Al alloy and SiC used for the calculations are given in Table 3. Although, computations were carried out for SiC_p/Al composite only, trends exhibited by $(Al_2O_3)_p$/Al composite are expected to be similar. The stress acting on the matrix near the equator of the inclusion is found to be lower than the applied tensile stress due to the load transfer to the inclusion through the interface. However, the stress acting on the matrix near the pole of the inclusion is calculated to be about 1.5 times that of the applied tensile stress. This stress reaches a maximum value in the matrix at a point slightly away from the pole along the direction of the applied

Table 3. Selected material properties for SiC and Al_2O_3 [28]

Material	E (GPa)	μ (GPa)	ν	α (/°C)
6061 Al	68.0	29.3	0.33	28.0×10^{-6}
SiC	423.0	178.0	0.19	3.0×10^{-6}
Al_2O_3	396.9	160.2	0.24	6.5×10^{-6}

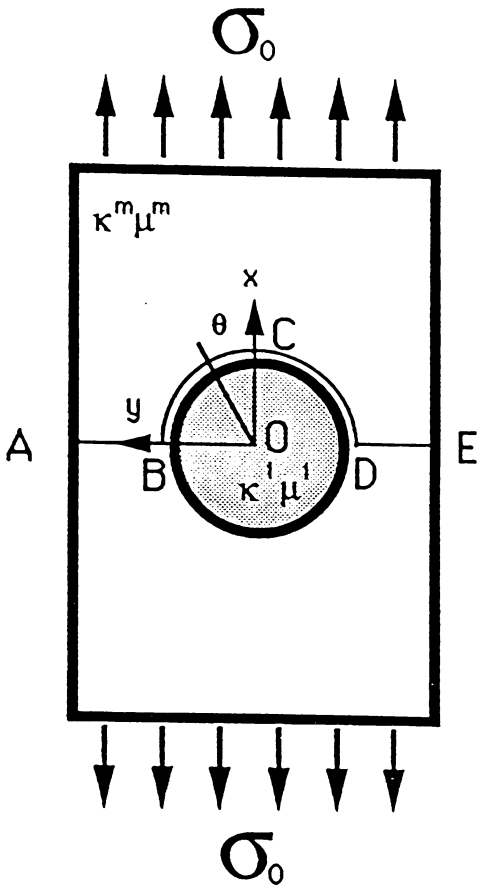

Fig.5 Normalized stress (σ_x/σ_0) distribution in the region of circular SiC$_p$ and 6061 Al alloy.
a) schematic of the loading configuration and the trajectory along which stress distributions are drawn.

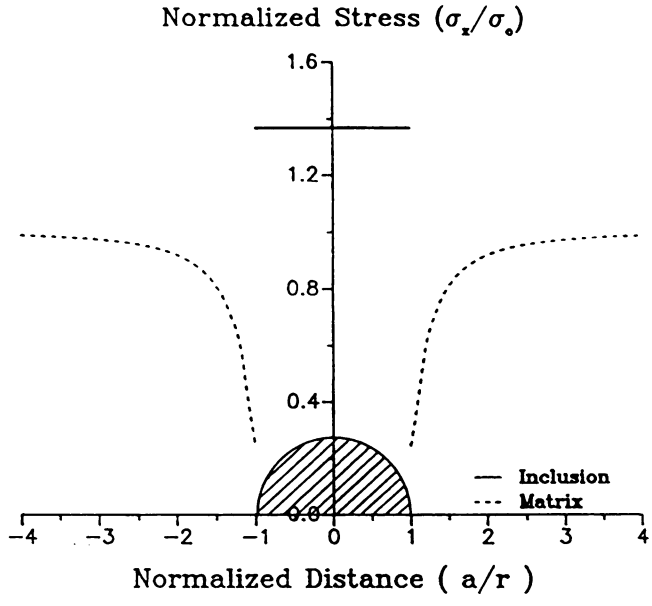

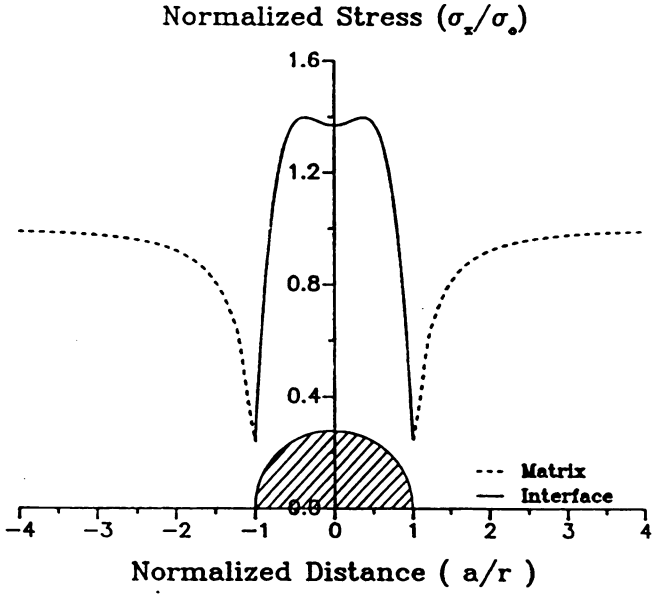

Fig.5 (continued)
b) along the line ABODE
c) along the interface BCD
Note : half circle is indicated in plots b) and c) for identifying the location of the particulate.

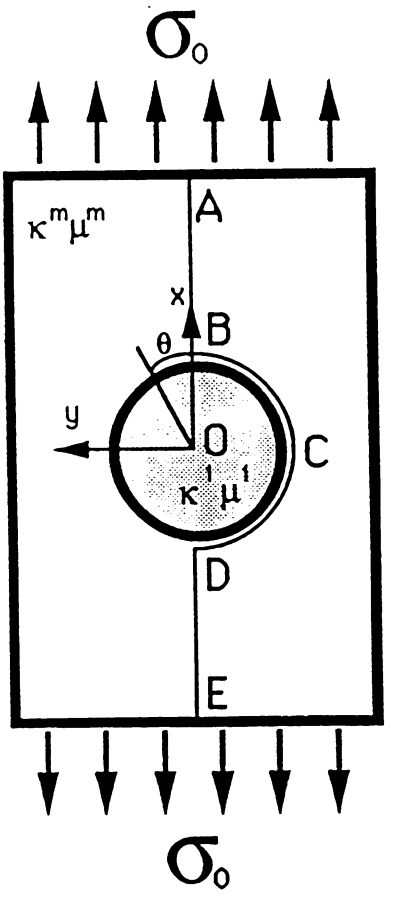

Fig.6 Normalized stress (σ_y/σ_0) distribution in the region of circular SiC$_p$ and 6061 Al alloy.
a) Schematic of the loading configuration and the trajectory along which stress distributions are drawn.

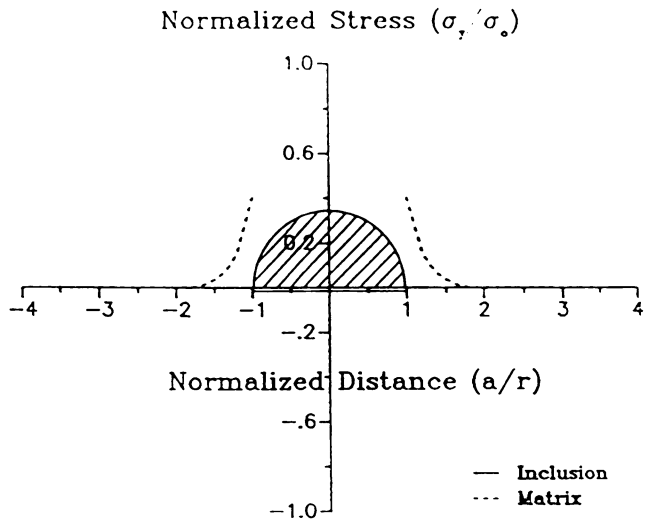

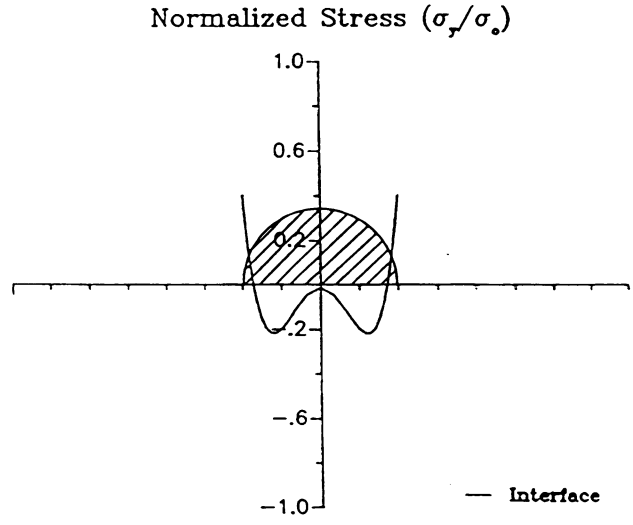

Fig.6 (continued)
b) along the line ABODE
c) along the interface BCD
Note : half circle is indicated in plots b) and c) for identifying the location of the particulate.

stress, and finally decreases to the level of applied tensile stress at regions away from the pole. Such a stress distribution at the pole region of the inclusion, along the direction of the tensile stress, appears to be responsible for some of the matrix material to be adherent to the particulate reinforcement, as has been observed occasionally at the debonded interfaces (Fig.3 b). This stress distribution is illustrated in Fig.7.

5.2 Interfacial debonding and particulate cracking

The axial stress developed in the matrix along the matrix/inclusion interface (σ^{m}_{xx}) increases significantly at the region of the pole of the inclusion, and decreases very rapidly as the angle θ measured from the pole rotates and approaches 90°, while the stress inside the inclusion remains constant, as shown in Fig.5. Such a stress concentration at the inclusion and the matrix/inclusion interface can cause particulate cracking and interfacial debonding, respectively. Using Eq.4) and 10), the maximum stress in the matrix near the pole of SiC_p is calculated to be about 1.5 times of the applied tension, assuming plane stress conditions. With a tensile stress of 300 - 400 MPa, typical strength of such composites, the stress at the pole of SiC_p reaches about 450 - 600 MPa. Although such a stress is not large enough compared to the interfacial bonding strength of SiC and Al reported by Flom and Arsenault [29], interfacial debonding may occur due to imperfect interface present in the composites. Formation of intermetallic compound [30] or amorphous phase [26] can cause degradation of the interface. Sharp corners [21] will result in higher stress

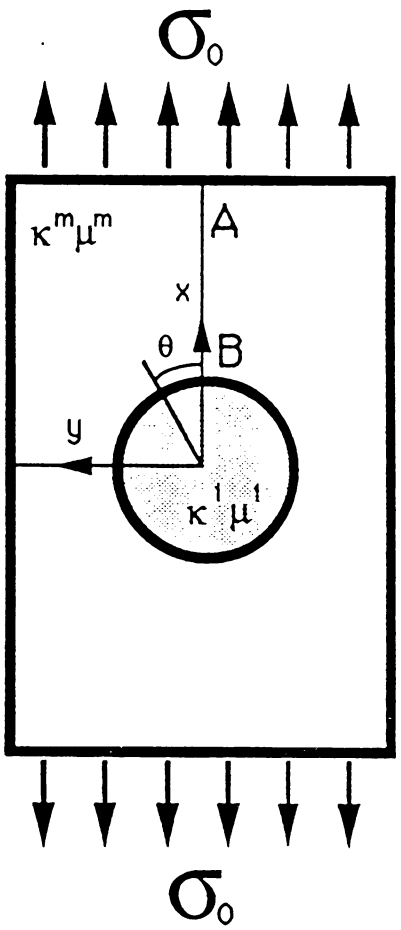

Fig.7 a) schematic of the loading configuration and the trajectory along which stress distributions are drawn.

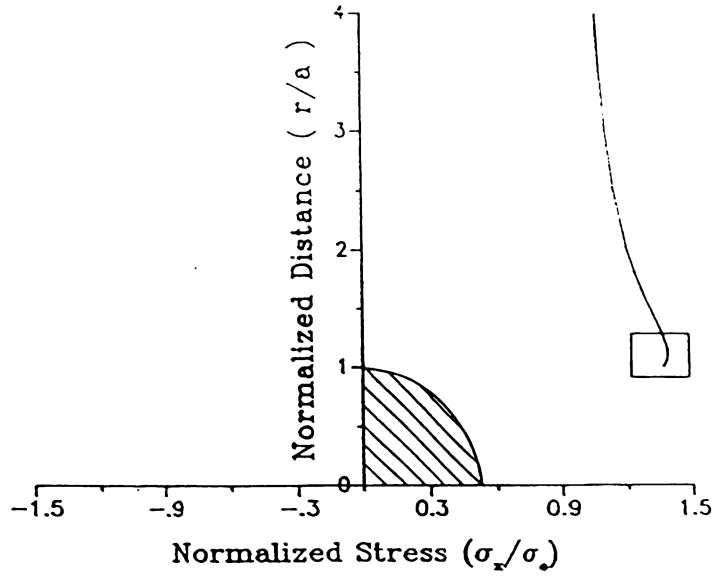

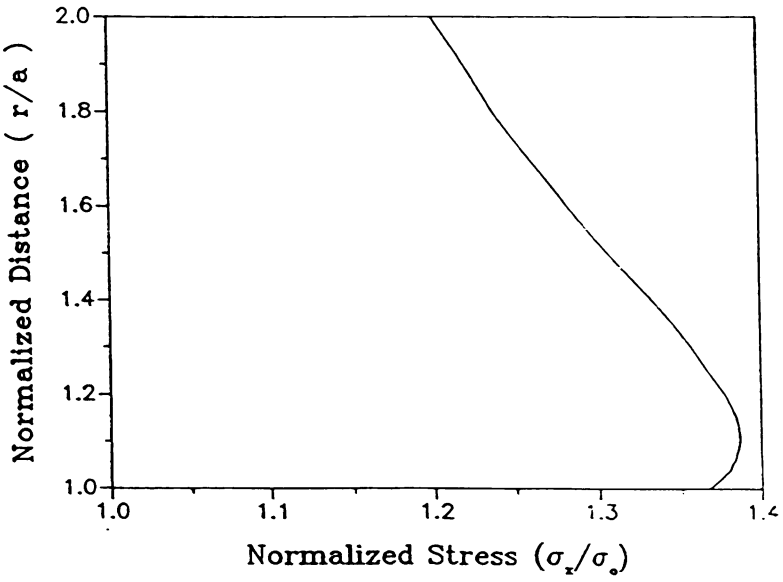

Fig. 7 (continued)

b) Normalized stress (σ_x/σ_0) distribution from the pole of SiC_p along the line AB (tensile direction).

c) Detailed stress distribution pattern within the enclosed rectangle.

Note : quarter circle is indicated in plot b) for identifying the location of the particulate.

concentration. Incipient debonding at the interface as a consequence of the manufacture results in severe stress concentration, as shown in Fig.8. Once interface is debonded at the pole of SiC_p, the crack so formed will propagate along the SiC_p/Al interface to some extent and then deviate into the matrix. This is due to the fact that the axial stress (σ_{xx}) at the interface decreases and that in the matrix increases abruptly as can be seen in Fig.5.

Tensile loading also gives rise to stress concentration within SiC_p, causing particulate cracking. From Eq.4) and 10), the stress exerted on SiC_p is calculated to be about 1.5 times that of the applied tensile stress. Although, this calculated stress is smaller than the fracture strength of SiC, its failure can occur even under small stress value, since most ceramic particle have flaws, grain boundaries, and sharp points where higher stress is concentrated. From Fig.3, which illustrated typical particulate cracking under tension, one can notice that particulate cracking precedes matrix failure, although severe plastic deformation could be observed in the matrix near the region of cracked SiC_p. Once SiC_p has cracked, the constraint on the plastic deformation of the matrix will disappear. Then matrix near SiC_p can easily undergo plastic deformation. Such a situation can be considered to be similar to the matrix alloy with a crack in it, providing a higher stress concentration at the crack tip. Under such conditions, matrix fails easily, and the ductility of the composite will decrease significantly.

Fig. 8 SEM micrograph showing the incipient debonding and compound layer observed in $(Al_2O_3)_p$/Al composite.
Note : micrograph was taken from the surface perpendicular to the extrusion direction.

5.3 Effect of thermal residual stress on failure mode

In this specific case, the pressure acting on the matrix/inclusion interface (-P in Eq.7) is computed to be about -800 MPa for the temperature drop down form the composite fabrication temperature to room temperature ($\Delta T \approx 600$ °C). However, upon cooling from the fabrication temperature, most of this inelastic stress will be relieved by the plastic deformation of the matrix near SiC_p (i.e, generation of dislocation around SiC_p) and only a small portion of about -30 MPa, as estimated by Arsenault and Taya [31], will remain in the form of residual stress at the interface. These inelastic stresses acting on SiC_p and the matrix will not change the state of stress significantly, since values are small compared to those of the applied stress. Consequently, there should be no substantial changes in the mode of particulate cracking and interfacial debonding as a result of the thermal residual stress.

5.4 Proposed failure modes

Based on the present study, the failure mechanism of the particulate reinforced Al alloy composites can be summarized as follows:
When a composite system is subjected to uniaxial tension, the maximum tensile stress is generated at the reinforcement and matrix near the pole of the reinforcement, in the same direction to the applied tension. Such a stress concentration may cause particulate cracking or interfacial debonding. As loading continues, the particulate cracks and debonded interfaces easily open up due to the plastic deformation of the matrix near the reinforcement. New cracks will develop in the matrix at

the tip of the opened-up crack and propagate into the matrix until they are joined with nearby cracks, resulting in a large void. Schematics of various steps for this failure mode are illustrated in Fig.9.

The micrographs of the side-surfaces of tensile specimens adjacent to the fractured region are given in Figs.1, 2, and 3. Extensive particulate crackings and debonded interfaces can be observed in these micrographs. Joining of nearby cracks into a large crack can also be observed in Fig.1 c). The void formation, as a result of such coalescences, can be seen in Fig.2. Based on these observations, particulate cracking, in addition to interface debonding, can be proposed as a major contributor to the failure of the particulate reinforced Al alloy composites.

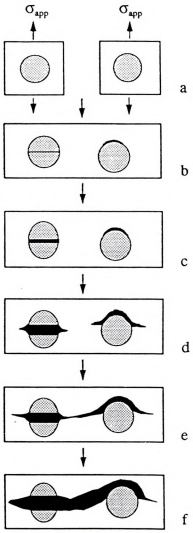

Fig.9 The schematics showing the failure mechanism of the particulate reinforced Al alloy composites.
a) Loading configuration
b) Formation of particulate cracking and interfacial debonding
c) Opening-up of cracked plane and debonded interface due to plastic flow of Al matrix.
d) Crack propagation into Al matrix due to stress concentration build up at the crack tip.
e) Joining of cracks.
f) Void formation.

6. CONCLUSIONS

Stress concentration in the matrix near the pole of particulate, and stress concentration within the particulate, appear to result in interfacial debonding and particulate cracking respectively. Increase in applied stress makes such microcracks open. New cracks develop in the matrix at the tip of the opened-up crack, propagate into matrix and join with nearby cracks, and form a large void. Based on the microscopic examinations and analytical study, interfacial debonding and particulate cracking together were considered to be responsible for the substantial decrease in the ductility of the particulate reinforced Al alloy composites.

Since particulate cracking and interfacial debonding were observed to always precede the matrix failure, such phenomena appear to be a more responsible for the failure than a mechanism based on the matrix failure.

7. REFERENCES

1. N. Tsangarakis, B.O.Andrews and C.Cavallaro, "Mechanical properties of some silicon carbide reinforced aluminum composites", J. Compo. Mat., 21, 481-492, (1987).

2. T.G.Nieh and D.J.Chellman, "Modulus measurements in discontinuous reinforced aluminum composites", Scr. Metall., 18,925-928, (1984).

3. R.J.Arsenault and S.B.Wu, "A comparison of PM vs. melted SiC/Al composite", Scr. Metall., 22, 767-772, (1988).

4. R.J.Arsenault, "The strengthening of aluminum alloy 6061 by fiber and platelet silicon carbide", Mat. Sci. Eng., 64, 171-181, (1981).

5. Y.Flom and R.J.Arsenault, "Deformation of SiC/Al composites", J. Metals, 38, 31-34, (1986).

6. V.C.Nardone, "Assessment of models used to predict the strength of discontinus silicon carbide reinforced aluminum alloys", Scr. Metall., 21, 1313-1318, (1987).

7. R.H.Jones, C.A.Lavender and M.T.Smith, "Yield strength - fracture toughness relationships in metal matrix composites", Scr. Metall., 21, 1565-1570, (1987).

8. W.A.Longsdon and P.K.Liaw, "Tensile, fracture toughness and fatigue crack growth rate properties of silicon carbide whisker and particulate reinforced aluminum metal matrix composite", Eng. Fract. Mech., 24, NO.5, 737-751, (1986).

9. T.Christman and S.Suresh, "Effect of SiC reinforced and aging treatment or fatigue crack growth in an Al-SiC composite", Mat. Sci. Eng., 102, 211-216, (1988).

10. J.K.Shang, W.Yu and R.O.Ritchie, "Role of silicon carbide particles in fatigue crack growth in SiC-particulate-reinforced aluminum alloy composites", Mat. Sci. Eng., 102, 181-192, (1988).

11. F.M.Hosking, F.F.Portillo, R.Wunderlin and R.Mehrabian, "Composite of aluminum alloys: fabrication and wear behavior.", J. Mat. Sci., 17, 477-498, (1982).

12. F.A.Girot, J.M.Quenisset and R.Naslain, "Discontinuously reinfoeced aluminum matrix composites", Comp. Sci. Tech., 30, 155-184, (1987).

13. V.C. Nardone and J.R. Strife, "Analysis of the creep behavior of silicon carbide whisker reinforced 2124 Al(T4)", Metall. trans., 18A, 109-114, (1987).

14. K.S.Ravichandran, "Advanced aerospace Al alloys", J. Metals, 39, 28-32, (1987).

15. J.J.Stephens, J.P.Lucas and F.M.Hosking, "cast Al-7Si composites : effect of particle type and size on mechanical properties", Scr. Metall., 22, 1307-1312, (1988).

16. D.L.McDanels, "Analysis of stress - strain, fracture, and ductility behavior of aluminum matrix composites containing discontinuous silicon carbide reinforcement", Metall. Trans., 16A, 1105-1115, (1985).

17. R.J.Arsenault and S.B.Wu, "The strength differential and Bauschinger effect in SiC-Al composites", Mat. Sci. Eng., 96, 77-88, (1987).

18. A.K.Vasudevan, O.Richmond, F.Zok and J.D.Amburg, "The influence of hydrostatic pressure on the ductility of Al-SiC composites", Mat. Sci. Eng., A107, 63-69, (1989).

19. H.Ohtsu, "Aluminum alloys matrix composites using particle dispersion", Proceeding of the fifth annual ASM/EDS advanced composites conference, Detroit, Michigan, Oct. 1989, pp 187-199, published by ASM International, Materials Park, Ohio, (1989)

20. D.J.Lloyd, H.Lagace, A.McLeod and P.L.Morris, "Microstructural aspects of aluminum - silicon carbide particulate composites produced by a casting method", Mat. Sci. Eng., A107, 73-80, (1989).

21. S.R.Nutt and J.M.Duva, "A failure mechanism in Al-SiC composites", Scr. Metall., 20, 1055-1058, (1986).

22. S.R.Nutt and A.Needleman, "Void nucleation at fiber ends in Al-SiC composites", Scr. Metall., 21, 705-710, (1987).

23. J.J.Lowandowski, C.Liu and W.H.Hunt, "Effects of matrix microstructure and particle distribution on fracture of an aluminum metal matrix compossite", Mat. Sci. Eng., 107A, 241-255, (1989).

24. C.P.You, A.W.Thompson and I.M.Bernstein, "Proposed failure mechanism in a discontinuously reinforced aluminum alloy", Scr. Metall., 21, 181-185, (1987).

25. T.Christman, A.Needleman, S.Nutt and S.Suersh, "On microstructural evolution and microstructural modelling of deformation of a whisker reinfroced metal matrix composite", Mat. Sci. Eng., 107A, 49-61, (1989).

26. G.M.Janowski and B.J.Pletaka, "The influence of interfacial structure on the mechanical properties of liquid-phase-sintered aluminum-ceramic composites", Mat. Sci. Eng., A129, 65-76, (1990).

27. N.I.Muskhelishvili, Some basic problems of the mathematical theory of elasticity, pp 215-216, P.Noordhoff Ltd. Groningen-Holland, (1953).

28. Y.S.touloukian, Editor, Thermophysical properties of high temperature solid materials, vol.6, part I, Thermophysical properties research center, Purdue University, (1967).

29. Y.Flom and R.J.Arsenault, "Interfacial bond strength in an aluminum alloy 6061-SiC composite", Mat. Sci. Eng., 191-197, 77, (1986).

30. T.Iseki, T.Kameda and T.Maruyama, "Interfacial reactions between SiC and aluminum during joining", J. Mat. Sci., 19, 1692-1698, (1984).

31. R.J.Arsenault and M.Taya, "Thermal residual stress in metal matrix composite", Acta Metall., 651-659, 35, (1987).

CHAPTER IV

EFFECT OF COLD ROLLING ON THE ELASTIC PROPERTIES OF $(Al_2O_3)_p$/Al COMPOSITE

This chapter is based on the paper that will is scheduled to appear in Journal of Materials Science, vol.28, 1993. The following is the abstract from the original publication.

Mechanical shaping of an aluminum alloy reinforced with Al_2O_3 particulates [$(Al_2O_3)_p$/Al] was carried out by cold rolling operation. Rolling was performed unidirectionally in a direction perpendicular to the extrusion direction of the composite, until edge cracks formed. Cold rolling was found to cause the particulate cracking and interfacial debonding, as well as the redistribution of $(Al_2O_3)_p$. These parameters have significant roles in determining the elastic properties of the resultant composite.

1. INTRODUCTION

Metal matrix composites reinforced with ceramic particulates, due to their improved mechanical properties, their economy of fabrication, and the ease of mechanical shaping, are gaining commercial importance for potential applications such as engine components [1-5], structural [6,7], and aerospace materials [8,9]. However, these applications involve mechanical working during shaping process. The mechanical forces associated with mechanical working not only cause the redistribution of the reinforcements, but also cause microscopic damages, such as particulate cracking and interfacial debonding [10], affecting the material properties of the resultant composite. Changes in mechanical properties, especially elastic properties, due to mechanical shaping are one of the important considerations that have to be taken into account in engineering design.

The Young's modulus is usually measured from the slope of the proportional region in stress-strain diagram. However, this property can also be measured very accurately using the "sonic resonance method", with minimal error due to inelastic behavior. The principal idea behind this method can be explained using the equation by which one can measure the propagating speed of sonic wave through a medium. For flexural waves travelling through a solid,

$$v = (F/P)^{1/2} \qquad 1)$$

,where v = propagating speed of flexural wave on a string

F = tension applied to both side of the string

P = mass per unit length of the string.

Some manipulations of Eq 1) result in

$$E = (1/\epsilon)\rho v^2 \qquad 2)$$

where E = the Young's modulus of the string

ϵ = the elastic strain of the string due to tension (F), and

ρ = the density of the string.

Since the strain is constant under constant tensile loading, the Young's modulus is directly proportional to the density of the string and squared amount of the speed of the propagating wave:

$$E \propto \rho v^2 . \qquad 3)$$

The speed of wave can be expressed as $v = \lambda f$, where λ is the wave length and 'f' is the frequency. However, the value of λ becomes constant, when the length of the string and the mode of vibration are specified. Thus, Eq 3) can be simplified as

$$E \propto \rho f^2 \qquad 4)$$

,where 'f' is the frequency of the flexural wave. The Young's moduli of solid materials are proportional to their densities and squared amount of the flexural resonance frequencies. Therefore, if the resonance frequency of a material can be measured, the Young's modulus

can be calculated. This method is often called as "sonic resonance method" or "dynamic resonance technique".

The objectives of the present study are to investigate the effect of cold rolling on the redistribution of $(Al_2O_3)_p$ clusters and microcracks in $(Al_2O_3)_p$/Al composites, and to study their influences on the elastic properties of the resultant composites.

2. EXPERIMENTAL PROCEDURE

2.1 specimen preparation

Duralcan composite (W6A 10A) with 6061 aluminum alloy reinforced with 10 % of $(Al_2O_3)_p$ (by volume), obtained in the form of extruded cylindrical bar with extrusion ratio of 20:1, was used in this study. A three dimensional view of as-extruded composite, exhibiting bandings of $(Al_2O_3)_p$ clusters along the direction of extrusion, is shown in Fig.1. The size of $(Al_2O_3)_p$ was measured using the optical image analyzer and found to have an average major dimension of 9.6 μm with an aspect ratio of about 2.

The stock material was cut out, annealed at 560 °C for 30 min., and quenched in cold water before rolling. Cold rolling was carried out unidirectionally to various percentages of reduction in thickness in a direction perpendicular (transverse) to the extruded direction. A reduction ratio of about 10 % per pass was used to obtain homogeneous matrix flow and to minimize the formation of edge cracks on the composites. Thin slices with a direction parallel (longitudinal) and perpendicular (transverse) to the extruded direction were cut from the rolled sheets with a low speed diamond saw. These slices were polished with abrasive papers and rotating laps in order to remove the damaged surface layer affected by rolls. The prismatic bars with dimensions of 46.85 x 9.1 x 0.95 (mm) were machined from these slices.

As-received and cold rolled specimens annealed at different temperatures were etched with Keller's reagent to reveal the grain boundaries. The grain size measurement on these specimens were

performed using line intercept method. The grain size of heavily rolled composites are found to be generally smaller than those of the lightly rolled ones [11,12]. However, the influence of annealing temperature on the resultant grain size was more significant than that of amount of prior cold work [Figs. 2(a) and (b)]. As a result, two different solution treatment temperatures have to be selected to obtain same grain size in specimens subjected to different extents of cold work. The details of T6 heat treatments used are

1. solution treatment
   : 560 °C for 1 hour (for as-received composite)
     590 °C for 1 hour (for all cold rolled composites)
2. room temperature aging for 65 hours
3. artificial aging
   : 170 °C for 14 hours (to obtain peak hardness).

An average grain size of about 20-23 μm in the peak hardness condition was obtained for all the specimens used for the Young's modulus measurements.

Fig.1 A three dimensional view of as-extruded $(Al_2O_3)_p$/Al composite exhibiting bandings of $(Al_2O_3)_p$ clusters along the direction of extrusion.

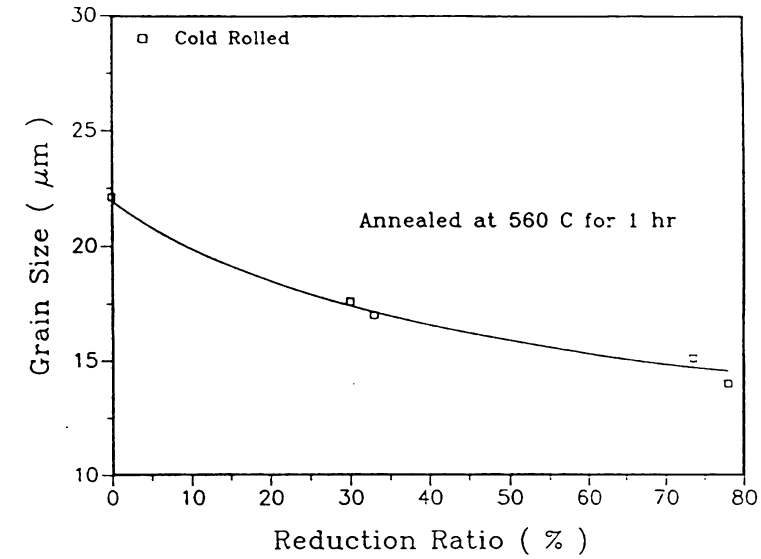

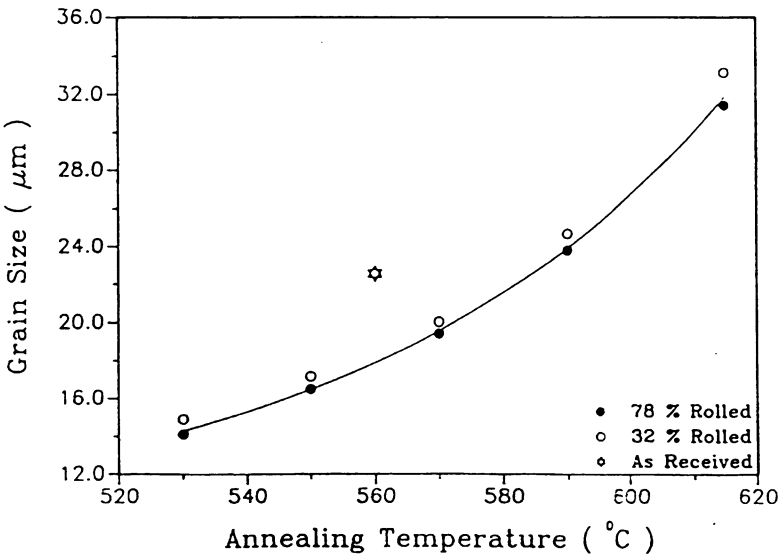

Fig.2 The measurements of the grain size of the composite as a function of a) amount of prior cold rolling and b) annealing temperature.

2.2 Measurement of elastic constants

All measurements of the Young's modulus were carried out at room temperature in air using standard sonic resonance test method designated by ASTM C848-78. A schematic setup used for the sonic resonance measurement is shown in Fig.3(a). The test setup consists of variable-frequency synthesizer, which generates a sinusoidal signal of known frequency. This electrical signal is converted into a mechanical derive using a piezoelectric transducer. The mechanical vibration travels along the supporting cotten thread thruogh the suspended specimen to another supporting cotten thread, which is connected to the other pick-up transducer which detect mechanical vibration of the specimen and convert it back into an electrical signal. This electrical is amplied, filtered, passed through a digital voltmeter, and displayed on an oscilloscope. In order to obtain torsional resonance frequencies as well as flexural ones, the cotten threads are attached to opposite sides of the specimen as shown in Fig.3(b). All specimens were suspended by cotten threads by attaching them to points located at a distance (15 % of the specimen length) from the both ends of the prismatic bar shaped specimens so as to minimize possible experimental errors in the Young's modulus measurements caused by the shifts in the location of the supporting threads.

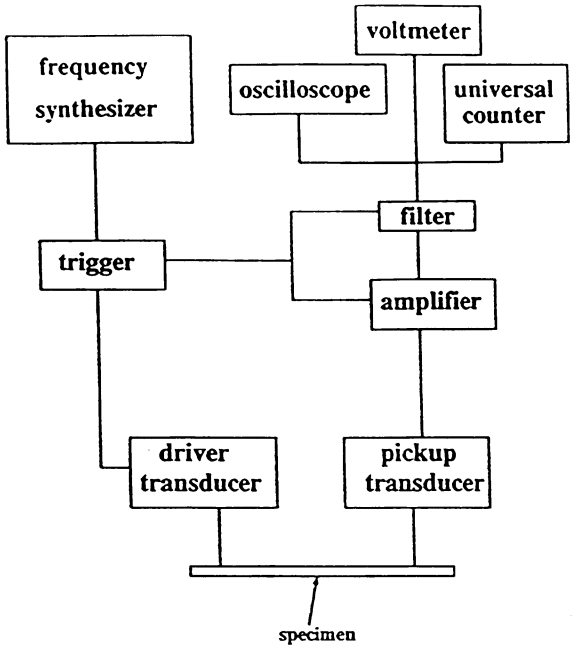

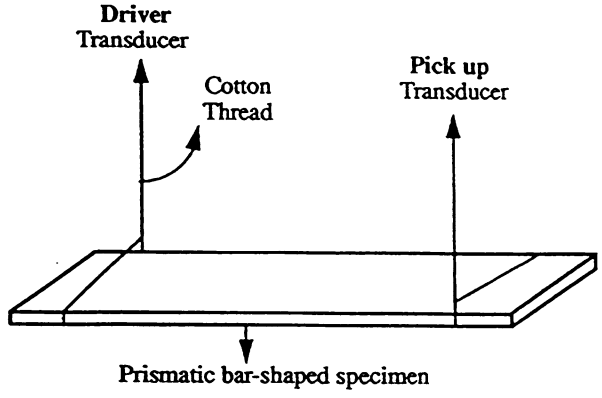

Fig.3 a) Experimental setup for the Young's modulus measurement
b) Method of suspending a specimen to obtain both the flexural and torsional frequencies.

3. BACKGROUND FOR THE YOUNG'S MODULUS MEASUREMENT

The measurements of the Young's modulus consist of matching the oscillator frequency with mechanical resonance vibration of the specimen. Both fundamental flexural and torsional resonance frequencies were measured for the specimens which were cold rolled into different reduction ratio and subjected to T6 treatment. Using the measured weight and dimensions of the specimens, the Young's and the shear modulus can be calculated from the flexural and torsional resonance frequencies, respectively.

The equation used for the calculation of the Young's modulus is that for the prisms of rectangular cross section provided by Pickett [13]. For the fundamental mode of vibration,

$$E = 0.94642(\ell^4/t^2)(\rho f^2)T \qquad 5)$$

where E = Young's modulus

ℓ = length of the specimen

t = thickness of the specimen

ρ = density of the specimen

f = fundamental flexural resonance frequency, and

T = shape factor which depends on the shape of the specimen.

The shape factor, T is given approximately by Spinner [14];

$$T = [\ 1 + 6.585(1+0.0752\nu+0.8109\nu^2)(t/\ell)^2 - 0.868(t/\ell)^4\ ] - \left[\frac{8.34(1+0.2023\nu+2.173\nu^2)(t/\ell)^4}{1 + 6.338(1+0.14081\nu+1.536\nu^2)(t/\ell)^2}\right] \quad 6)$$

where ℓ = length of the specimen

t = thickness of the specimen, and

ν = Poisson's ratio.

The shear modulus can also be calculated by measuring the torsional resonance frequency. The basic equation which relates torsional resonance frequency with the shear modulus is [13];

$$G = (2\ell/n)^2(\rho f'^2)\ R \quad 7)$$

where G = shear modulus

n = an integer which is unity for the fundamental mode, (two for the first overtone, etc.)

f' = torsional resonance frequency, and

R = shape factor which depends on the shape of the specimen.

For the prisms of rectangular cross section, the best approximation for R was obtained by Spinner and Tefft [15];

$$R = R_0[1+0.0085(nb/\ell)^2] - 0.06(nb/\ell)^{3/2}(b/a-1)^2 \quad 8)$$

where b = width of the specimen

a = thickness of the specimen, and

$$R_0 = \left[\frac{1+(b/a)^2}{4-2.521(a/b)\{1-1.991/[\exp(\pi b/a)+1]\}} \right] \qquad 9)$$

Poisson's ratio (ν) can be obtained from the measured E and G.

4. RESULTS

4.1 Effect of Cold Rolling on Microstructure

Cold rolling was carried out on the as-extruded composite, until edge cracks were observed on the specimens, to study the effects of mechanical working on the size and redistribution of $(Al_2O_3)_p$ clusters in these composites. Although 10 % of reduction in thickness per pass was used, the composite could be rolled up to about 75 % of reduction in thickness without edge cracking or surface scuffing. During cold rolling, the hardness of the composite increases rapidly with increasing reduction ratio, as shown in Fig.4. The rolled sheets of composites were cut and examined with SEM. A significant amount of particulate cracking and interfacial debonding were observed from the polished surfaces, as shown in Fig.5. There was strong tendency for the crack planes to be parallel to the direction of compression (i.e rolling pressure) and to be perpendicular to the rolling direction (i.e feed direction) as can be seen in Fig.6. The grid analysis performed on the micrographs taken from the rolled composites showed that the number of damaged $(Al_2O_3)_p$ increaseed linearly with increasing reduction ratio as illustrated in Fig.7. The substantial increase in rolling pressure, which is caused by the increase in hardness of the composite during cold rolling, was considered to be responsible for such crackings and debondings in the composites.

A considerable change in the distribution and shape of the $(Al_2O_3)_p$ clusters could be observed in the rolled composites. The most apparent difference in metallographic features between the as-extruded and the rolled composites is that the $(Al_2O_3)_p$, initially presented in

the form of banded clusters in as-extruded composite, becomes more uniformly distributed with increasing percent of reduction. The banded clusters of $(Al_2O_3)_p$ in the composite almost disappears at about 70 % reduction, as can be observed in the micrographs presented in Fig.8.

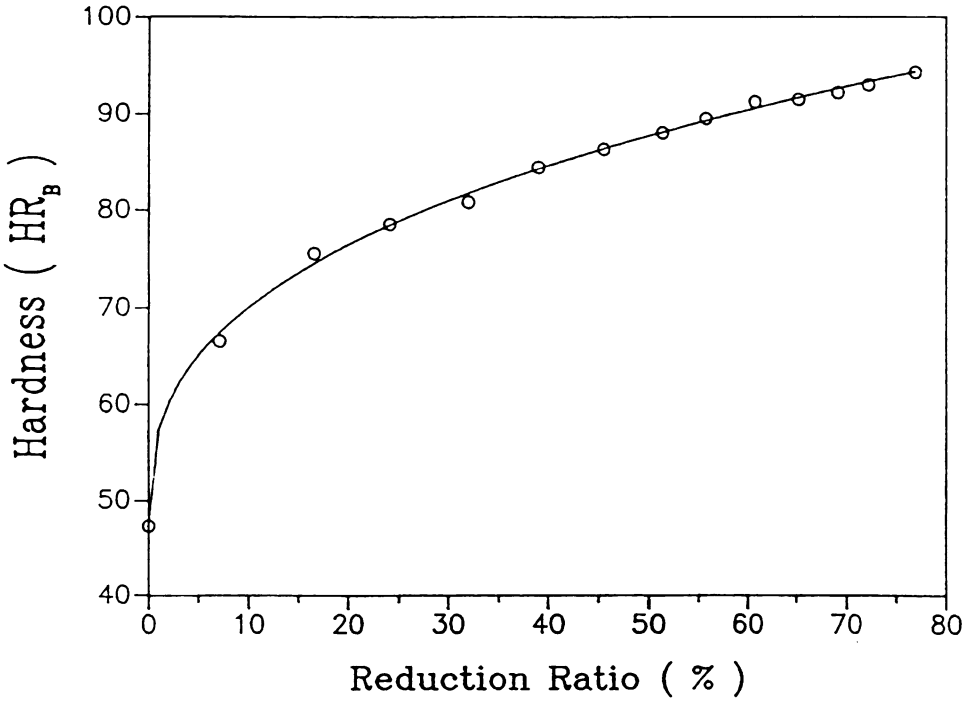

Fig.4 Plot of hardness of the cold rolled composite as a function of reduction ratio.

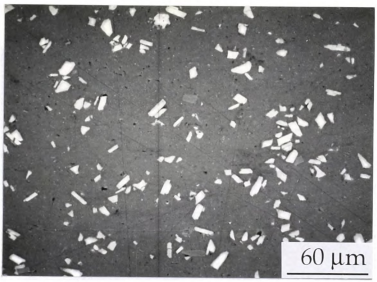

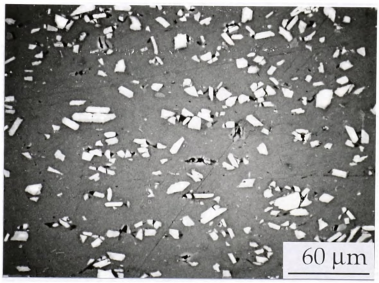

Fig.5 SEM micrographs of a) as-extruded (0%) and b) 60 % cold rolled composites. Note that 60 % cold rolled composite exhibits significant number of interfacial debonding and particulate cracking, while almost no crack damage can be seen on the as-extruded composite.

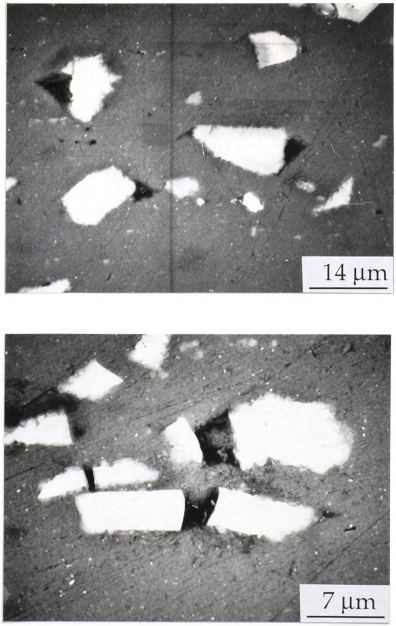

Fig.6 SEM micrographs illustrating a) interfacial debonding [D] and b) particulate cracking [C]. Note that crack planes are oriented perpendicular to the rolling direction.

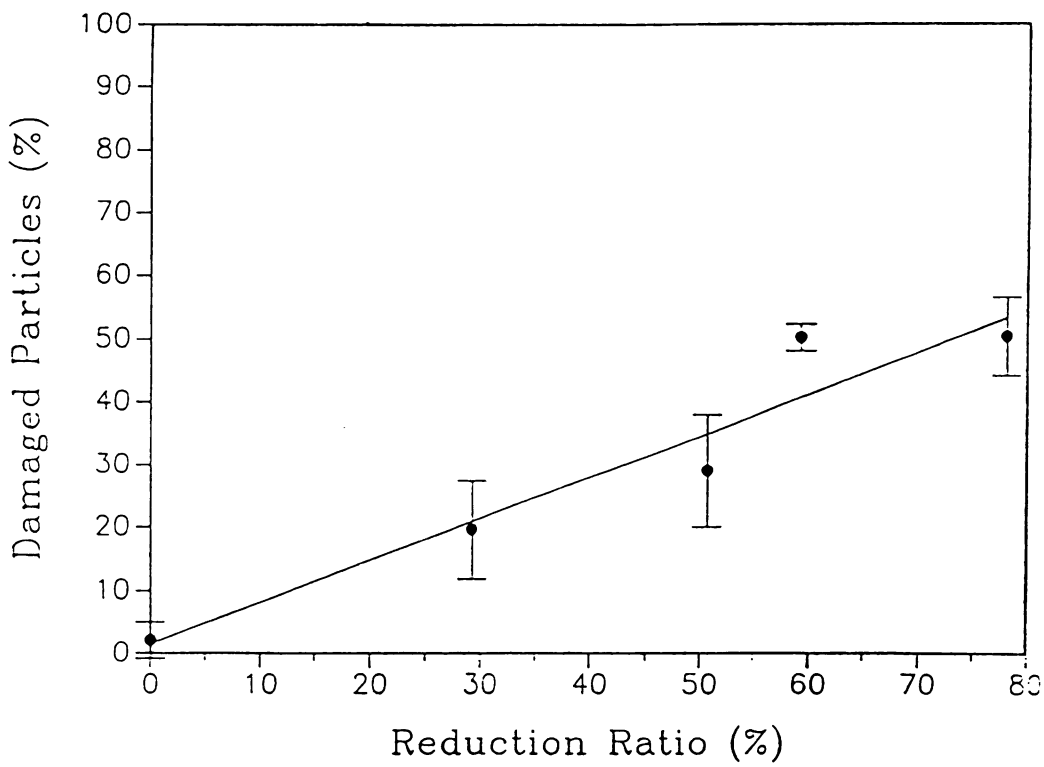

Fig.7 Plot of the percentage of damaged $(Al_2O_3)_p$ as a function of reduction ratio.

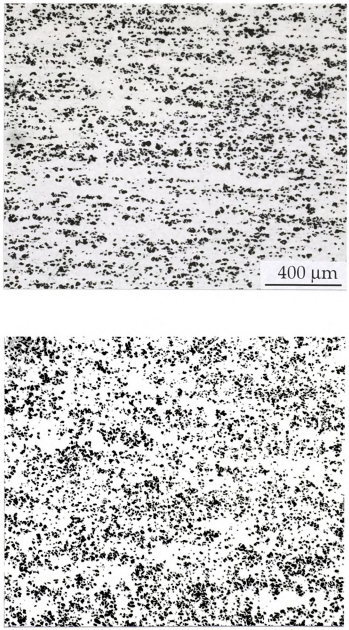

Fig.8 Optical micrographs exhibiting the distribution of $(Al_2O_3)_p$ clusters in; a) As-extruded, and b) 75% cold rolled composite.

4.2 Effect of Cold Rolling on Elastic Properties

Considerable increases in the Young's modulus (about 18 % for both L & T direction) and shear modulus (about 15-20 % depending on the directions) were measured in the as-extruded 6061 Al alloy reinforced with 10 % of $(Al_2O_3)_p$. The Young's modulus measured along the transverse direction of the as-extruded composite (transverse Young's modulus) was found to be slightly higher than that along the longitudinal direction (longitudinal Young's modulus). The transverse shear modulus was also higher than the longitudinal shear modulus. Some typical values of E, G, and ν of the unreinforced 6061-Al alloy and the as-received (as-extruded) composite are compared in Table.1.

The measured values of E and G as a function of reduction ratio are listed in Table.2, and are plotted in Fig.9. As illustrated in Fig.9(a), the longitudinal Young's modulus was observed to increase significantly at the early stages of cold rolling, and decrease afterwards. Nevertheless, the Young's modulus remains higher than that of the as-extruded composite even after 70 % of reduction. However, the transverse Young's modulus increases slightly at the early stages of cold rolling, and decreases afterwards.

The transverse Young's modulus becomes lower than that of the as-extruded composite after about 30 % of reduction. Similar features could also be observed for the shear modulus measured with respect to reduction ratio, as shown in Fig.9(b).

The shear modulus was found to be always higher along the transverse direction than along the longitudinal direction even after rolling. However, the Young's modulus was found to be higher along longitudinal direction than along the transverse direction except at

very small amounts of cold work: hence, under a given elastic stress the rolled composites should undergo less tensile deformation along the longitudinal direction, and less shear deformation along the transverse direction.

Table.1 Comparison of E, G, and ν between unreinforced 6061 Al-alloy and as-extruded composite, under T6 heat treated condition.

Material	direction	E (GPa)	G (GPa)	ν
6061 Al alloy	All	68.0	25.6	0.33
10 % $(Al_2O_3)_p$/Al	L	79.9	30.2	0.323
	T	80.7	31.7	0.274

All : random direction
L : longitudinal direction
T : Transverse direction

Table.2 Variation in the elastic properties of 10 % $(Al_2O_3)_p$/Al composite as a function of reduction ratio.
(Values obtained from the best fit curve)

Reduction Ratio (%)	E (GPa)		G (GPa)		ν	
	L	T	L	T	L	T
0	79.9	80.7	30.2	31.7	.32	.27
10	81.2	81.1	30.7	31.8	.33	.28
20	83.4	81.1	31.0	31.8	.34	.28
30	83.8	80.7	31.2	31.8	.34	.27
40	83.5	80.2	31.2	31.6	.34	.27
50	82.9	79.6	31.1	31.5	.33	.26
60	82.2	79.0	30.8	31.3	.33	.26
70	81.6	78.7	30.5	31.2	.33	.26

T : Transverse direction
L : Longitudinal direction

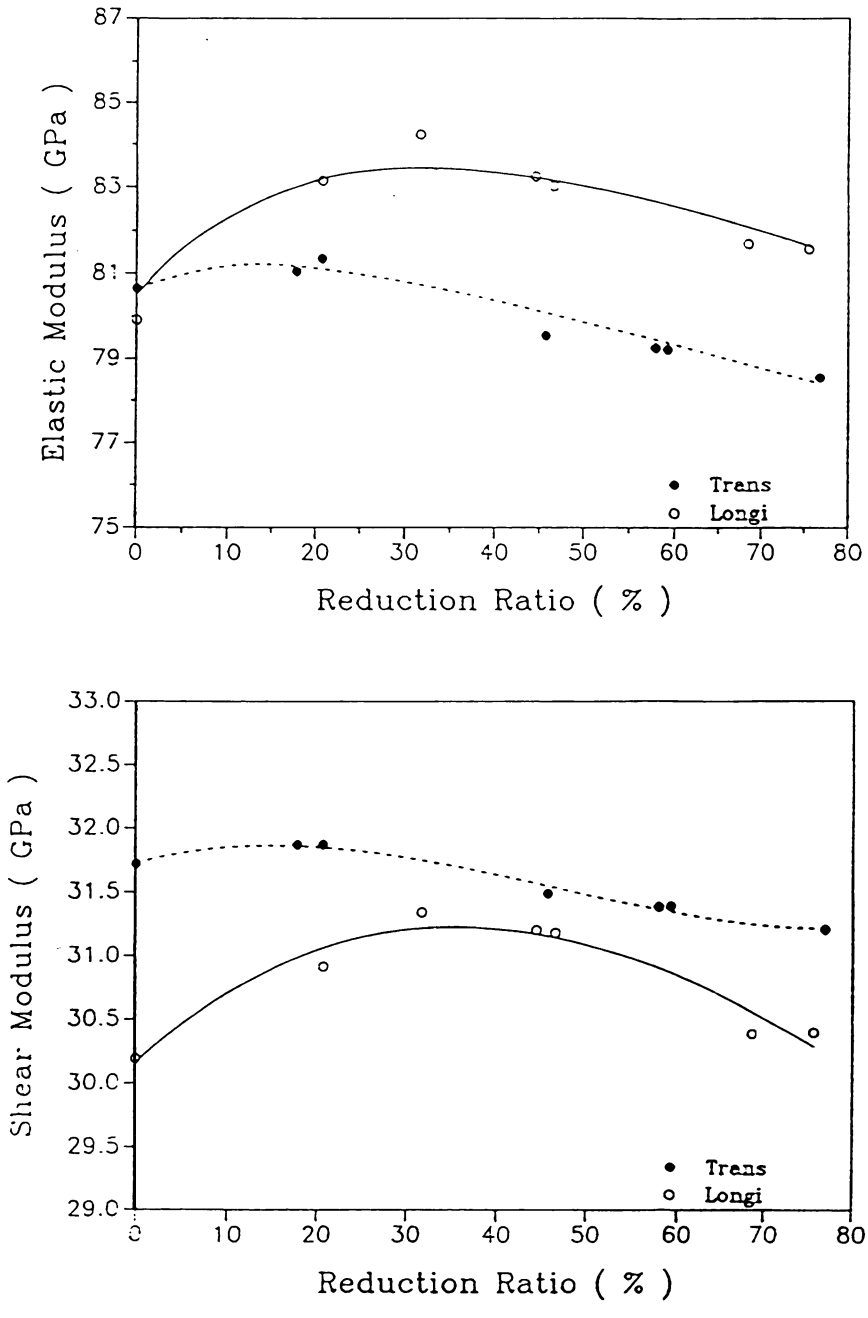

Fig.9 Plots of the experimentally obtained E and G as a function of reduction ratio along the longitudinal and transverse directions. All specimens were T6 treated before measurements.

a) Young's modulus vs. Reduction ratio

b) Shear modulus vs. Reduction ratio

5. DISCUSSION

5.1 Effect of porosity on the elastic properties

A quantitative assessment of the effect of porosity on various material properties, such as thermal conductivity, elastic properties, etc. has been carried out extensively in brittle materials, such as glass, ceramic, etc [16-18]. The following semi-empirical equations can be used to fit the experimental data on the relationship between the elastic properties and porosity.

$$U = U_o (1-\alpha P) \qquad 10(a)$$

$$U = U_o \exp(-\beta P) \qquad 10(b)$$

where U_o = value of elastic properties of pore-free material

U = value of elastic properties of material with porosity

P = the volume fraction of pore, and

α, β = the empirical constants.

The above equations illustrate that the elastic properties of the solid materials decrease with increasing volume fraction of porosity. They vary linearly for small (a few percent) volume fraction of porosity. The schematic illustration of such a relationship is shown in Fig.10(a).

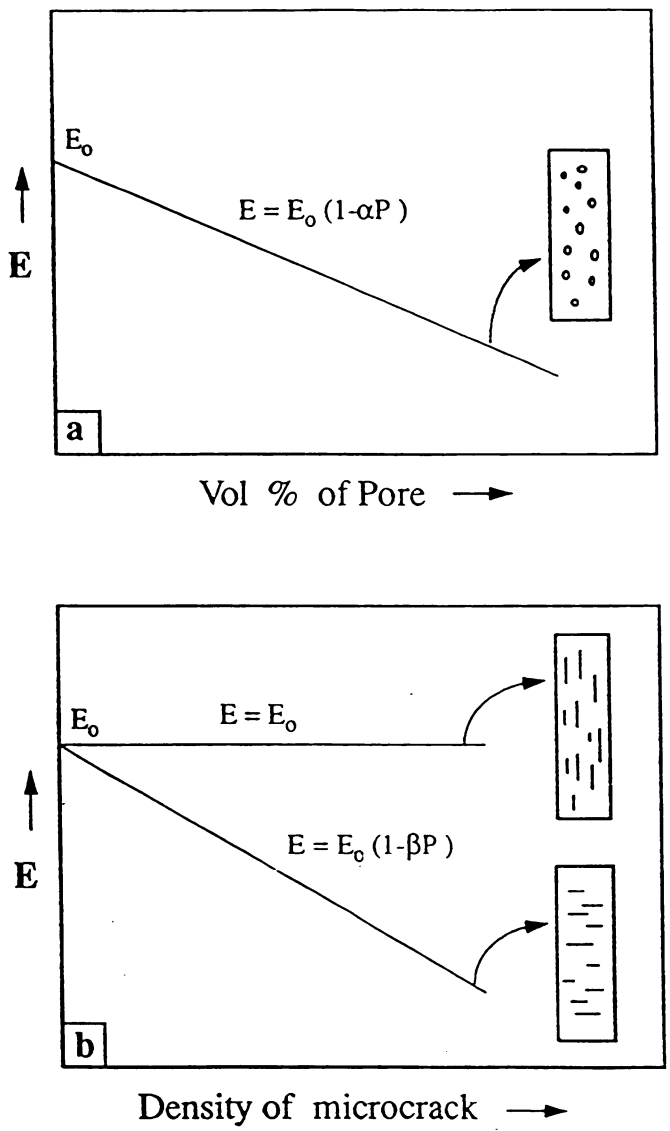

Fig.10 Schematics illustrating the effect of a) porosity and b) microcrack on the material properties.

5.2 Effect of microcrack on the elastic properties

A theoretical analysis of the effect of microcrack on various material properties, such as thermal conductivity, thermal stress resistance, elastic properties, etc., has also been well established in the field of brittle materials [19-21]. According to Hasselman [19], the relative effect of microcrack on a given material property, Q_o can be given in the general form

$$Q = Q_o [1 - \eta] \quad \text{or} \quad Q = Q_o [1 + \eta]^{-1} \qquad 11)$$

where Q_o = value of the material property of the crack-free material

Q = value of the material property of the microcracked material, and

η = a function of Poisson's ratio of crack-free material (ν_o), crack density, and crack shape.

The same expression can be used to investigate the effect of microcrack on the elastic properties. For a material having microcracks with crack plane oriented perpendicular to the uniaxial tension, the Young's modulus can be obtained by using the equation [21];

$$E = E_o [1 - F(\nu_o)\Phi] \qquad 12)$$

where E = Young's modulus of the microcracked material

E_o = Young's modulus of the crack free material

$F(\nu_o)$ = function of Poisson's ratio, depending on the shape of the microcrack (e.g $F(\nu_o) = 16(1-\nu_o^2)/3$ for penny shaped crack)

ν_o = Poisson's ratio of crack free material

Φ = crack density parameter given as $\Phi = (2N/\pi)[A^2/P]$

N = density of crack (mm^{-3})

A = crack area per crack, and

P = perimeter per crack.

However, for a material having microcracks with crack plane oriented **parallel** to the uniaxial tension, the Young's modulus of cracked material will almost be the same as that of crack-free material [19]. In other words, the propagation of the sonic waves is not impeded by the parallel crack. Thus,

$$E \approx E_o. \qquad 13)$$

As a summary, during uniaxial tensile loading, the Young's modulus is not influenced by microcracks oriented parallel to the direction of loading, but is affected by microcracks oriented perpendicular to the loading direction. Schematic illustrations of such features are given in Fig.10(b).

5.3 Effect of cold rolling on the elastic properties

Although cold rolling results in the uniform distribution of $(Al_2O_3)_p$ clusters with increasing reduction ratio (Fig.8), it does induce elliptical pore-like microcracks with crack plane oriented perpendicular to the rolling direction (Fig.6). Such pore-like microcracks include particulate crack, and interfacial debonding which can be considered as both crack and pore. In the present discussion, the effect of redistribution of $(Al_2O_3)_p$ and pore-like microcracks on the variation of the elastic properties of the composite, especially the Young's modulus, will be considered. Since the crack planes of microcracks, developed within transverse specimen, are oriented perpendicular to tensile direction, the transverse Young's modulus of the rolled composites will decrease due to pore-like microcracks according to Eq 9). However, the effect of such microcracks on the longitudinal Young's modulus will not be as significant as that on the transverse ones, since the crack planes are oriented parallel to the direction of the propagating wave. On the other hand, the redistribution of $(Al_2O_3)_p$ and possibly the texture formation, achieved by rolling, is considered to attribute to the increase in both the longitudinal and the transverse Young's modulus due to the fine dispersion of $(Al_2O_3)_p$ and break-up of clusters. Analytical expressions concerning the contribution of the both parameters on the Young's modulus can be obtained from the curve fitting of the data points for the transverse specimens under the following assumptions;

a. Only the redistribution and the microcracks of $(Al_2O_3)_p$ act as the influencing factors for the changes in the Young's modulus.

b. The orientation of each $(Al_2O_3)_p$ in the longitudinal and the transverse specimens does not affect the Young's modulus of the composite.

The best fit curve for the experimentally measured values of Young's moduli was found to have the form of

$$E = E_o (1 + \alpha x^{\beta} - \gamma x) \qquad 14)$$

where E = Young's modulus of the composite

E_o = Young's modulus of the as-extruded composite

X = reduction ratio, which is related with volume percent of pore-like microcrack, and

α, β, γ = constants to be determined from experimental data.

In this equation, $E_o(1 + \alpha x^{\beta})$ corresponds to the contribution due to the redistribution of $(Al_2O_3)_p$, and $E_o(1 - \gamma x)$ corresponds to the effect due to the pore-like microcracks. The contribution due to the pore-like microcracks is more significant in transverse direction, as illustrated in Fig.11. This is to be expected based on the orientation of the microcracks (introduced by cold work) relative to the tensile direction. As a result, the transverse Young's modulus of cold rolled composite is smaller than the longitudinal Young's modulus. If the damage on $(Al_2O_3)_p$ could be eliminated efficiently during rolling, the rolling operation can result in an increase in the Young's modulus of the composite (according to $E = E_o[1 + \alpha x^{\beta}]$) due to breaking up of banding and clustering so as to provide uniform distribution of $(Al_2O_3)_p$.

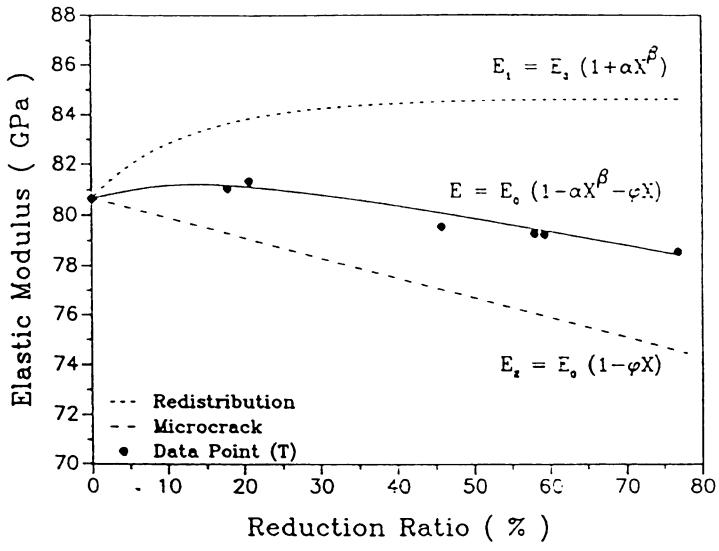

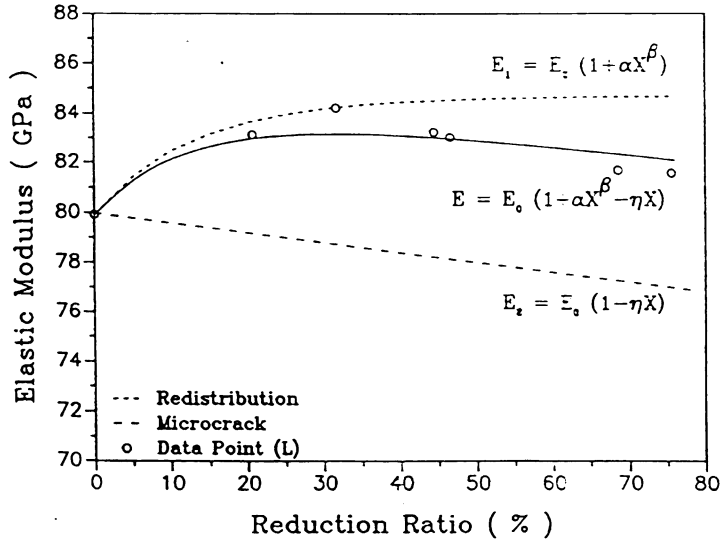

Fig.11 Plots of analytical expressions for the effect of redistribution of $(Al_2O_3)_p$ and pore-like microcracks on the Young's moduli along the a) Transverse and b) Longitudinal direction of the composites. Note that the effect of pore-like microcracks on the Young's modulus is less significant in longitudinal than in transverse directions.

6. SUMMARY

Following statements summarize the results of cold rolling carried out on extruded $(Al_2O_3)_p$/Al composite.

6.1 Microstructural features

Significant redistribution of $(Al_2O_3)_p$ clusters could be achieved with increasing reduction ratio by cold rolling. The composite could be rolled down to as much as 75 % of reduction in thickness without forming any edge crackings or surface scuffings, indicating good cold formability. The banded structure of $(Al_2O_3)_p$ clusters present in the as-extruded composite almost disappeared beyond about 60-70 % of reduction. Both particulate cracking and interfacial debonding were observed from the rolled composite. There is strong tendency for the crack planes to be formed perpendicular to the rolling direction. The extent of such damage in $(Al_2O_3)_p$ increases linearly with increasing reduction ratio.

6.2 Elastic properties

The measured Young's modulus and the shear modulus of the as-extruded composite were considerably higher than those of the unreinforced Al alloy. Although the longitudinal Young's modulus of the cold rolled composite was higher than the transverse one, the shear modulus was found to be always higher along the transverse direction than along the longitudinal direction. Both the redistribution of $(Al_2O_3)_p$ and the pore-like microcracks were found to affect the elastic properties of the composite. The analytical

expressions which account for the contribution of both parameters on the elastic properties were obtained by using curve fitting method; the effect of pore-like microcrack on the Young's modulus was found to be in the form of $E = E_o(1 - \gamma x)$, and the effect of redistribution of $(Al_2O_3)_p$ on the Young's modulus has the form of $E = E_o(1 + \alpha x^{\beta})$, where x and E_o represent the reduction ratio and the Young's modulus of the as-extruded composites, respectively.

7. REFERENCES

1. D.R.Flinn, "Metal matrix composites", The New Materials Society, 2, Bureau of Mines, p 6.1-6.23, (1990).

2. T.W.Chou, A.Kelly and A.Okura, "Fiber-reinforced metal matrix composites", Composite, 16, 187-206, (1985).

3. C.F.Lewis, "The exciting promise of metal matrix composites", Material Eng., 103, 33-37, (5.1986).

4. J.C.Bittence, Adv. Mater. and Process, 131, 39-63, (1987).

5. S.R.Lampman, Adv. Mater. and process, 138, 17-22, (1991).

6. H.Ohtsu, "Aluminum alloys matrix composites using particle dispersion", Proceeding of the Fifth Annual ASM/EDS Advanced Composites Conference, Detroit, Michigan, Oct. 1989, pp 187-199, published by ASM International, Materials Park, Ohio, (1989).

7. K.Marsden, "Commercial potentials for composites", J. Metals, 37, 59-62, (6.1985).

8. T.R.Pritchett, "Advanced technology aluminum materials for aerospace application", Light Metal Age, 44, 10-19, (10.1986).

9. K.S.Ravichandran and E.S.Dwarakadasa, "Advanced aerospace Al alloy", J.Metals, 39, 28-32, (6.1987).

10. J.C.Lee and K.N.Subramanian, "Rolling of SiC_p reinforced Aluminum alloy composites", Proceeding of the Sixth Annual ASM/EDS Advanced Composites Conference, Detroit, Michigan, Oct. 1990, pp 575-583, published by ASM International, Materials Park, Ohio, (1990).

11. F.N.Rhines and B.R.Patterson, "Effect of the degree of prior cold work on the grain volume distribution and the rate of grain growth of recrystallized aluminum", Metall. Trans. A, 13, 985-993, (1982).

12. H.L.Walker, Univ. Illinois Engineering Experiment Station Bullitin, No.359, University of Illinois, (1945).

13. G.Pickett, "Equations for computing elastic constants from flexural and torsional resonant frequencies of vibration of prisms and cylinders", Am. Soc. Testing Mats. Proc., 45, 846-865, (1945).

14. S.Spinner, T.W.Reichard and W.E.Tefft, Journal of Research, National Bureau of Standards, 64A, 147-155, (1960).

15. S.Spinner and W.E.Tefft, "A method for determining mechanical resonance frequencies and for calculating elastic mudulus from these frequencies", Am. Soc. Testing Mats. Proc., 61, 1221-1238, (1961).

6. V.D.Krstic and W.H.Erickson, "A medel for the porosity dependence of Young's modulus in brittle solids based on crack opening displacement", J. Mater. Sci., 22, 2881-2886, (1987).

17. S.K.Dutta, A.K.Mukhopadhyay and D.Chakraborty, "Assessment of strength by Young's modulus and porosity: A critical evalution", J. Am. Ceram. Soc., 71, 942-947, (1988).

18. H.M.Chou and E.D.Case, "Characterization of some mechanical properties of polycrystalline yttrium ion garnet (YIG) by non-destructive methods", J. Mater. Sci. Lett, 7, 1217-1220, (1988).

19. D.P.F.Hasselman and J.P.Singh, "Analysis of thermal stress resistance of microcracked brittle ceramics", Am. Cer. Soc. Bulletin, 856-860, (1979).

20. H.J.Siebeneck, J.J.Cleveland, D.P.H.Hasselman and R.C.Bradt, "Effect of grain size and microcracking on the thermal diffusivity of $MgTi_2O_5$", J. Am. Ceram. Soc., 60, 336-338, (1977).

21. B.Budiansky and R.J.O'connell, "Elastic moduli of a cracked solid", Int. J. Solids and structures, 12, 81-97, (1976).

CHAPTER V.

EFFECT OF COLD ROLLING ON THE TENSILE PROPERTIES OF $(Al_2O_3)_p$/Al COMPOSITES

This chapter is based on the paper that has appeared in Material Science and Engineering, A159, 43-50, 1992. The following is the abstract of the original publication.

Cold rolling of extruded 6061 Al alloy composite reinforced with 10 % of Al_2O_3 particulates along the transverse direction results in more uniform distribution of the particulates. This rolling is associated with a considerable amount of damage to the particulates. Room temperature tensile tests carried out on the rolled composites showed, with increasing reduction in rolling, significant decrease in strength and insignificant change in fracture strain along the longitudinal (extruded) direction. However, the same properties increased with increasing reduction in rolling along the transverse (rolling) direction. Such behaviors of rolled composites are analyzed on the basis of redistribution of the particulate clusters, disappearance of the particulate free zones, particulate damage, and the contribution of the individual particulate to the strengthening with the achievement of uniform distribution.

1. INTRODUCTION

Some modern engineering applications require materials with high strength and stiffness as well as good elevated temperature properties. Various types of metal matrix composites reinforced with ceramic particulates are being developed to meet such demands. However, the addition of these particulates also results in substantial decrease in ductility, limiting their wider use. Several processing techniques [1-3] have been studied to improve the ductility and the fracture toughness of metal matrix composites reinforced with various ceramic particulates. In spite of recent developments and improvements in the processing of these composites, non-uniform distribution (and clustering) of the reinforcements are of major concern due to their undesirable effects on the mechanical behavior of the composites. Such problems could be overcome by mechanical working of the composites, since the size, shape, and distribution of particulate clusters, which had formed during manufacture, can be altered by additional mechanical processing.

The present study deals with the effects of cold rolling on the microstructural changes of Al alloy composite reinforced with Al_2O_3 particulates [$(Al_2O_3)_p$/Al composite] and its influence on the tensile properties. An understanding of these effects would be useful in optimizing the tensile properties of the resultant composites and making them more suitable for engineering applications.

2. EXPERIMENTAL PROCEDURE

Duralcan composite (W6A 10A) with 6061 aluminum alloy reinforced with 10 % of $(Al_2O_3)_p$, obtained as extruded cylindrical bars, was used in this study. In the as-received composite, $(Al_2O_3)_p$ has the blocky platelet shape with an average size of 10 μm and with aspect ratio of about 2. General morphology and the size distribution of $(Al_2O_3)_p$ are shown in Figs.1 and 2. The stock material was cut, annealed at 560°C for 30 min. and then rolled unidirectionally with 10 % reduction in thickness per pass in a direction perpendicular (transverse) to the extrusion (longitudinal) direction. Each sheet was cold rolled to a different final reduction (up to 75 %) without any intermittent stress relief annealing. Tensile test specimens with the dimensions of 20 x 6.5 x 0.9 mm were machined from the rolled sheets, and then T6 heat treated before tensile testing. The specimens were solutionized at 560°C for 60 min, aged at room temperature for 65 hours, followed by artificial aging at 170°C for 14 hours to obtain peak hardness in T6 condition. The side-surfaces of the tensile test specimens were polished with 600 grit abrasive paper followed by lapping on rotating wheels. Room temperature tensile testing was carried out at a constant cross-head speed of 0.1 cm/min. in air. The fractured tensile test specimens were examined by optical and scanning electron microscopy.

Fig.1 Morphology of $(Al_2O_3)_p$. Small crystals present on the of $(Al_2O_3)_p$ are $MgAl_2O_4$ spinel formed at the interface composite manufacture. (The specimen for this study w prepared by removing the matrix electrolytically.)

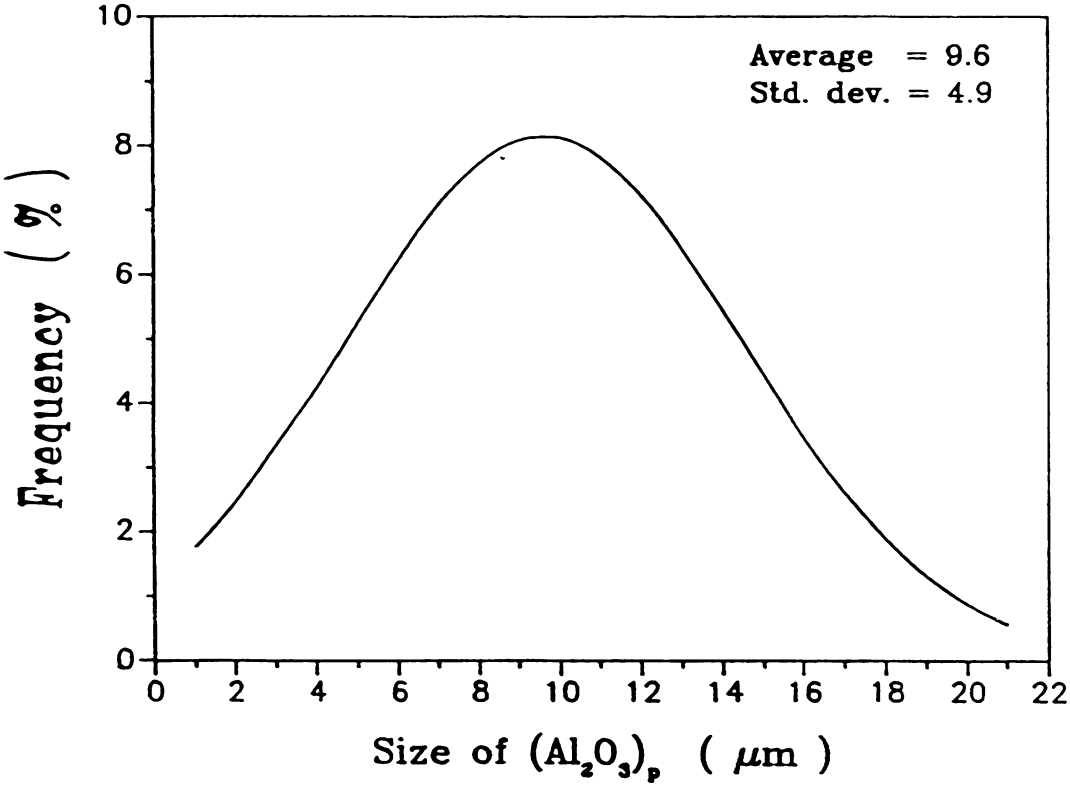

Fig.2 Size distribution of $(Al_2O_3)_p$ within the $(Al_2O_3)_p$/Al composite.

3. RESULTS

3.1 Effect of cold rolling on the microstructural Features

The most apparent difference in metallographic features of the as-extruded (as-received) and the rolled composites is that $(Al_2O_3)_p$, present as a banded structure in as-extruded material, becomes more uniformly distributed with increasing reduction ratio. At the same time, the presence of $(Al_2O_3)_p$ free zones with the width of 100 to 200 μm (occasionally 300 to 400 μm) in the as-extruded composite become narrower and ultimately disappear with increased reduction in rolling. In spite of these significant changes in the distribution of $(Al_2O_3)_p$ clusters, the orientation of each $(Al_2O_3)_p$ (initially aligned parallel to the extrusion direction) was not altered substantially even after the rolling operation. Differences in the microstructural features of as-extruded and 60 % rolled composites are compared in Fig.3. Detailed micrographs showing such a redistribution of the particulate reinforcements due to cold rolling are given elsewhere [4,5]. However, this uniform distribution of $(Al_2O_3)_p$ observable in cold rolled composites is accompanied by a considerable amount of particulate cracking and interfacial debonding. This particulate cracking and interfacial debonding (Fig.4) formed during cold rolling did not appear to be healed even after solution treatment.

There was a strong tendency for the cracks in the particulates to be formed perpendicular to the rolling direction. The extent of damaged $(Al_2O_3)_p$, either in the form of particulate cracking or interfacial debonding, increases linearly with increasing reduction ratio of cold rolling, such that the fraction of damaged particles

increases from 2 % in as-extruded composite to about 50 % in 70-80 % cold rolled composite. Such particulate cracking and interfacial debonding of $(Al_2O_3)_p$ within the composites are probably due to a substantial increase in rolling pressure, which is associated with an increase in the hardness of the matrix during cold rolling. Detailed micrographs and discussion on the damage of $(Al_2O_3)_p$ due to cold rolling are provided elsewhere [4].

3.2 Effect of cold rolling on the tensile properties

The graphical results for the variations in the tensile properties with respect to the reduction ratio are shown in Fig.5. The tensile properties of the **as-extruded** $(Al_2O_3)_p$/Al composites along the longitudinal and transverse directions were found to be anisotropic. Such anisotropy is due to the microstructural inhomogeneity observable in the as-extruded composites, as can be seen in Fig.3. The cracks formed due to tension propagate directly through $(Al_2O_3)_p$ clusters without large plastic deformation of the matrix, as can be observed on the side-surfaces of fractured transverse tensile test specimens made out of as-extruded composites (Fig.6). This feature will lower the ductility and strength along the transverse direction as compared with the longitudinal direction of the composite.

Significant redistribution of $(Al_2O_3)_p$ achieved with increasing reduction in rolling resulted in increase in strength and fracture strain along the **transverse** direction. However, along the **longitudinal** direction, the strength decreased and the fracture strain remained relatively unaffected, under similar conditions. Similar

trends have also been observed in 6061 Al alloy composite reinforced with SiC particulates [5]. Although other published results [6-10] are consistent with these findings, no attempt has been made to explain such a behavior.

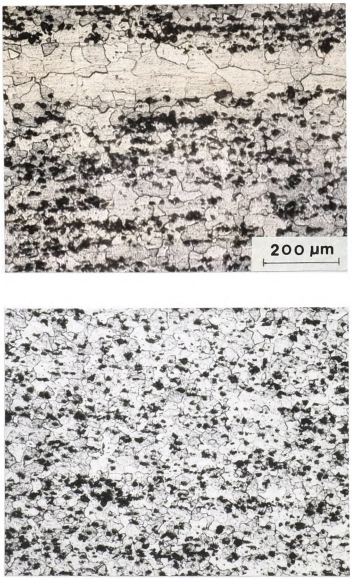

Fig.3 Micrographs of a) as-received composite, showing microstructural inhomogeneities, such as banded $(Al_2O_3)_p$ and larger matrix grains in particulate free zones, observed in as-extruded (as-received) composite, and
(b) 60 % cold rolled composite, showing more uniform distribution of $(Al_2O_3)_p$ and smaller recrystallized grains seen in the cold rolled composite.

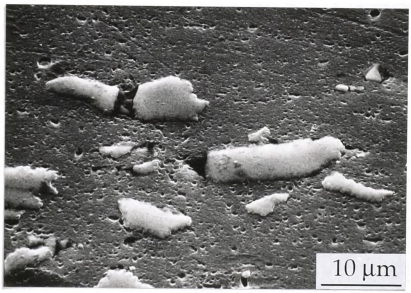

Fig.4 Particulate cracking [C] and interfacial debonding [I] due to rolling. The arrow indicates the rolling direction.

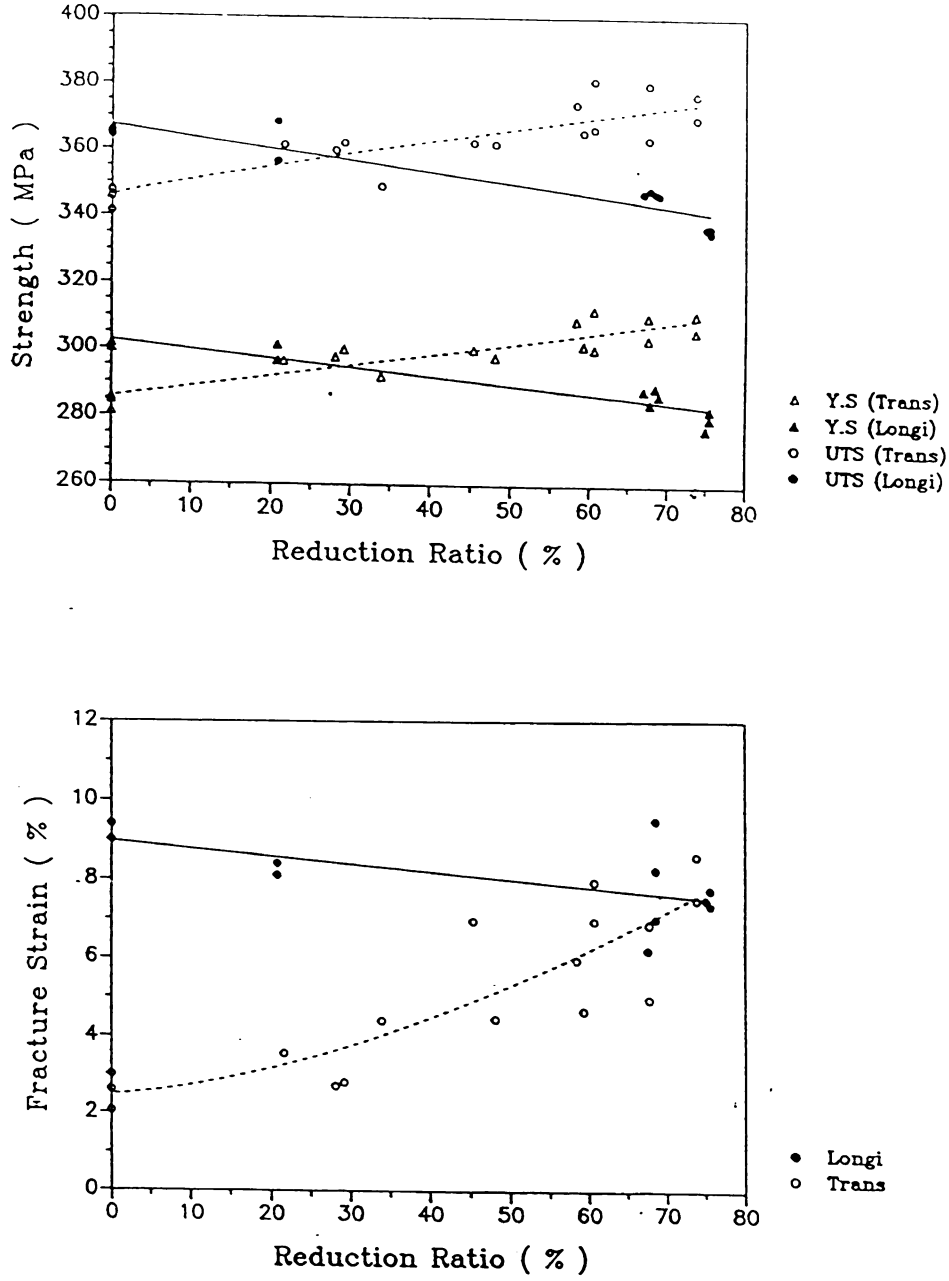

Fig.5 Plots illustrating the variations in tensile properties as a function of reduction ratio. The solid and broken lines are the best fit curves for the data points.

a) Strength vs. Reduction ratio.

b) Fracture strain vs. Reduction ratio.

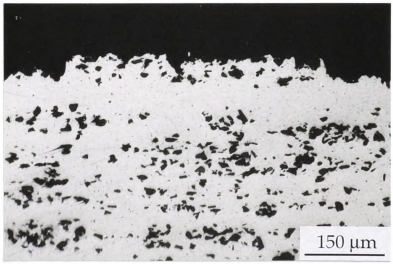

Fig.6 Micrograph taken from the side surface of the fractured transverse tensile test specimen prepared from the as-received composite. Direct propagation of the major crack through the $(Al_2O_3)_p$ clusters can be seen.

4.ANALYSIS

Redistribution of $(Al_2O_3)_p$ clusters, disappearance of $(Al_2O_3)_p$ free zones, higher stress concentration at $(Al_2O_3)_p$ within the clusters, and the damage of $(Al_2O_3)_p$ are responsible for the observed changes in tensile properties. As more uniform distribution of $(Al_2O_3)_p$ is achieved, the orientation of $(Al_2O_3)_p$ with respect to the axis of loading also has a considerable effect on the tensile properties along the longitudinal and transverse direction. Each of these parameters, as affected by rolling, could either improve or deteriorate the tensile properties along different directions of the resultant composite. In this particular paper, the role of some of these parameters, especially redistribution of $(Al_2O_3)_p$, on the change in the tensile strength of the composite are considered.

4.1 Effect of redistribution of $(Al_2O_3)_p$ on the tensile strength

4.1.1 Composite Model:

As the cold rolling causes more uniform distribution of the particuates, the tensile properties should become more isotropic (in the rolling plane) with increased amount of reduction. In order to analyze the effect of particulate redistribution on the tensile properties, especially the observed increase and decrease in strength along the transverse and the longitudinal directions, a simplified two dimensional composite model based on the following assumptions is considered:

a. The extruded composite can be treated as a discontinuous fiber reinforced composite, where the fibers correspond to the banded structure (with particulates clustering and stringing together) along the extrusion direction. In this analysis, such regions are termed as 'fiberils',
b. The strength of these fiberils can be considered to be the strength of those regions with associated higher volume fraction of $(Al_2O_3)_p$,
c. The effective yield strength of the fiberils as a function of the volume fraction of $(Al_2O_3)_p$ can be obtained from the experimentally measured and extrapolated regions in the plot given in Fig.7,
d. $(Al_2O_3)_p$ free regions are the matrix with the yield strength of the Al alloy (240 MPa), and
e. The individual particulate geometry does not contribute to the observed strength variation addressed in this model.

Based on the microscopic studies of the as-extruded composite, the approximate dimensions of these fiberils are about 300 μm in length, with an average width of about 50 μm. These fiberils are spaced approximately 100 μm apart along the transverse direction, and they are spaced closely along the longitudinal direction. The fiberils are treated as rectangular regions in the two dimensional sketch provided for the analysis. $(Al_2O_3)_p$ volume fractions as high as 30 to 35 % have been observed in these banded regions. The schematic of this composite is shown in Fig.8(a). Rolling along the transverse direction spreads $(Al_2O_3)_p$ present within the fiberils along the transverse direction without changing the fiberil length along the

longitudinal direction (due to the plane strain condition during rolling). Such a redistribution of $(Al_2O_3)_p$ within the fiberil will decrease the strength of the fiberil due to decrease in volume fraction of $(Al_2O_3)_p$. With a significant amount of reduction in rolling, uniform distribution of $(Al_2O_3)_p$ in the matrix could be achieved. The schematics illustrating these features are provided in Figs.8(b) and (c).

4.1.2 Variation in strength along the longitudinal direction:

In a discontinuous fiber reinforced composite, the strength of the fiber, along the direction parallel to the fiber, can be achieved fully only when the aspect ratio (ℓ/w) satisfies

$$\frac{\ell}{w} > \frac{\sigma_f}{2\tau} = \frac{\ell_c}{w} \qquad 1)$$

,where ℓ is the length of the fiber

w is the width (or diameter) of the fiber

σ_f is the yield strength of the fiber

τ is the shear strength of the interface, and

ℓ_c is the critical fiber length.

For the fiberil present in the as-extruded composite, the critical aspect ratio (ℓ_c/w) is about 2, based on the strength of the fiberils assumed to be about 500 MPa. This strength is an assumed value based on the observation that provide 30 to 35 % $(Al_2O_3)_p$ in the banded

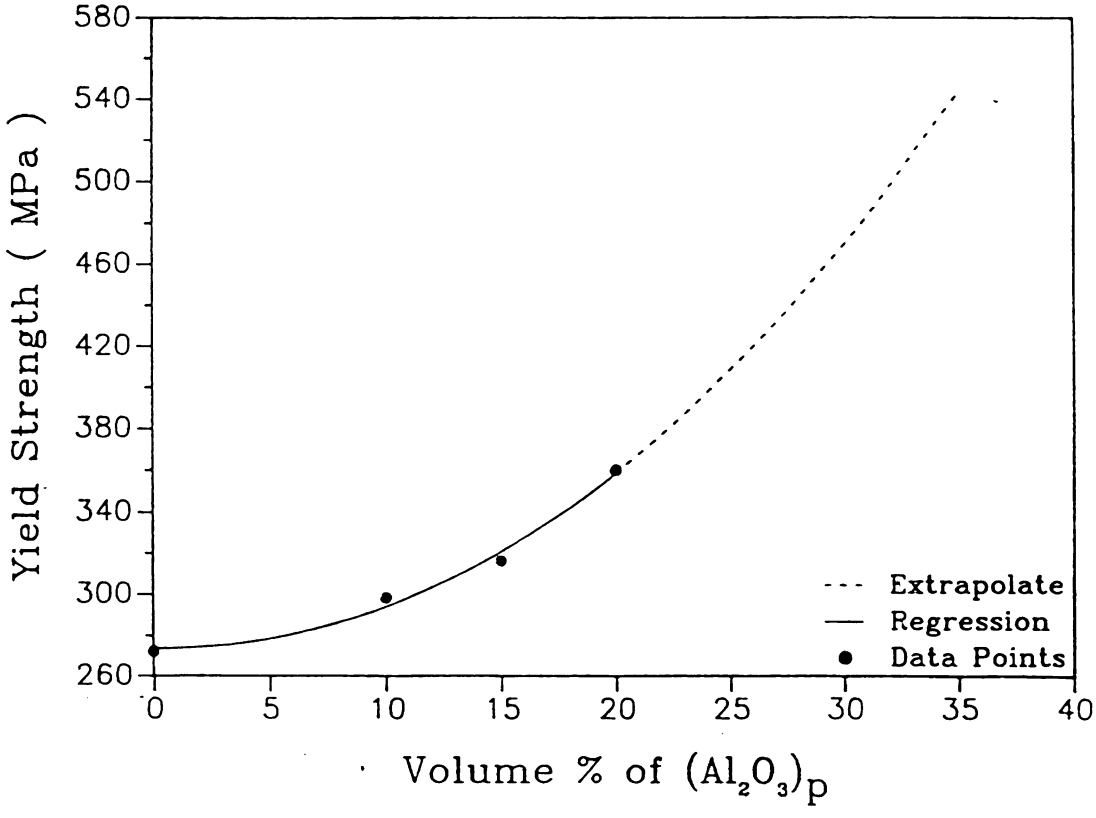

Fig.7 Yield strength of 6061-Al alloy composite reinforced with various volume fraction of $(Al_2O_3)_p$. The broken portion of the plot is obtained by extrapolating the best fit solid curve.

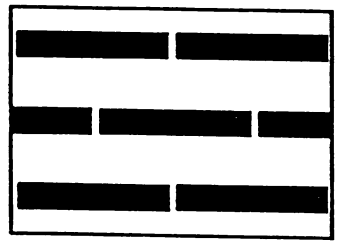

a) 0% Rolled

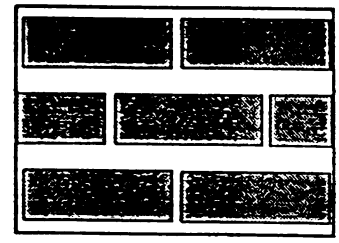

b) Intermediate stage

c) Later stage

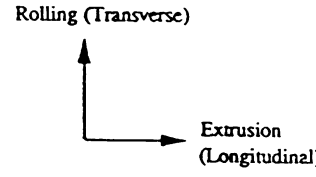

Fig.8 Schematic illustration of the two dimensional composite model used for the analysis.
a) As-extruded (0 % rolled) composite exhibiting the banded structure of $(Al_2O_3)_p$: Each fiberil possesses 30-35 % $(Al_2O_3)_p$
b) Intermediate stage in the cold rolled composite (corresponds to 30-40 % cold rolling in the system considered)
c) Later stage in the cold rolled composite exhibiting uniform distribution of $(Al_2O_3)_p$ (corresponds to about 70 % cold rolling in the system considered)
Each fiberil in all stages possesses same number of $(Al_2O_3)_p$.

region, and from the plot given in Fig.7. The shear strength of the interface (τ) is assumed to be the shear stress required to cause plastic deformation of the Al alloy matrix (about 120 MPa). In the as-extruded composite, the aspect ratio of the fiberil is measured to be about 10. As a result, strength of the composite along the longitudinal direction will approach that for a continuous fiber reinforced composite.

With rolling along the transverse direction, the fiberil width increases without altering its length. This decreases the volume fraction of $(Al_2O_3)_p$ within the fiberil, decreasing the effective strength of the fiberil according to the plot given in Fig.7. Therefore, the decrease in strength of the rolled composite along the **longitudinal** direction arises due to decrease in the strength of the fiberils, which reduce the load carrying capability of the fiberils [Fig.9(a)]. Although this lateral spreading of the fiberils will decrease the aspect ratio (responsible for longitudinal strengthening), it will still be significantly larger than the critical aspect ratio, providing a composite strength approaching that for continuous fiber reinforcement.

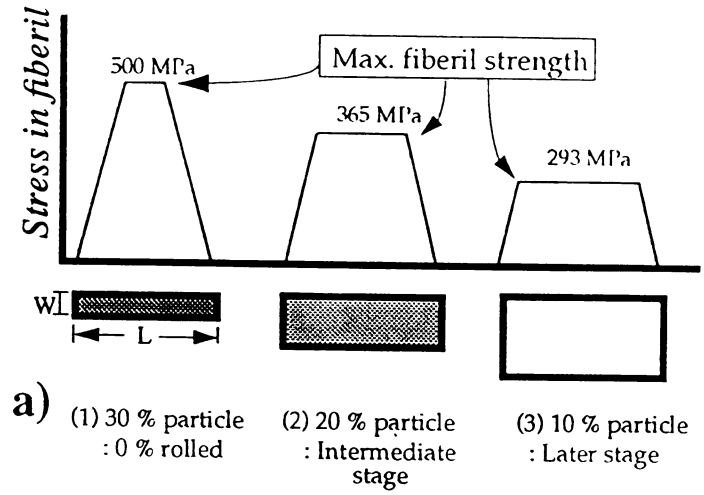

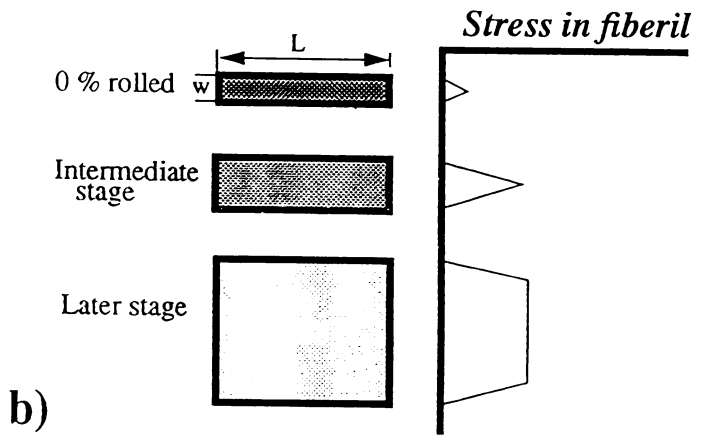

Fig.9 a) Variation in stress distribution along the length of a fiberil in the composite which is subjected to uniaxial tension along the longitudinal direction.

b) Variation in stress distribution along the width of a fiberil in the composite which is subjected to uniaxial tension along the transverse direction.

4.1.3 Variation in strength along the transverse direction:

Along the transverse direction, the aspect ratio of the fiberil within the as-extruded composite, relevant to strengthening in that direction, will be much smaller than the critical aspect ratio. As a result, these fiberils do not contribute to significant strengthening along the transverse direction. However, redistribution due to rolling will increase the aspect ratio responsible for the strengthening along the transverse direction, although it does not reach the critical aspect ratio. Such features are illustrated in Fig.8. Thus, the increase in strength along the transverse direction, with respect to the gradual redistribution of $(Al_2O_3)_p$, is due to the following two contributions:

a. Increase in the aspect ratio (w/ℓ), which increases the load carrying capability of the fiberil by increasing the average stress in the fiberil [11,12], is reflected as the increased strength in this direction. Such features illustrating the increasing load carrying capability of the fiberil are shown in [Fig.9(b)].
b. In addition, the stress concentration at the particulates (presented in the banded region) will be reduced with the redistribution of particulates achieved by cold rolling, minimizing the particulate damage during tensile testing along the transverse direction. Such a feature will also enhance the strength along the transverse direction with increased amounts of cold work.

4.1.4 Calculations:

The rule of mixture for parallel and series alignments of fiberils is applied to make a rough estimation of the strength based on the composite models provided in Fig.8. The data needed for the calculations and resultant strengths corresponding to Fig.8 are listed in Table.1. The relationship between the particulate redistribution and the yield strength of the composite based on these calculations is shown in Fig.10. The comparison between the predicted and the measured strength, with increasing reduction in rolling, are provided as "the percent change in strength" in plots given in Fig.11 so as to check the trend observed in Fig.5(a). The change in longitudinal strength presented by the model agrees well with the experimental observations. However, along the transverse direction, significant mismatch exists between the measured and the predicted change in strength, although both show an increasing tendency with increasing amount of rolling.

Table.1 Data used for the calculations of the strength of the composite along the longitudinal and the transverse directions.

Vol. % of $(Al_2O_3)_p$ in fiberils	Strength of fiberil and matrix	Vol. % of fiberil and matrix	Strength of composite
30 % (As-extruded)	σ_f = 460.0 MPa σ_m = 240.0 MPa	V_f = 33.3 % V_m = 66.7 %	σ_ℓ = 313.3 σ_t = 285.5
20 %	σ_f = 365.0 MPa σ_m = 240.0 MPa	V_f = 50.0 % V_m = 50.0 %	σ_ℓ = 302.5 σ_t = 289.0
15 %	σ_f = 327.2 MPa σ_m = 240.0 MPa	V_f = 66.7 % V_m = 33.3 %	σ_ℓ = 298.2 σ_t = 291.9
10 % (70 % rolled)	σ_f = 295.0 MPa σ_m = 240.0 MPa	V_f = 100 % V_m = 0 %	σ_ℓ = 295.0 σ_t = 295.0

Note:

a. σ_f and σ_m denote the strength of the fiberil and matrix, respectively, and σ_ℓ and σ_t denote the strength of the composite along the longitudinal and the transverse directions, respectively.

b. Rule of mixture for longitudinal direction ; $\sigma_\ell = \sigma_f V_f + \sigma_m V_m$

c. Rule of mixture for transverse direction ; $\sigma_t = \dfrac{\sigma_f \sigma_m}{\sigma_f V_f + \sigma_m V_m}$

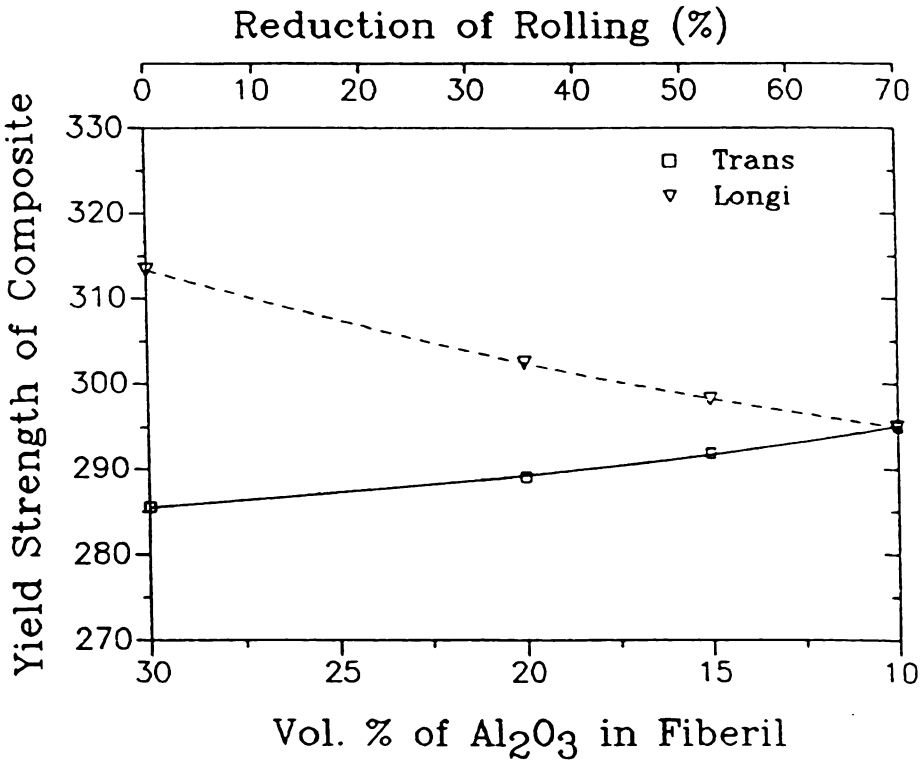

Fig.10 Predicted variation in the yield strength along the longitudinal and the transverse directions of the composite due to the redistribution of $(Al_2O_3)_p$ caused by rolling based on the proposed model. The solid and broken lines are the best fit curve for the calculated data points.

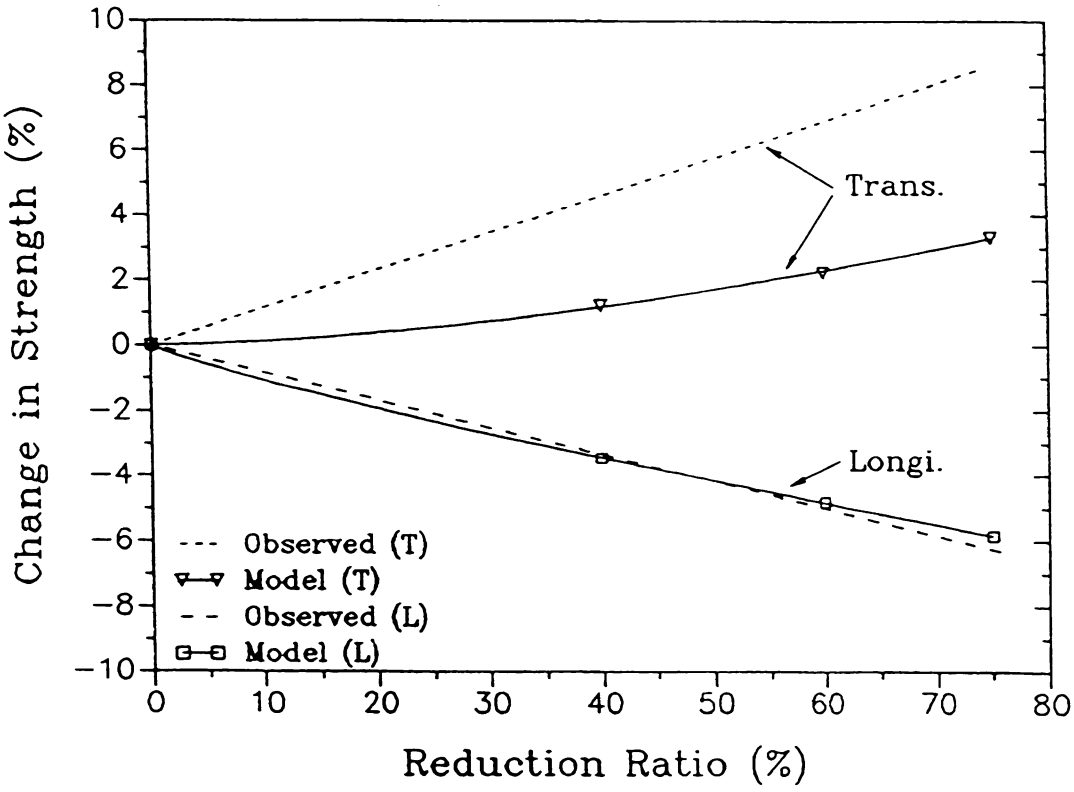

Fig.11 Plots comparing the predicted and observed percent changes in the yield strength as a function of reduction in rolling. Note that the observed and the predicted strength changes (%) are in good agreement along the longitudinal direction, whereas significant differences between the observed and the predicted strength changes exist along the transverse direction.

4.1.5 Effect of other parameters

Based on the analysis made so far, reasonable explanations could be given for the features of decreasing and increasing tensile behaviors of the longitudinal and the transverse specimen in proportion to increasing reduction ratio. This analysis, however, can not provide the reason why the strengths of rolled transverse composites with uniform distribution of $(Al_2O_3)_p$ become higher than those of the longitudinal ones, even under the unfavorable orientation (with respect to the tensile direction) of particulate cracking and interfacial debonding within the transverse composites. Other factors contributing to the discrepancy between the predicted and the observed strength along the transverse direction include

i) particulate damage (particulate cracking and interfacial debonding) due to cold rolling,

ii) decreased recrystallized grain size with increased reduction in rolling [13-15],

iii) disappearance of particulate free zones, and

iV) orientation of the individual particulates (with elliptical geometry) with respect to loading direction.

i) Effect of particulate damage

Particulate cracking and interfacial debonding caused by cold rolling can be considered as elliptical pore-like microcracks (as can be seen in Fig.4). Thus, the major axes of such microcracks are oriented parallel and perpendicular to the tensile direction in the longitudinal and transverse specimens, respectively. The states of stress at the tip of the elliptical microcrack are provided by Inglis

[16]; in two dimensional problem of elasticity in polar coordinates, the hoop stress ($\sigma_{\theta\theta}$) at the crack tip due to tension is

$$\sigma_{\theta\theta} = \sigma_{\circ} \left(1 + 2b/a \right) \qquad 2)$$

where $\sigma_{\circ}$ = applied stress

b = length of the crack perpendicular to the tension, and

a = length of the crack parallel to the tension.

It is worthy to note that the hoop stress at the tip of a microcrack in the transverse specimens is more severe than that in the longitudinal specimens, according to Eq 2). Therefore, upon loading, the microcracks in the transverse specimens will open up and propagate into the matrix more easily than those in the longitudinal ones; as a result, particulate crackings and interfacial debondings due to cold rolling would decrease the strength and ductility of the transverse specimens more than as it would do for longitudinal ones. So, it can not be used as a basis for explaining the higher observed strength, as compared to the predictions in that direction.

ii) Effect of decreased recrystallized grain size

During the course of this study, no significant change in the strength of the composite as a function of matrix grain size (in the range of interest) was observed. As a result, matrix grain size is not considered to be an important factor that contributes to the strength variation in the transverse direction.

iii) Effect of disappearance of particulate free zone

Redistribution of particulates by cold rolling separates the particulates in the banded region, allowing them to act as particulate strengtheners for the transverse direction. Fracture of as-received composite under transverse loading normally occurs by the crack propagation along the particulates within the banded region or along the particulate free zones. With the redistribution of particulates, the cracks are arrested during transverse loading, and higher strength results. However, such a redistribution will not have any significant effect on the longitudinal strength.

iV) Effect of the orientation of individual particulates with respect to loading direction

Individual particulates that can be assumed to be ellipsoids are oriented with their major axis parallel to the longitudinal direction in the as-received composite. Rolling along the transverse direction does not alter the orientation of the particulates. Such a feature has also been noted in whisker reinforced composites [8]. In order to simulate the situation of longitudinal and transverse specimen, one can consider a two dimensional composite model "A thin plate having an elliptical inclusion subjected to uniaxial tension" as shown in Fig.12. The states of stress at any points in such a composite system having an elliptical inclusion are given by Donnell [17]. Considering his solution, the radial stress (σ_α) at the pole of the inclusion becomes higher as the major axis of the elliptical inclusion is oriented to the axis of loading (i.e, the situstion in the

longitudinal composite). σ_α within the inclusion and at the interface near the pole of the inclusion is given as

$$\sigma_\alpha = \frac{3\zeta\ [\ 3(\zeta+r^2) + (1+5\zeta)r\ ]}{9\zeta\ (r^2+1) + 2\ (2-\zeta+8\zeta^2)r}\ \sigma_\circ \qquad 3)$$

where $\sigma_\circ$ = applied stress

r = b/a

ζ = E^i/E^m, and

E^i, E^m = elastic modulus of the inclusion and the matrix, respectively.

According to E3), stress concentration at the interface and within the inclusion will increase, as the values of 'r' and 'ζ' increase; i.e, for a given combination of the materials (i.e. constant ζ), the stress concentration factor, ($\sigma_\alpha/\sigma_\circ$), will increase, if the major axis of the inclusion is oriented in the direction of the tension.
A graphical illustration for the stress concentration at the pole of the inclusion with respect to the aspect ratio of $(Al_2O_3)_p$ [or the orientation of $(Al_2O_3)_p$] are shown in Fig.13. Under such conditions, the transverse loading causes less interfacial dedonding and particulate cracking due to less severe stress concentration at the particulate, as has been observed experimentally. As a result, the composite is able to withstand higher stresses in the transverse direction, than predicted by the model.

In addition, the simplified two dimensional model, which correctly predicts the strength along longitudinal direction, may be neglecting some of the three dimensional aspects that could mainly enhance the strength in the transverse direction.

The summary of the effects of these factors on the strength variation along the longitudinal and the transverse directions are presented in Table.2

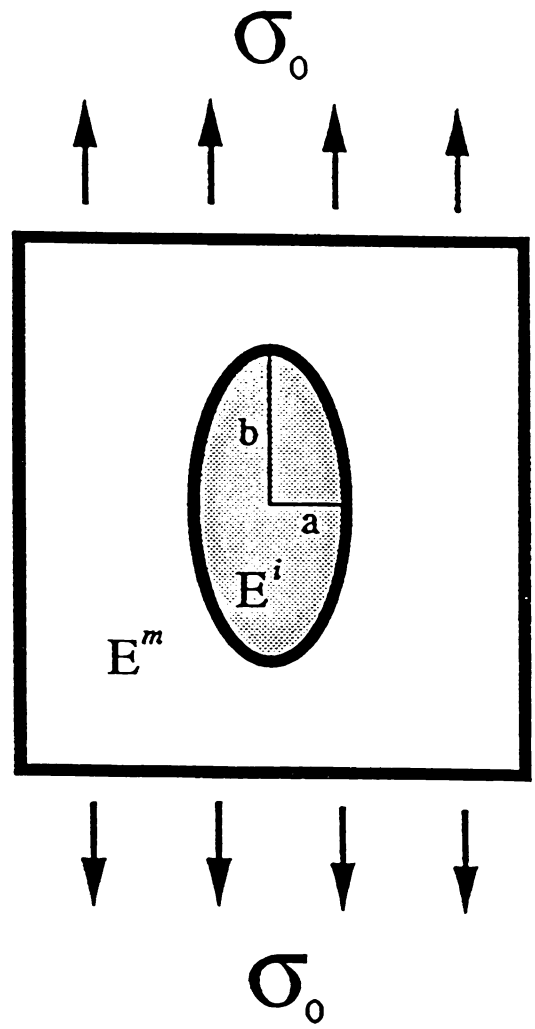

Fig.12 Schematic of two dimensional composite model: A thin plate (Al alloy) having an elliptical inclusion (Al_2O_3) subjected to uniaxial tension (σ_0). 'E^i' and 'E^m' denote the elastic modulus of the inclusion and the matrix, respectively.

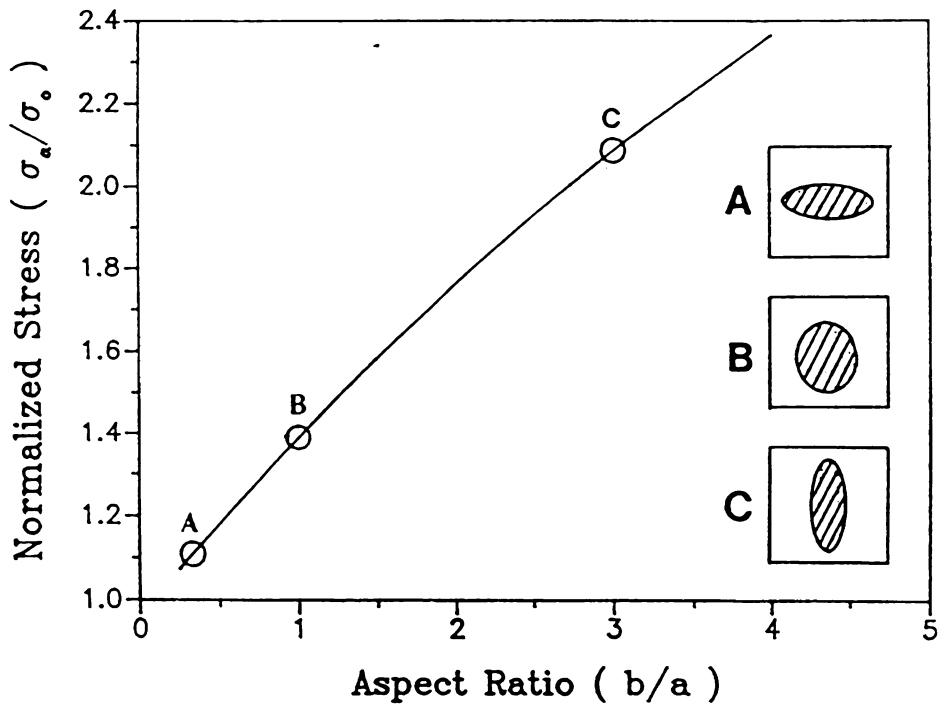

Fig.13 A plot showing theoretical stress concentration factor (σ_α/σ_0) at the pole of the inclusion as a function of the aspect ratio (b/a).

Table.2 Effect of the microscopic changes, due to increased amount of transverse cold rolling, on the tensile strength of the composite along the longitudinal and the transverse directions.

Parameter	Microscopic changes due to increased amount of rolling	Change in strength	
		Trans.	Longi.
Particulate damage	Increase in $(Al_2O_3)_p$ cracking & interfacial debonding		
Redistribution	More uniform distribution of $(Al_2O_3)_p$	{due to the spreading of $(Al_2O_3)_p$ considered in the two dimensional composite model}	
		{due to aspect ratio effect of $(Al_2O_3)_p$ with respect to the axis of loading}	
	Disappearance of $(Al_2O_3)_p$ free zone, leading to smaller grain size		
Resultant change in strength with increasing reduction in cold rolling			

Note: Arrows pointing upward(downward) represent contribution towards increase(decrease) in strength. The longer(shorter) arrows indicate significant(minimal) contribution.

4.2 Effect of redistribution of $(Al_2O_3)_p$ on the fracture strain

In spite of the particulate damage (where the microcrack is oriented perpendicular to the axis of loading in transverse specimen), the fracture strain along the transverse direction was observed to increase significantly (by a factor of 3 to 4) with increasing reduction in rolling. Such a behavior can also be attributed to the gradual redistribution of the particulates. The dispersion of the particulates obtained will minimize the stress concentration at the particulates, resulting in minimal particulate cracking and interfacial debonding upon loading, allowing larger plastic deformation of the matrix present between the particulates. At the same time, the uniform distribution of the particulates prevents the main crack from propagating directly through the $(Al_2O_3)_p$clusters or $(Al_2O_3)_p$ free zones.

On the other hand, the fracture strain along the longitudinal direction will be less affected by the uniform distribution of the particulates achieved by transverse rolling, since the fraction of the particulates across the width of the specimen remains the same before and after rolling. Thus, the crack propagating perpendicular to the direction of the banded clusters will have to confront the same number of particulates even after rolling with no observable change in the fracture strain.

5. CONCLUSIONS

5.1 Microstructural features

The composites could be cold rolled up to 75 % reduction without forming any edge crack or surface scuffing. Significant redistribution of $(Al_2O_3)_p$ clusters was achieved with increasing reduction ratio. The banded structure of $(Al_2O_3)_p$ clusters in the as-received extruded composites totally disappeared beyond 60-70 % of reduction. Substantial amounts of particulate cracking and interfacial debonding were formed due to cold rolling.

5.2 Tensile properties

The principal effects of an increasing amount of cold rolling along the transverse direction on the tensile properties are to increase the strength and fracture strain along the transverse direction and to decrease these properties along the longitudinal direction. Such behaviors are mainly due to the redistribution of $(Al_2O_3)_p$. The proposed two dimensional model is able to explain the observed trends qualitatively.

6. REFERENCES

1. V.Laurent, D.Chatain, and N.Eustathopoulous, "Wettability of SiC by aluminum and Al-Si alloys" J. Mater. Sci., 22, 244-250, (1987).

2. C.G.Levi, G.J.Abbaschian, and R.Mehrabian, "Interface interaction during fabrication of aluminum alloy-alumina composites", Metall. Trans. A, 9, 697-711, (1978).

3. D.Webster, "Effect of Lithium on the mechanical properties and microstructure of SiC whisker reinfroced aluminum alloys", Metall. Trans. A, 13, 1511-1519, (1982).

4. J.C.Lee and K.N.Subramanian, "Effect of cold rolling on the elastic properties of $(Al_2O_3)_p$/Al composites." J. Mat. Sci., (in press)

5 J.C.Lee and K.N.Subramanian, "Rolling of SiC_p reinforced aluminum alloy composites", Proceeding of the Sixth Annual ASM/EDS Advanced Composites Conference, Detroit, Michigan, Oct. p575-583, 1990, published by ASM International, Materials Park, Ohio, (1990).

6. M.G.McKimpson and T.E.Scott, "Processing and properties of metal matrix composites containing discontinuous reinforcement", Mat. Sci. Eng. A, 107, 93-106, (1989).

7. A.P.Divecha, S.G.Fishman, and S.D.Karmarkar, "Silicon Carbide reinforced Aluminum - A formable composites" J. Metals, 33, 12-17, (9.1981).

8. D.L.McDanels, "Analysis of stress-strain, fractiure, and ductility behavior of aluminum matrix composites containing discontinuous silicon carbide reinforcement", Metall. Trans. A, 16, 1105-1115, (1985).

9. R.D.Schueller and F.E.Wawner, "Effect of hot rolling on AA2124 15 % SiC whisker composites", J. Comp. Mat., 24, 1060-1076, (1990).

10. S.V.Nair, J.K.Tien, and R.C.Bates, "SiC reinforced aluminum metal composites", Int. Metall. Rev., 30, No.6, 275-290, (1985).

11. W.H.Sutton and J.Chorne, "Potential of Oxide-Fiber Reinforced Metals", Fiber Composite Materials, ASM. p177-184, (1964).

12. G.S.Holister and C.Thomas, Fiber Reinforced Materials, Elsevier Co. p77-82, (1966).

13. W.A.Anderson and R.F.Mehl, "Recrystallization of Aluminum in terms of the rate of Nucleation and the rate of Growth", AIME. Trans., 161, 140-172, (1945).

14. S.L.Channon and H.L.Walker, "Recrystallization and grain growth in alpha brass", ASM. Trans., 45, 200-220, (1953).

15. F.N.Rhines and B.R.Patterson, "Effect of the degree of prior work on the grain volume distribution and the rate of grain growth of recrystallized aluminum", Metall. Trans. A, 13, 985-993, (1982).

16. S.P.Timoshenko and J.N.Goodier, Theory of Elasticity, Third edition, p187-194, McGraw-Hill Co.

17. L.H.Donnell, Theodore von Karman Anniversary Volume, California Institute of Technology, Pasadena, (1941) p293.

CHAPTER VI

YOUNG'S MODULUS OF COLD AND HOT ROLLED $(Al_2O_3)_p$/Al COMPOSITES

This chapter is based on the paper that has been submitted to Journal of Materials Science. The following is the abstract of the original paper.

The Young's modulus of the hot rolled Al alloy reinforced with Al_2O_3 particulates [$(Al_2O_3)_p$/Al composite] is measured using the dynamic sonic resonance test method. The variation in the moduli of the cold and the hot rolled composites, as a function of the reduction ratio, is compared. Although both cold and hot rolling result in more uniform distribution of the particulates, hot rolling causes less damage to the reinforcements, resulting in more isotropic composites possessing higher Young's modulus. These observed variations in the Young's modulus with respect to reduction ratio are analyzed on the basis of the microstructural changes due to the rolling and T6-heat treating operations.

Note: Detailed study on the effect of annealing texture on the Young's modulus of the composite is provided in APPENDIX IV.

1. INTRODUCTION

Metal matrix composites reinforced with low cost ceramic particles, with attractive mechanical properties suitable for commercial applications that do not require very high unidirectional strengthening, are being investigated. One of the characteristics of such composites is that they can be mechanically worked during the final shaping process. The forces associated with mechanical working not only cause the redistribution of the reinforcements, but also cause microscopic damage, such as particulate cracking and interfacial debonding [1,2], affecting the material properties of the resultant composite. Changes in the material properties, especially the elastic properties, due to the mechanical shaping process are one of the important considerations that have to be taken into account in engineering design. The variation in the Young's modulus of the cold rolled $(Al_2O_3)_p$/Al composite has already been reported in the literature [2]. The results indicated that the Young's modulus along the longitudinal direction increases with increasing reduction ratio. This property along the transverse direction, however, decreases with increasing amounts of cold rolling. Such behaviors could be explained on the basis of the observed microstructural changes caused by the cold rolling operation, i.e, redistribution of $(Al_2O_3)_p$ and damage of $(Al_2O_3)_p$. In case of the transverse specimen, the contribution of the microcracks to the Young's modulus is more predominant than that due to the redistribution of $(Al_2O_3)_p$ and the texture formation. As a result, the transverse Young's modulus of cold rolled composite is lower than that of the as-extruded, and the longitudinal specimens.

Such experimental results indicated that if the damage on $(Al_2O_3)_p$ could be eliminated efficiently during rolling, the rolling operation can result in an increase in the Young's modulus of the composite. In order to minimize the damage of $(Al_2O_3)_p$, hot rolling was carried in this study.

The objectives of the present study are to investigate the effects of cold and hot rolling on the redistribution of $(Al_2O_3)_p$ clusters and microcracks in $(Al_2O_3)_p$, and to evaluate their influences on the Young's modulus of the composite.

2. EXPERIMENTAL PROCEDURE

2.1 Specimen Preparation

Duralcan composite (W6A 10A), 6061 aluminum alloy reinforced with 10 % of $(Al_2O_3)_p$, obtained in the form of extruded cylindrical bars with an extrusion ratio of 20:1, was used in this study. Unidirectional hot rolling with a reduction ratio of about 10 % per pass was carried out in a direction perpendicular to the extruded direction. The temperature of the specimen measured before the entrance of the rolls was about 500°C. The rolled composite was reheated at 540°C for 3 min. between passes so as to maintain consistent hot rolling conditions. Thin slices with directions parallel (longitudinal) and perpendicular (transverse) to the extruded direction were cut from the rolled sheets having various percentages of reduction. Similar procedures were also employed in cold rolling without the heating of the specimens. The details regarding the

procedures used in cold rolling, specimen preparation, and T6 heat treatment utilized are described elsewhere [2]. The grain size of the rolled specimens were measured using the line intercept method.

2.2 Modulus Measurement

All Young's modulus measurements were carried out at room temperature in air using the standard sonic resonance test method designated by ASTM C848-78. The equation used for the calculations of the Young's modulus is that derived for the prismatic bars with a rectangular cross-section under free-free suspension [3]:

$$E = 0.94642\ (\ell^4/t^2)(\rho f^2)\ T \qquad (1)$$

where E is the Young's modulus, ℓ is the length of the specimen, 't' is the thickness of the specimen, ρ is the density of the specimen, 'f' is the fundamental flexural resonance frequency, and 'T' is the shape factor which depends on the geometry of the specimen. The approximate shape factor (T) used for the calculation is that obtained by Spinner [4]

3. RESULTS

3.1 Effect of Rolling on the Microstructural changes

3.1.1 Grain size

The recrystallized grain size of the cold rolled composites were found to decrease with increasing amounts of prior cold rolling, which is consistent with previous findings [5]. As reported in the literature [5], this is due to the fact that the ratio of nucleation rate to growth rate ($\partial N/\partial G$) at recrystallization temperature increases with increasing amounts of prior cold working. However, the grain size of the hot rolled composites were observed to increase with increasing reduction. This could probably be explained on the basis that 10 % reduction per pass used in the present study was not sufficient to promote recrystallization. Under such conditions, gradual extension of the grain boundary with the help of the applied mechanical energy can occur [6]. These observations are presented in Fig.1.

3.1.2 Redistribution of particulates

The most apparent difference in metallographic features between the as-extruded and the rolled composites is that $(Al_2O_3)_p$, initially present in the form of banded clusters along the extrusion direction, becomes more uniformly distributed with increasing reduction ratio. The microstructural changes due to the redistribution of $(Al_2O_3)_p$ achieved by hot rolling are presented in Fig.2. Similar redistribution could also be obtained using cold rolling [2].

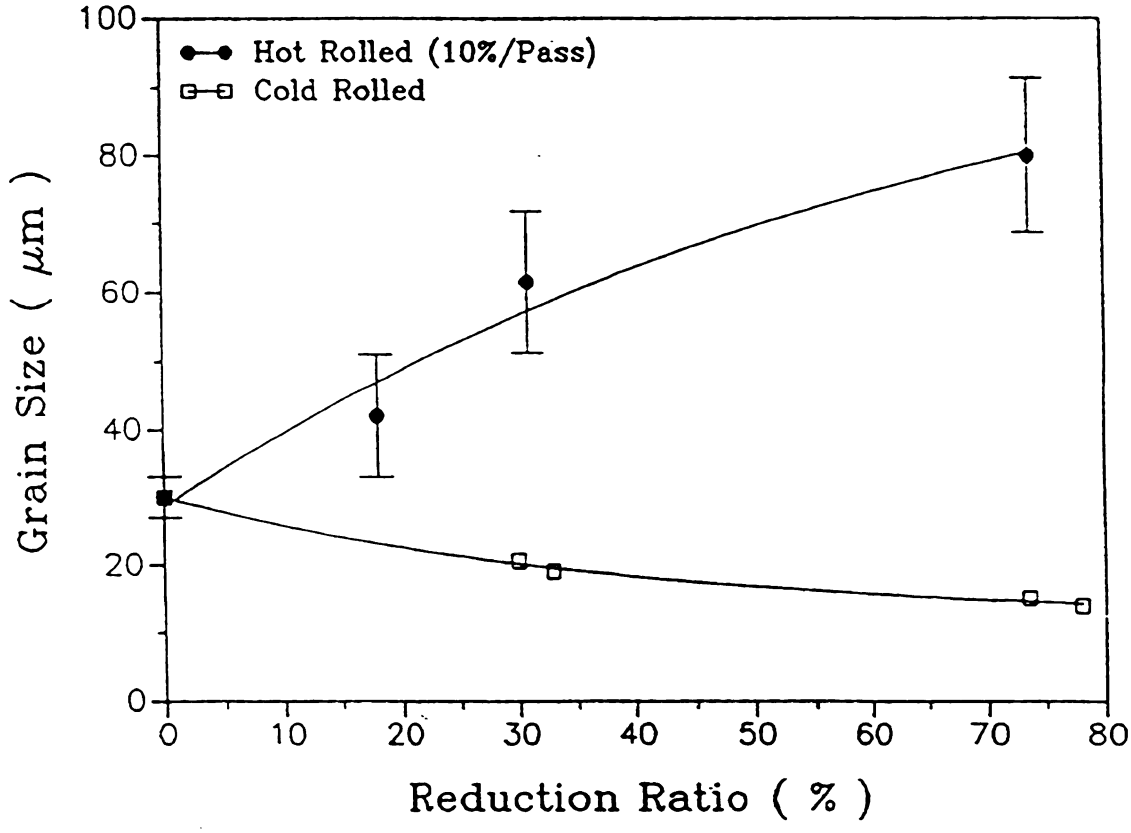

Fig.1 Variation of the grain size of the cold and hot rolled composites as a function of the reduction ratio. The error bars indicate one standard deviation.

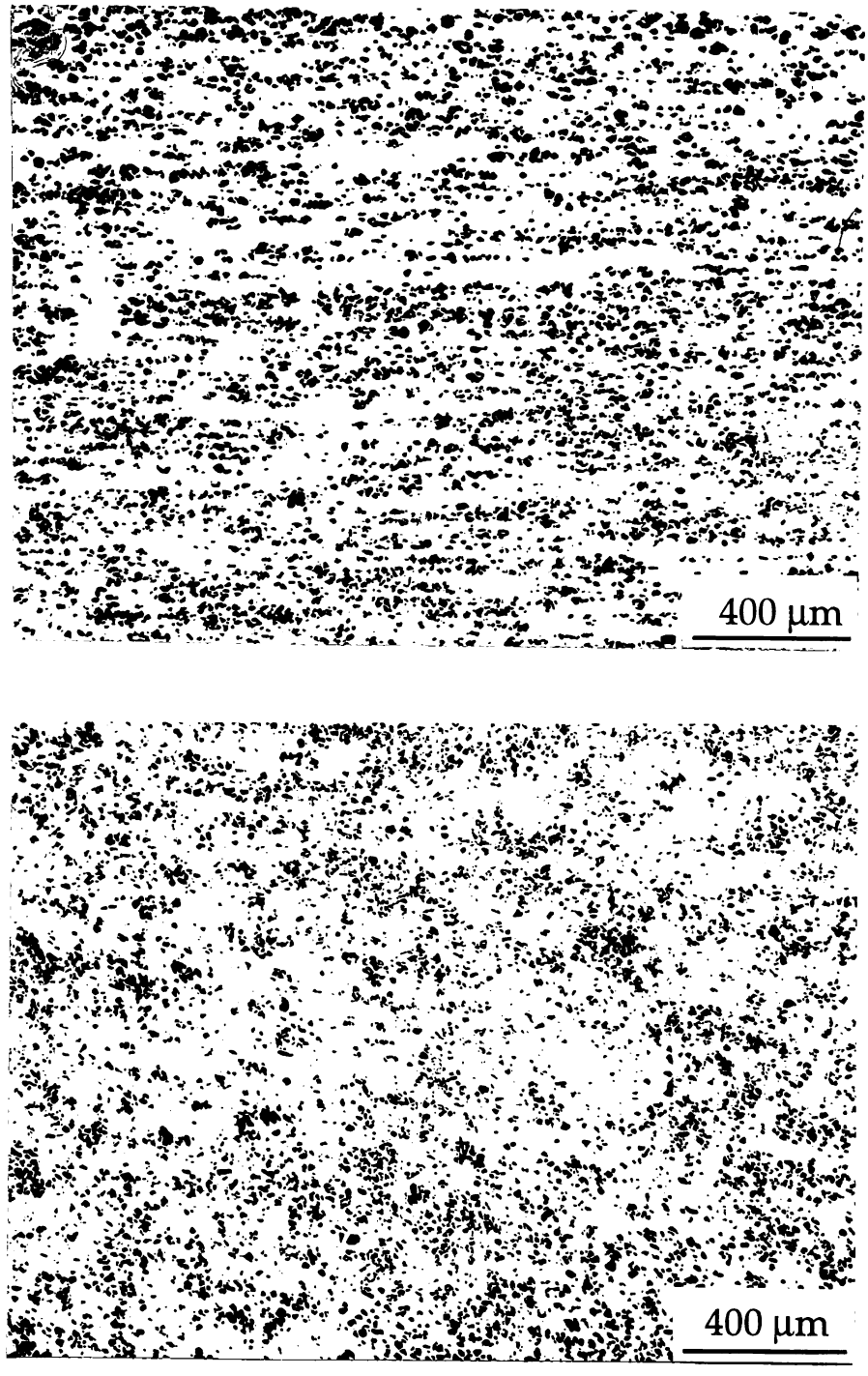

Fig.2 Optical micrographs showing the distribution of $(Al_2O_3)_p$ in
a) the as-extruded composite and
b) the 70% hot rolled composite.

3.1.3 Particulate damage

Although uniform distribution of $(Al_2O_3)_p$ could be achieved by the rolling operation, the microscopic observations of the cold rolled composites showed significant damage to the reinforcements, i.e, particulate cracking and interfacial debonding (Fig.3(a)). However, hot rolling results in significantly less damage on the reinforcements as shown in Fig.3(b). In addition, there was strong tendency for these crack planes to be parallel to the direction of compression (i.e rolling pressure) and be perpendicular to the rolling direction, as shown in Fig.3(c). The grid analysis performed on the micrographs taken from the rolled composites showed that the extent of damaged reinforcements increases linearly with increasing reduction ratio. The results of these studies are presented in Fig.4.

3.2 Effect of rolling and T6-heat treating operation on the Young's Modulus

Effects of cold rolling on the Young's modulus of this composite has already been reported [2]. This study showed that the longitudinal Young's modulus increases substantially in the early stages of cold rolling and decreases slightly afterwards; On the other hand, the transverse Young's modulus increases slightly in the early stages of rolling and decreases substantially afterwards (Fig.5). The deviation between the longitudinal and the transverse moduli of the cold rolled composites increases as the reduction ratio increases. In case of the hot rolled composites, a similar trend has been observed in the variation of the Young's modulus along the longitudinal direction. However, the transverse moduli of the hot

rolled composite, unlike in the case of the cold rolled ones, increases substantially, and approaches the longitudinal values. These features are presented in Fig.5.

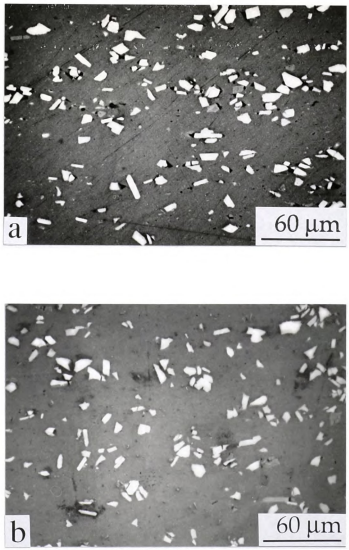

Fig.3 Scanning electron micrographs showing the particulate damage in a) 70 % cold rolled composite, b) 70 % hot rolled composite.

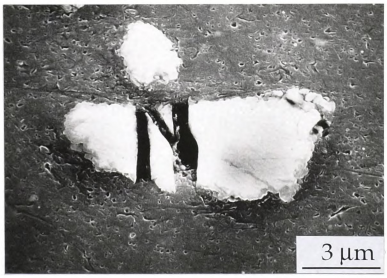

Fig.3 (continued)

c) magnified view of the cracked particle in which the crack planes are perpendicular to the direction of rolling indicated by an arrow.

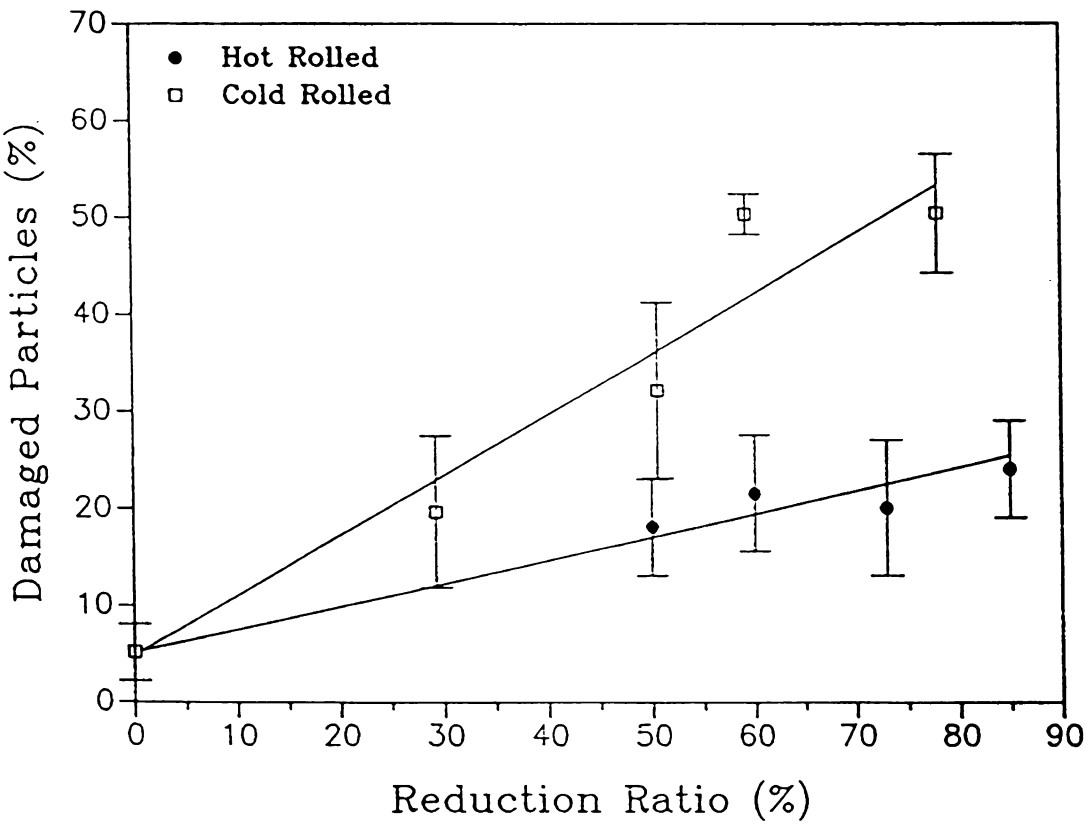

Fig.4 Plots of the percentage of the damaged particulates as a function of the reduction ratio. The error bars indicate one standard deviation.

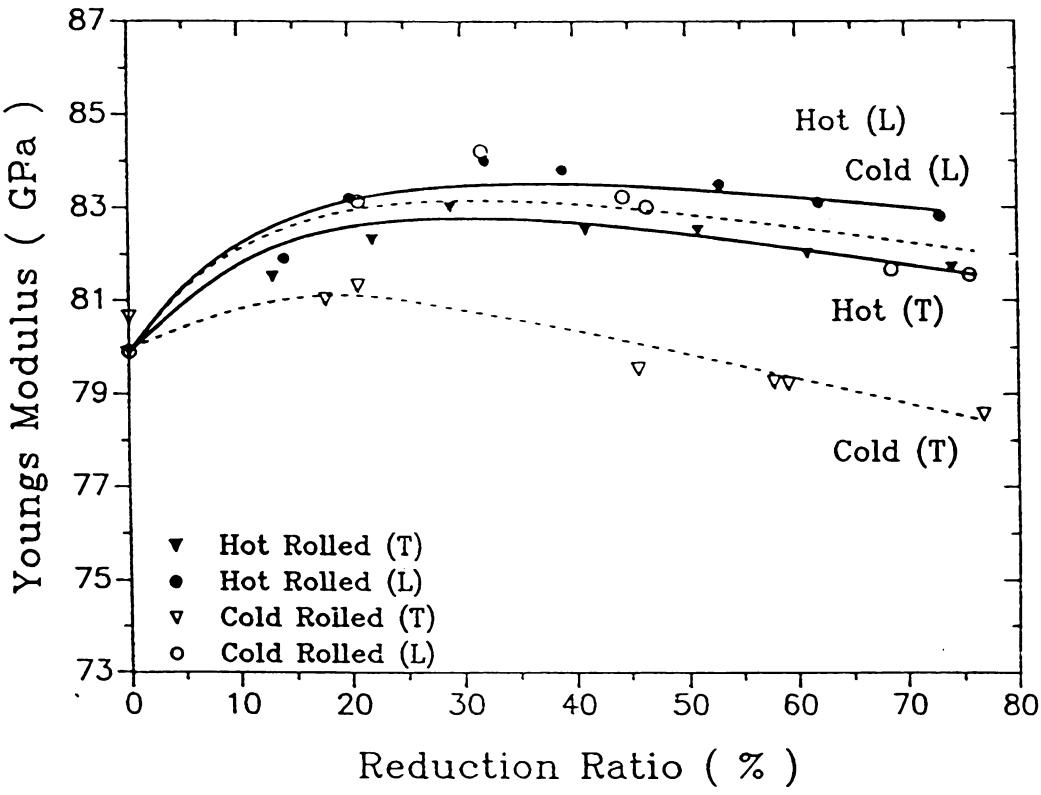

Fig.5 Plots of the experimentally measured Young's modulus of the cold and the hot rolled composites along the longitudinal(L) and the transverse(T) directions.

4. DISCUSSION

Although the Young's modulus has been known as one of the microstructure insensitive material properties, variation (usually less than 30%) in the modulus of a polycrystalline material can occur due to the changes in the microstructures. For a given material, such a variation in the modulus due to the microstructural changes can be related with the changes in the resonance frequency of the material (or propagating speed of resonant waves), as suggested by Eq(1). As a result, the presence of the microstructural defects such as pores, microcracks, grain boundaries, dislocations, etc. lowers the Young's modulus, since they impede the travelling sonic waves, resulting in lower resonant frequency. The effects of such microstructural changes on the variations of the Young's modulus (due to the rolling and T6-heat treating operations) are discussed in this section.

4.1 Effect of grain size and microcracks on the Young's modulus

Sugihara [7] and Koster [8] have reported that the Young's modulus of the aluminum alloy is relatively unaffected (or increases slightly if any) with increasing grain size. Since the average grain size observed in this investigation is within the range considered in their studies, grain size is not believed to be an important contributor to the observed variations in the Young's modulus.

The effect of microcracks on the Young's modulus has already been reported in literatures [9,10]. They indicate that the modulus of a material decreases linearly due to the presence of the microcracks when the crack planes of such microcracks within the material are

oriented perpendicular to the tensile direction (or the direction of the travelling sonic waves). However, the effect of the microcracks on the Young's modulus will be less significant, when the crack planes are oriented parallel to the tensile direction. As a result, the effect of microcracks on the transverse and the longitudinal modulus can be expressed as [2]

$$E_t = E_o [1 - \gamma X] \quad (2)$$

$$E_\ell \approx E_o \quad (3)$$

where E_t and E_ℓ are the Young's moduli of the rolled and T6-treated composites along the transverse and the longitudinal directions respectively, E_o is the Young's modulus of the as-extruded composite, 'X' is the reduction ratio which has a linear relationship with microcrack density, and γ is a constant.

4.2 Effect of particulate redistribution and texture on the Young's modulus

Since the formation of the microcracks due to the rolling operations should result in decrease in the modulus, it cannot explain the observed increase in the modulus of the longitudinal specimens. However, two microstructural changes due to rolling, i.e the redistribution of the reinforcements and the texture formation, can provide the basis for the measured increment in the modulus of such specimens.

Theoretical treatments dealing with the Young's modulus of the metal matrix composites reinforced with ceramic particulates have considered the role of the volume fraction of the reinforcements [11,12]. The effects due to the size and the shape of the particulate reinforcements are not taken into account in these treatments. However, the experimental studies have shown that for a given volume fraction of the reinforcements, the modulus increases as the particulate size decreases [13,14]. Such experimental observations are explained on the basis of more efficient load transfer achieved by increased interface area in composites with particulates [15]. With this point of view, the separation of particulates present in clusters and their redistribution due to the rolling operation, can contribute to an increase in the modulus both along the longitudinal and the transverse directions. Annealing texture in a cold rolled and T6-treated material can also contribute to an increase in the Young's modulus along both directions (due to the preferred crystallographic orientations with respect to the tensile direction) [13]. However, the observed differences in the modulus along different directions as a function of reduction ratio in cold and hot rolled (T6 treated) composites, given in Fig.5, cannot be explained on the basis of texture, since all the specimens used in this study will have comparable texture contributions.

Based on the experimental observations, changes in the Young's modulus due to the microstructural changes can be approximated by the curve fitting method;

$$E = E_o (1 + \alpha e^{\beta X}) \quad (4)$$

where α and β are constants that can be determined from the y-intercept and the slope of $\ell n(E-E_o)$ versus reduction ratio plot.

4.3 Combined effects of the various parameters on the modulus

The analytical expression of the form

$$E = E_o (1 + \alpha X^{\beta})(1 - \gamma X) \quad (5)$$

has been used to account for various contributions to the Young's modulus in an earlier study [2]. However, an expression of the form

$$E = E_o (1 + \alpha e^{\beta X} - \gamma X). \quad (6)$$

has been found to provide better fit with experimental measurements than the above expression. In this equation, $(\alpha E_o e^{\beta X})$ is due to the texture formation and the redistribution of $(Al_2O_3)_p$, and $(-\gamma E_o X)$ corresponds to the effect due to the presence of the microcracks. The effects of these two oppositely contributing factors are schematically illustrated in Fig.6.

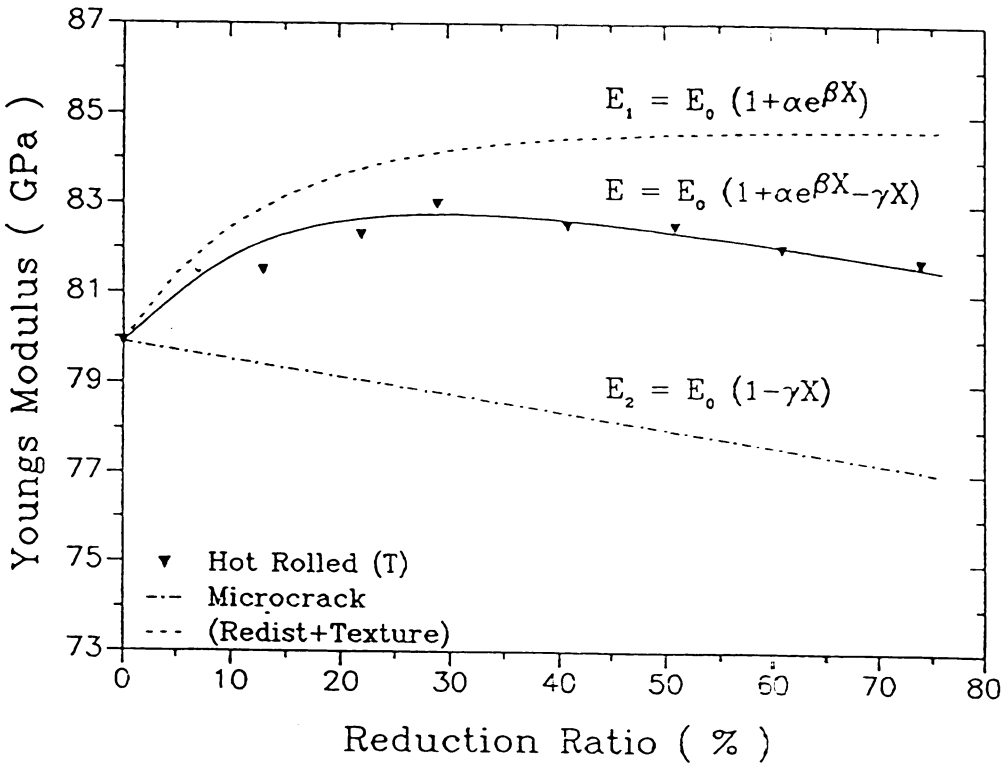

Fig.6 A schematic illustrating the effect of the redistribution of $(Al_2O_3)_p$, the texture formation and the microcracks on the resultant Young's modulus of the hot rolled transverse composites. In the graph, E_1 is the Young's modulus due to the redistribution of $(Al_2O_3)_p$ and the texture formation, and E_2 is due to the formation of microcracks. E is the Young's modulus due to the combined effects of E_1 and E_2.

5. SUMMARY

Following statements summarize the results of cold and hot rolling carried out on extruded $(Al_2O_3)_p$/Al composites.

5.1 Effect of rolling on the microstructural features

$(Al_2O_3)_p$ clusters, initially present in the form of banded clusters along the extrusion direction in the as-extruded composite, become more uniformly distributed with increased reduction in cold and hot rolling. However, this uniform distribution of $(Al_2O_3)_p$ due to rolling is always associated with particulate cracking and interfacial debonding. Such a crack damage, formed during rolling, was more significant in case of cold rolling than in hot rolling. The extent of damage in $(Al_2O_3)_p$ increases linearly with increasing reduction ratio in both cases. In addition, there is strong tendency for the crack planes to be formed perpendicular to the rolling direction.

5.2 Effect of rolling on the Young's modulus

The Young's moduli of the hot rolled composites were found to be generally higher than those of the as-extruded, and the cold rolled composites. The variation of the Young's modulus as a function of the reduction ratio have the form of $E = E_o (1 + \alpha e^{\beta X} - \gamma X)$. Such a variation in the Young's modulus of the composites is believed to be due to the combined effects of the redistribution of $(Al_2O_3)_p$, the texture formation, and the microcracks. The analytical expressions which account for their contributions to the Young's modulus were obtained by using curve fitting method; The effect of microcrack on

the Young's modulus was found to be in the form of $E = E_o (1 - \gamma X)$, indicating that the modulus decreases linearly with increasing reduction ratio. However, the effect of the redistribution of $(Al_2O_3)_p$ and texture formation on the Young's modulus has the form of $E = E_o (1 + \alpha e^{\beta X})$, indicating that the modulus increases with increasing reduction ratio. Hot rolling minimizes the extent of damage on the reinforcements, resulting in significant increase in the transverse modulus that approaches the longitudinal values.

6. REFERENCES

1. J.C.Lee and K.N.Subramanian, "The effect of cold rolling on the tensile properties of $(Al_2O_3)_p$/Al composite", Mat. Sci. Eng. (in press).

2. J.C.Lee and K.N.Subramanian, "The effect of cold rolling on the elastic properties of $(Al_2O_3)_p$/Al composite", J. Mat. Sci. (in press).

3. G.Pickett, Am. Soc. "Equations for computing elastic constants from flexural and torsional resonant frequencies of vibration of prisms and cylinders" Testing Mats. Proc., 45, 846-865, (1945).

4. S.Spiner, T.W.Reichard, and W.E.Tefft, J. of Research, National Bureau of Standards, 16A, (1960) 147.

5. W.A.Anderson and R.F.Mehl, "Recrystallization of Aluminum in terms of the rate of nucleation and the rate of growth" AIME Trans., 161, 141-172, (1945).

6. J.D.Verhoeven, Fundamentals of Physical Metallurgy, John Wiley & Sons, New York, (1975) p352.

7. M.Sugihara, "Elastic properties of an Aluminum rod composed of large crystal grains" Mem. Coll. Sci. Kyoto Imp. Univ. A17, 389-397, (1934)

8. V.W.Koster, "Elastic modulus and damoing of Aluminum and Aluminum alloys" Ztsch. Metallkunde, 32, 282-287, (1940).

9. B.Budiansky and R.J.O'connell, Int. J. Solids, 12, (1976) 81.

10. D.P.F.Hasselman and J.P.Singh, "Analysis of thermal stress resistance of microcracked brittle ceramics" Am. Cer. Soc. Bulletin, 856-860, (1979).

11. S.Ahmed and F.R.Jones, J. Mat. sci. 25, (1990) 4933.

12. F.A.Girot, J.M.Quenisset, and R.Naslain, "Discontinuously reinforced Aluminum matrix composites" Comp. Sci. Tech, 30, 155-184, (1987).

13. T.B.Lewis and L.E.Nielsen, "Dynamic mechanical properties of particulate filled composites" J. App. Polym. Sci, 14, 1449-1471, (1970).

14. J.Spanoudakis and R.J.Young, "Crack propagation in a glass particle filled epoxy resin" J. Mat. Sci, 19, (1984) 473.

15. D.J.Mack, Trans. "Young's modulus - its metallurgical aspect" AIME, 166, 68-85, (1946).

CHAPTER VII.

THE TENSILE PROPERTIES OF COLD AND HOT ROLLED $(Al_2O_3)_p$/Al COMPOSITES

This chapter is based on the paper submitted to Material Science and Engineering. The following is the abstract of the original paper.

Hot rolling was carried out on the extruded 6061 Al alloy composite reinforced with Al_2O_3 particulates [$(Al_2O_3)_p$/Al composite] along a direction perpendicular to the extrusion direction of the composite. Room temperature tensile tests of the hot rolled composites showed significant increase in strength and fracture strain along the transverse (rolling) direction with increasing reduction in rolling However, the same properties along the longitudinal (extrusion) direction were relatively unaffected by hot rolling. Such behaviors of rolled composites are compared with those of the cold rolled composites and analyzed on the basis of the microstructural changes such as redistribution of the particulate clusters, disappearance of the particulate free zones, particulate damage, and smaller matrix grain size of the rolled composites.

1. INTRODUCTION

Although considerable increase in strength and Young's modulus could be achieved by adding ceramic particulates into molten metallic alloy, these improvements are associated with substantial decrease in ductility. One of the features responsible for this low ductility is the non-uniform distribution (and clustering) of the reinforcements, which can be altered by mechanical working of the composites.

The variations in the tensile properties of the cold rolled $(Al_2O_3)_p$/Al composites has already been reported in the literature [1]. Increasing reduction in cold rolling results in significant decrease in strength and insignificant change in fracture strain along the longitudinal direction. However, along the transverse direction, substantial increases in these properties were observed. These behaviors were explained on the basis of the observed microstructural changes caused by the cold rolling and T6 heat treating operations, especially the redistribution and the damage of $(Al_2O_3)_p$. If the substantial damage to $(Al_2O_3)_p$ observed in the cold rolled composites could be eliminated effectively, additional increase in the strength and the fracture strain could be achieved by the rolling operation. In order to minimize such a damage to the particulates, hot rolling was carried out in this study. The effects of hot rolling on the microstructural changes of $(Al_2O_3)_p$/Al composite and its influence on the tensile properties were investigated. These findings are compared with results obtained by cold rolling of the same composite. The observed variations in the composite properties are analyzed using a simplified three dimensional composite model.

2. EXPERIMENTAL PROCEDURE

Duralcan composite (W6A 10A) with 6061 aluminum alloy reinforced with 10 % of $(Al_2O_3)_p$, obtained as extruded cylindrical bars, was used in this study. The shape of $(Al_2O_3)_p$ present in the as-received composite is blocky type platelet with an average major dimension of 10 μm and an aspect ratio of about 2. Micrographs showing the detailed morphology of $(Al_2O_3)_p$ can be found elsewhere [1,2]. Unidirectional hot rolling using a laboratory mill with 10cm diameter roll at a roll speed of 8m/min was carried out in a direction perpendicular to the extruded direction with 35-45% reduction in thickness per pass. The temperature of the specimen at the entrance of the rolls was about 530°C. The rolled composite was reheated at 590°C for 2-3 min between passes. Thin slices with directions parallel (longitudinal) and perpendicular (transverse) to the extruded direction were cut from the rolled sheets having various percentages of reduction. Similar procedures were also employed in cold rolling without the heating of the specimens and the intermittent stress relief annealing. The details regarding the procedures used in cold rolling, specimen preparation, and T6 heat treatment utilized in this study are described elsewhere [1]. The grain size of the rolled specimens were measured using the Jeffries method. Room temperature tensile tests were carried out using a constant cross-head speed of 0.1cm/min.

3. RESULTS

3.1 Effect of hot rolling on the microstructural features

3.1.1. Redistribution of the particulates

The most apparent difference in metallographic features between the as-extruded (as-received) and the hot rolled composites is that $(Al_2O_3)_p$, present as banded clusters in the as-extruded composite, becomes more uniformly distributed with increasing reduction ratio. In addition, $(Al_2O_3)_p$ free zones with a width ranging from 50 to 200 μm along the transverse direction present in the as-extruded composite become narrower. Most of these zones, except when they are significantly wide, disappeared at about 70% reduction in rolling. In spite of these significant changes in the distribution of $(Al_2O_3)_p$ clusters, the orientation of each $(Al_2O_3)_p$ (initially aligned with their major axes parallel to the extrusion direction) was not altered substantially even after the hot rolling operation. Detailed micrographs showing such a redistribution of the particulate reinforcements due to hot rolling are given elsewhere [3]. Similar behaviors in the particulate redistribution were observed in the cold rolled composites [1,4].

3.1.2. Matrix grain size

The average matrix grain size of the as-extruded composite was measured to be about 30μm (Fig.1(a)). The grain sizes in the range of 70-100μm were occasionally observed within $(Al_2O_3)_p$ free zones [1]. The recrystallized grain size of the hot rolled composites with 35-45% reduction per pass becomes smaller as with increasing reduction in hot

rolling, resulting in an average grain size of 15μm after 75% reduction (Fig.1(b)). This is due to the fact that the ratio of the nucleation rate and the growth rate ($\partial N/\partial G$) at the recrystallization temperature increases as the prior amount of reduction in rolling increases [5]. Similar behavior was also observed in the cold rolled specimens (Fig.1(c)). Graphical illustration of such observations is present in Fig.2. However, hot rolling with 10% reduction per pass was found to result in significantly larger grains with increasing reduction, providing 80-100μm grains after 75% reduction (Fig.1(d)). This can be explained on the basis that 10 % reduction per pass was not sufficient to promote the recrystallization of the matrix alloy of the composite. Under such conditions, gradual extension of the grain boundary with the help of the applied mechanical energy may occur [6]. This resulted in considerable decrease in the composite strength. As a result, the study was conducted with 35-45% reduction per pass, and the term 'hot rolling' refers to this condition for the rest of this paper.

3.1.3. Damage to the particulates

The uniform distribution of $(Al_2O_3)_p$ observable in the hot rolled composites is accompanied by particulate cracking and interfacial debonding. The extent of such damage to the particulates, however, was found to be less significant as compared to that in the cold rolled composites. The extent of particulate damage, either in the form of particulate cracking or interfacial debonding, appears to increase linearly with increasing reduction ratio in hot rolling probably due to substantial increases in rolling pressure (Fig.3).

These particulate crackings and interfacial debondings formed during rolling, did not appear to heal even after the solution treatment. In addition, there was a strong tendency for the crack planes in the particulates to be formed perpendicular to the rolling direction and parallel to the rolling pressure.

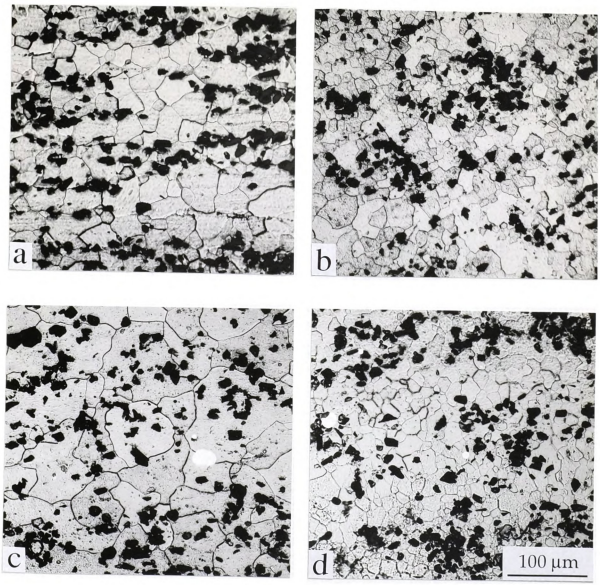

Fig.1 Optical micrographs showing the matrix grain size in
a) as-received composite, b) 70% cold rolled composite,
c) 70% hot rolled composite (10% reduction/pass), and
d) 70% hot rolled composite (35-45% reduction/pass).
All the micrographs are taken at the same magnification.

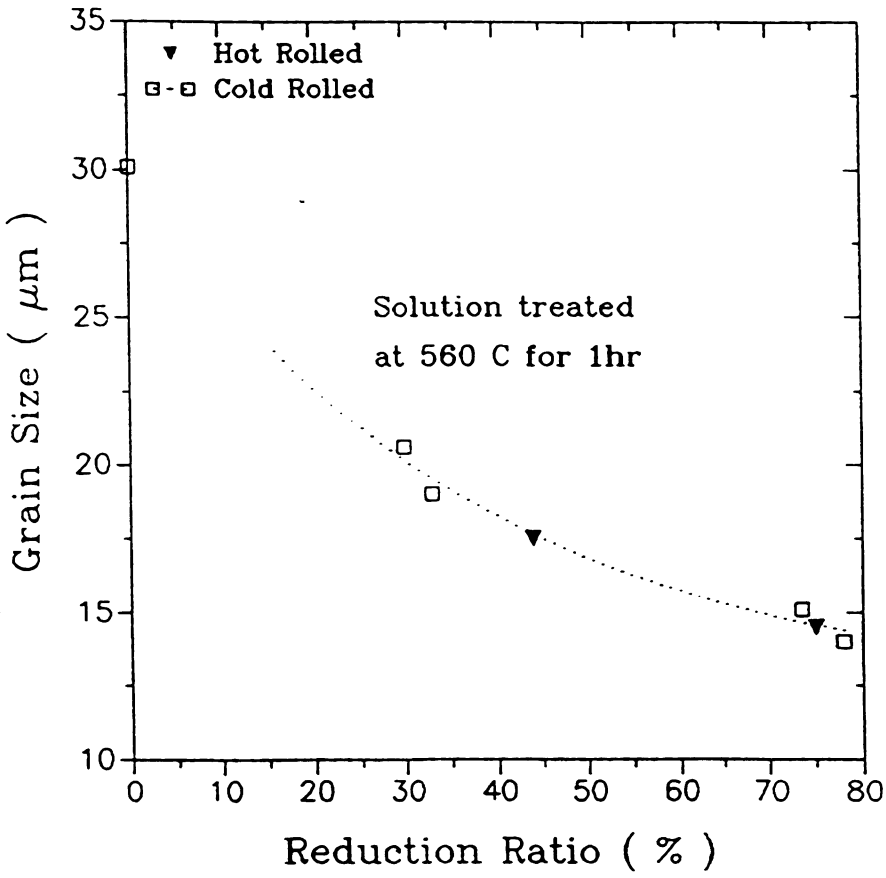

Fig.2 A plot illustrating the variation in the recrystallized grain size of the cold and the hot rolled composites as a function of the prior amount of rolling.

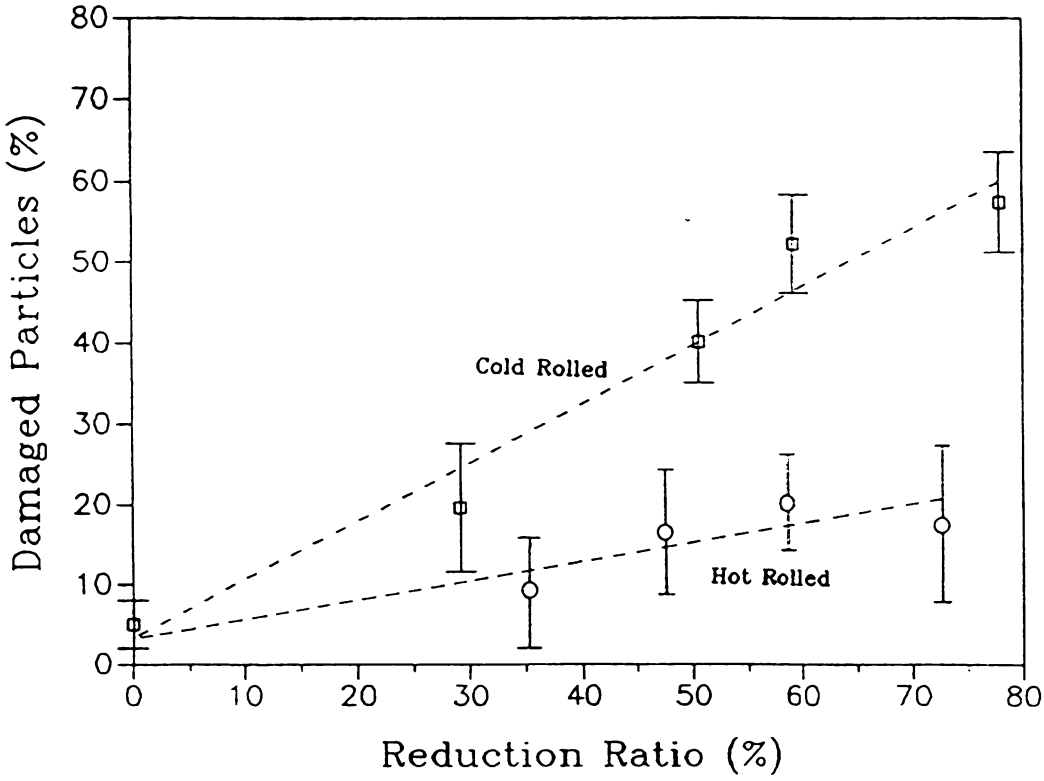

Fig.3 A plot showing the fraction of the damaged particulates versus reduction ratio.

3.2 Effect of hot rolling on the tensile properties

The strength and the fracture strain of the **as-extruded** $(Al_2O_3)_p/Al$ composites along the longitudinal and the transverse directions were found to be anisotropic. Such an anisotropy has already been explained on the basis of the microstructural inhomogeneities within the as-extruded composite, such as banded clusters of particulates, particulate free zones, large matrix grains within the particulate free zones, etc [1].

With increasing reduction in hot rolling, the strength and the fracture strain along the **transverse** direction were observed to increase significantly. These changes in the tensile behaviors can be seen in the superposed stress-strain curves obtained from the transverse specimens having various reduction ratios (Fig.4). Similar trends along the transverse direction have also been observed in the cold rolled composites [1], with the exception that the strength and the fracture strain of the cold rolled composites are lower than those of the hot rolled ones. On the other hand, along the **longitudinal** direction, such properties were relatively unaffected with increasing reduction in hot rolling. The variations in the tensile properties of the cold and the hot rolled composites (with respect to the reduction ratio) are illustrated graphically in Fig.5.

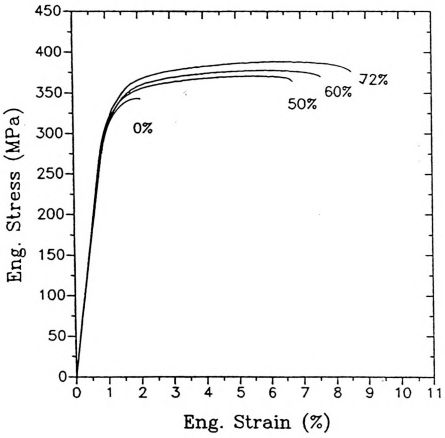

Fig.4 Superposed stress-strain curves for the transverse specimens having various reduction ratios, illustrating significant increase in strength and fracture strain with increasing reduction ratio.

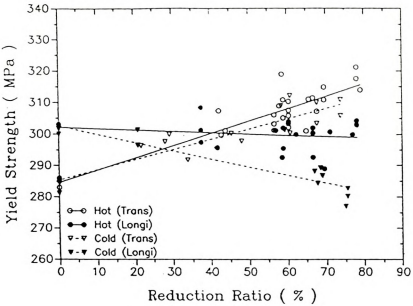

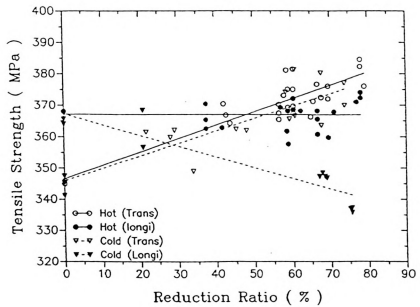

Fig.5 Plots of
a) Yield strength vs. Reduction ratio
b) Tensile strength vs. Reduction ratio
observed in the cold and the hot rolled composites

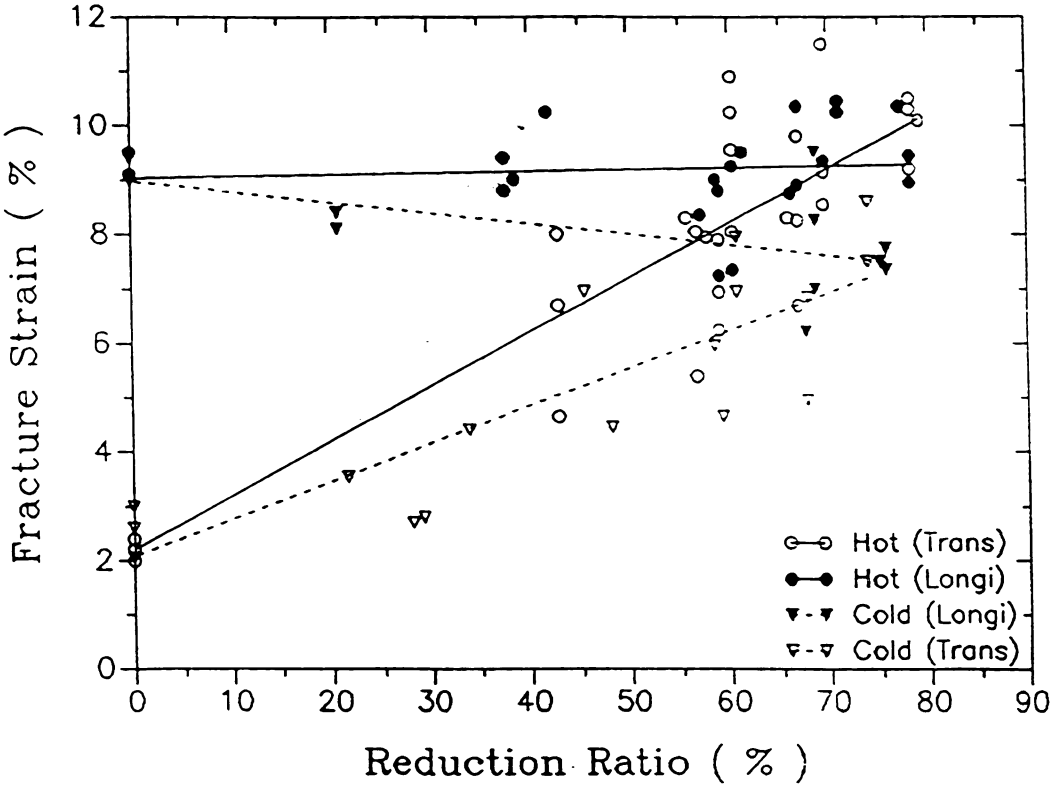

Fig.5 (Continued)
c) Fracture strain vs. Reduction ratio observed in the cold and the hot rolled composites.

4.ANALYSIS

Redistribution of $(Al_2O_3)_p$ clusters, disappearance of $(Al_2O_3)_p$ free zones, change in the matrix grain size, and damage to $(Al_2O_3)_p$ are responsible for the observed changes in the tensile properties. Each of these parameters, as affected by rolling, could either improve or deteriorate the tensile properties along different directions of the resultant composites. In this paper, the effects of redistribution of $(Al_2O_3)_p$ on the variations in the strength is analyzed, since detailed explanations concerning the effect of the other microstructural changes on the composite strength have already been reported [1].

4.1 Effect of redistribution of $(Al_2O_3)_p$ on the yield strength

4.1.1 Three dimensional composite model

In order to analyze the effects of particulate redistribution on the tensile properties, a simplified three-dimensional composite model based on the following assumptions is considered:

a. The extruded composite can be treated as a short (or discontinuous) fiber reinforced composite, where the fibers correspond to the clusterings of $(Al_2O_3)_p$ banded along the extrusion direction. In this analysis, such regions are termed as 'fiberils' and are assume to have square cross-section. $(Al_2O_3)_p$ free zones correspond to the matrix possessing the yield strength of the Al alloy (276 MPa),

b. The strength of the fiberils can be considered to be the strength of those regions with the associated higher volume fractions of $(Al_2O_3)_p$, and obtained from the experimentally measured and extrapolated regions in the plot given in Fig.6,

c. The individual particulate geometry does not contribute to the observed strength variations addressed in this model.

Based on the microscopic studies on the as-extruded composite, the approximate dimensions of these fiberils are about 300μm in length, with an average width and thickness of about 50μm. These fiberils are spaced approximately 50-100μm apart along the transverse direction, and they are spaced closely along the longitudinal direction. $(Al_2O_3)_p$ volume fractions in the fiberil regions are assumed to be about 30-40% based on the observations. A schematic of this composite is shown in Fig.7(a).

Rolling along the transverse direction spreads $(Al_2O_3)_p$ present within the fiberils along the transverse direction without changing the fiberil length along the longitudinal direction (due to the plane strain condition during rolling). The thickness of the fiberils decreases slightly as the reduction ratio increases, such that the thickness of the fiberils in 70% hot rolled composite reduces to about 2/3 of its initial thickness. At the same time, the matrix alloy present in the particulate free zone was observed to spread into the fiberils with increasing reduction, and this zone almost disappeared at about 70% reduction. Such a redistribution of $(Al_2O_3)_p$ due to rolling will decrease the strength of the fiberil due to decreased volume fraction of $(Al_2O_3)_p$within the fiberils (from 582MPa in the as-received composite to 356MPa in 70% rolled composite). However, the volume fraction of the fiberil within the composite will increase, from about 25% in the as-extruded composite to about 90% in the 75% hot rolled composite [Fig.7(b)]. In addition, the load carrying

capability of the fiberil should be changed to account for the changes in the fiberil dimensions, i.e, surface area of the fiberils.

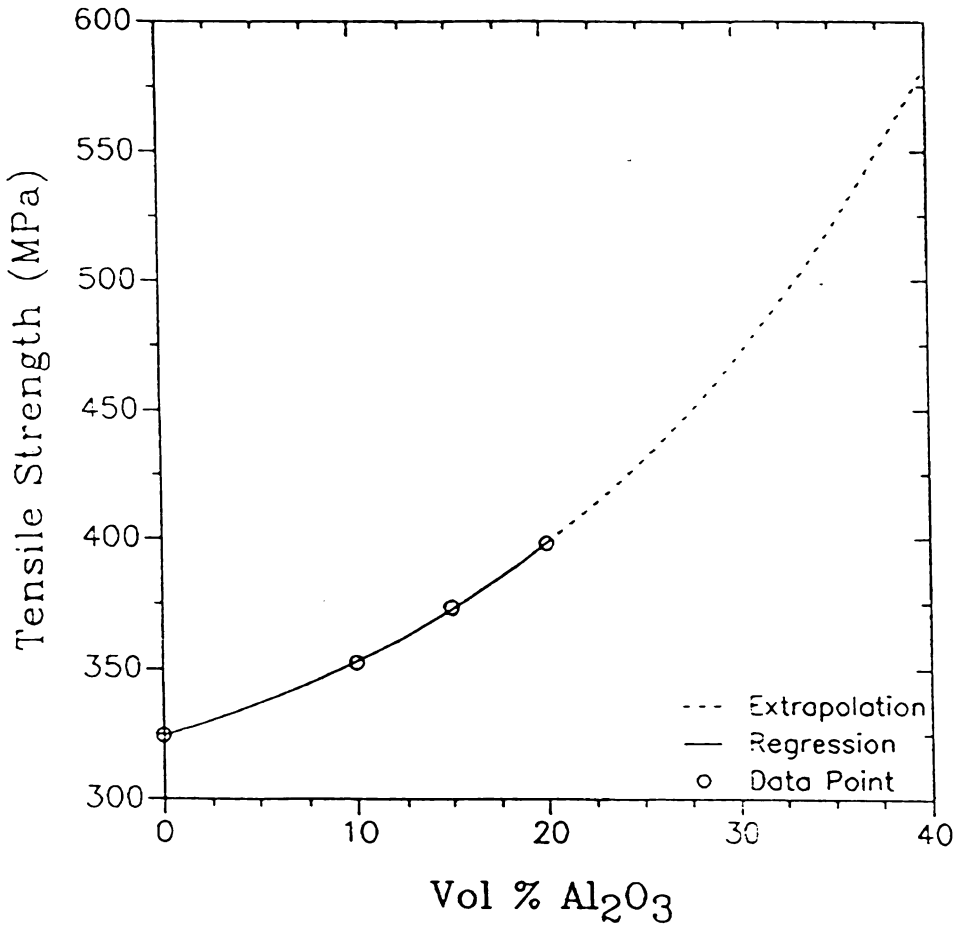

Fig.6 Tensile strength of 6061 Al alloy composite reinforced with various volume fractions of $(Al_2O_3)_p$. The broken portion of the plot is obtained by extrapolating the best fit solid curve.

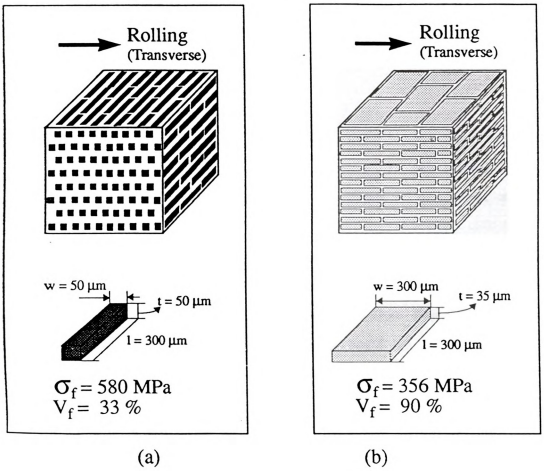

Fig.7 Schematics illustrating the three dimensional composite model
a) the as-received composite exhibiting the banded structure of the particulates each fiberil possesses 30-40% $(Al_2O_3)_p$
b) the 70% rolled composite exhibiting uniform distribution of $(Al_2O_3)_p$.

4.1.2 Theoretical consideration for the longitudinal and the transverse strength

The rule of mixtures has been successfully used to predict the strength of continuous fiber reinforced composites in which the fiber length(ℓ) is much larger than the critical fiber length(ℓ_c), and is given as

$$\sigma_c = \sigma_f V_f + \sigma_m V_m \quad (\text{if } \ell \gg \ell_c) \tag{1}$$

where σ_f is tensile strength of the fiber, σ_m is the stress in the matrix, and V_f and V_m are the volume fractions of the fiber and the matrix, respectively.

However, in case of short fiber reinforced composites, σ_f in Eq(1) has to be replaced by the average fiber stress($\bar{\sigma}_f$), since the average stress in a short fiber is always less than that found in a continuous fiber. As a result, the longitudinal strength of short fiber reinforced composite can be expressed as

$$\sigma_{\ell c} = \bar{\sigma}_f V_f + \sigma_m^* V_m \quad (\text{if } \ell > \ell_c) \tag{2}$$

where $\sigma_{\ell c}$ is the composite yield strength along the longitudinal direction, σ_m^* is the matrix stress at the fiber fracture strain (A useful approximation can be made by using the value of matrix yield strength in place of σ_m^*.), and $\bar{\sigma}_f$ is given by [7]

$$\bar{\sigma}_f = \sigma_f \left(1 - \frac{\ell_c}{2\ell} \right) \tag{3}$$

where ℓ_c is $(\frac{\sigma_f d}{2\tau_i})$, d is the fiber diameter (or fiber thickness), and τ_i is the shear stress at the interface which is assumed to be half the matrix yield strength. Substitution of Eq(3) and $V_m = (1-V_f)$ into Eq(2) yields

$$\sigma_{\ell c} = (\sigma_f - \sigma_m^* - \frac{\sigma_f^2 d}{2\sigma_m^* \ell})V_f + \sigma_m^* . \tag{4}$$

It is important to note, form Eq(4), that the longitudinal strength of the composite($\sigma_{\ell c}$) is a function of σ_f(fiberil strength) and V_f(fiberil volume fraction) only, since all other parameters in above equation can be assumed to remain constant for the case under consideration.

For the transverse specimen, the rule of mixture for a series alignment with the form of

$$\sigma_{tc} = \frac{\sigma_f \sigma_m^*}{\sigma_f V_m + \sigma_m^* V_f} \tag{5}$$

is used to predict the variation of the strength of the composite along the transverse direction. Again, from Eq(5), the transverse strength of the composite (σ_{tc}) is a function of σ_f and V_f only.

4.1.3. Calculations

The rule of mixture for the parallel and the series alignments of fiberils are applied to predict the variations in the composite strength. Data needed for the calculations of the longitudinal and the transverse strengths are listed in Table 1. The variations in the predicted strength obtained using the previously reported 2-D model [1] and the present 3-D model are compared with those in the measured strength as "the percent change in strength" in plots given in Fig.8. With increasing reduction in rolling, both 2-D and 3-D models show increasing and decreasing trends of the transverse and the longitudinal strengths. However, in general, 3-D model provides better prediction of these trends observed in this composite. In case of the hot rolled composites, the variations in the longitudinal and the transverse strength predicted by this model agree well with the experimental observations. In case of the cold rolled composites, however, the model provides the strength values much higher than the measured ones along the longitudinal direction, although it still shows good agreement for the transverse strength.

Table 1. Data needed for the calculations
(obtained on the basis of the composite model)

Rolling %	% Al_2O_3 in fiberil	σ_m^* (MPa)	σ_f (MPa)	V_f (%)
0	30	276	500	33
35	18	276	390	58
70	11	276	356	90

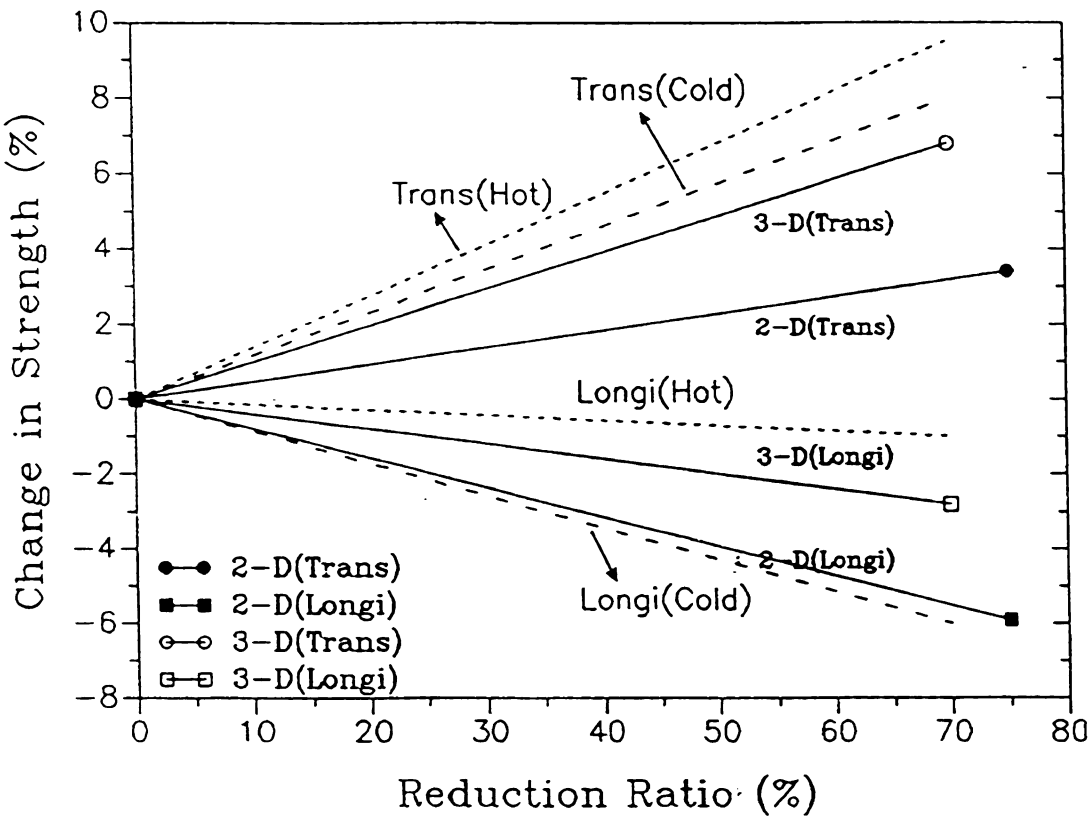

Fig.8 Plots comparing the predicted and the observed changes in the yield strength as a function of reduction ratios.

4.1.4. Discussion

The rolling operation along the transverse direction causes significant increase in the fiberil width with insignificant changes in the length and the thickness of the fiberil, as shown in Fig.7. Such increased width of the fiberil, i.e, change in the fiberil dimensions, should affect the load carrying capability of the fiberil along the longitudinal and the transverse directions. In this section, the maximum fiberil stress, which will be reflected as load carrying capability of the fiberil upon loading, was calculated as a function of fiberil dimensions and the matrix strength using the force equilibrium at the fiberil. Detailed derivations are provided in the APPENDIX V.

For the longitudinal composites, the maximum fiberil stress $[\sigma_f(\frac{\ell}{2})]$ due to the longitudinal loading was obtained as

$$\sigma_f(\frac{\ell}{2}) = \frac{\ell}{2} \left(\frac{1}{\omega} + \frac{1}{t} \right) \sigma_m \qquad (6)$$

where ℓ, ω, and t are the length, the width, and the thickness of the fiberil, and σ_m is the matrix yield strength. Since ℓ, t, and σ_m can be assumed to be constants, Eq(6) can be rewritten as

$$\sigma_f(\frac{\ell}{2}) \approx \alpha \frac{1}{\omega} + \beta \qquad (7)$$

where α and β are positive constants. 'ω' in Eq(7) increases with increasing reduction in rolling, resulting in a decrease in the maximum fiberil stress as shown in Fig.9. In addition, rolling along

the transverse direction causes the fiberil width increase without significant changes in its length and thickness. Such an increase in the fiberil width decreases the volume fraction of $(Al_2O_3)_p$ within the fiberil, decreasing the fiberil strength according to the plot given in Fig.6. However, the fiberil volume fraction within the composite increases with increasing reduction in rolling. Therefore, the observed slight decrease in the longitudinal strength of the hot rolled composite is due to the compromising effect of the decreased fiberil strength and increased fiberil volume fraction. Lower longitudinal strength observed in the cold rolled composites (compared to that of the hot rolled composite) is considered to be due to more significant damage to $(Al_2O_3)_p$ in case of the cold rolled composites.

For the transverse composites, the maximum fiberil stress $[\sigma_f(\frac{\omega}{2})]$ due to the transverse loading can be obtained as

$$\sigma_f(\frac{\omega}{2}) = \frac{\omega}{2} \left(\frac{1}{\ell} + \frac{1}{t} \right) \sigma_m. \qquad (8)$$

Eq(8) can be rewritten as

$$\sigma_f \left(\frac{\omega}{2}\right) \approx \gamma \, \omega \qquad (9)$$

where γ is a positive constant. Again, 'ω' in Eq(9) increases with increasing reduction, resulting in increased maximum fiberil stress (Fig.9), that will be reflected as increased load carrying capability of the fiberil along the transverse direction although fiberil strength itself decreases. Therefore, increase in the transverse

strength due to rolling is believed to be due to increased load carrying capability of the fiberil along the transverse direction as well as increased fiberil volume fraction within the composites. The changes in the maximum fiberil stress and the load carrying capability of the fiberil along the longitudinal and the transverse directions are schematically illustrated in Fig.10.

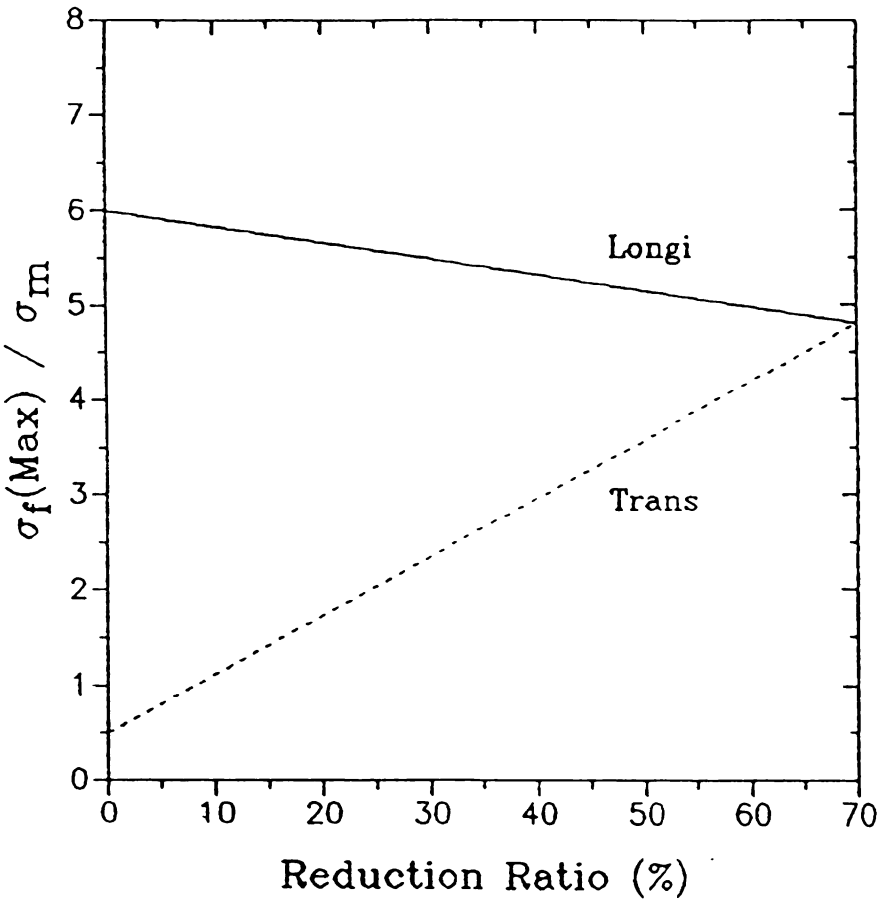

Fig.9 Variations in the normalized maximum fiberil stress [$\sigma_f(max)/\sigma_m$] as a function of reduction ratio.

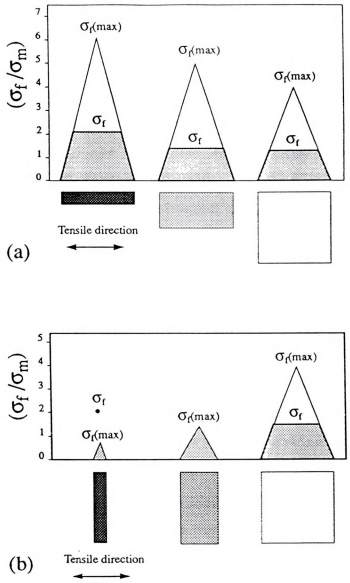

Fig. 10 Schematics illustrating the change in the maximum fiberil stress [σ_f(max)] and the loading carrying capability (shaded region) along (a) the longitudinal direction and (b) the transverse direction.

4.2 Effect of other parameters

Other factors contributing to variations of the strength along the longitudinal and the transverse directions have already been reported [1]. The results based on these findings can be summarized as follows;

i) Particulate damage (particulate cracking and interfacial debonding) should reduce the transverse strength due to its orientation relative to loading direction, and as a consequence cannot explain the increased transverse strength due to the rolling operation.

ii) Reduced grain size due to the rolling and T6 heat treating operations should increase the strength both along the longitudinal and the transverse directions, and as a result, cannot be used to explain the decreased strength along the longitudinal direction.

iii) With increasing reduction in rolling, the particulate free-zones gradually disappear to make uniform distribution of the particulates. During transverse loading of the rolled composite, the cracks that initially propagate through the particulate free-zones in the as-received composite, will be arrested, resulting in higher transverse strength. However, such a redistribution will not result in any decrement in the longitudinal strength.

iV) Several studies [8-10] have reported the transverse strength of discontinuous composites to be higher than the longitudinal one, based on the orientation of the individual particulates (with elliptical geometry) with respect to loading direction, when the reinforcements within the composites are uniformly distributed. This may be due to the fact that less severe stress concentration on the reinforcement

within the transverse specimen causes less particulate cracking and interfacial cracking under identical stress levels. As a result, the composite is able to withstand higher stresses along the transverse direction.

5. CONCLUSIONS

5.1 Microstructural features

With 35-45% reduction per pass, the grain size of the hot rolled composites is comparable to that of the cold rolled composite. Significant redistribution of $(Al_2O_3)_p$ clusters could be achieved using both cold and hot rolling. Most of the banded structure of $(Al_2O_3)_p$ clusters in the as-received extruded composites disappeared beyond 60-70 % of reduction. Substantial particulate damage in the form of particulate cracking and interfacial debonding occurs due to cold rolling. The extent of such damage could be minimized by hot rolling.

5.2 Tensile properties

The principal effects of cold and hot rolling on the tensile properties are that both rolling operations result in improved transverse tensile properties. However, the longitudinal tensile properties were observed to be generally decreased due to rolling. Such behaviors are mainly due to the redistribution of $(Al_2O_3)_p$. The strength and the fracture strain were measured to be higher in case of the hot rolled composites than the cold rolled ones due to less significant particulate damage in the hot rolled composites. The proposed three dimensional model was able to explain the observed trends qualitatively.

6. REFERENCES

1. J.C.Lee and K.N.Subramanian, "Effect of cold rolling on the tensile properties of $(Al_2O_3)_p$/Al composites" Mater. Sci. Eng., (In press)
2. J.C.Lee, Y.Kim and K.N.Subramanian, "Interface in Al_2O_3 particulate reinforced Aluminum alloy composite and its role on the tensile properties" (Submitted to J. Mat. Sci.).
3. J.C.Lee and K.N.Subramanian, "Young's modulus of cold and hot rolled $(Al_2O_3)_p$/Al composites" (Submitted to J. Mat. Sci.)
4. J.C.Lee and K.N.Subramanian, "Effect of cold rolling on the elastic properties of $(Al_2O_3)_p$/Al composite" J. Mat. Sci. (In press).
5. W.A.Anderson and R.F.Mehl, "Recrystallization of aluminum in terms of the rate of nucleation and the rate of growth" AIME. Trans., 161, 140-172 (1945).
6. J.D.Verhoeven, Fundamentals of Physical Metallurgy, p352, John Wiley & Sons, New York (1975).
7. G.S.Holister and C. Thomas, Fiber reinforced materials, p80, Elsevier Publishing Co. New York, 1966.
8. D.L.McDanels, "Analysis of stress-strain, fracture, and ductility behavior of aluminum matrix composites containing discontinuous Silicon carbide reinforcement" Metall. Trans. A, 16, 1105-1115, (1985).
9. M.G.McKimpson and T.E.Scott, "Processing and properties of metal matrix composites containing discontinuous reinforcement" Mat. Sci. Eng. A, 107, 93-106, (1989).
7. A.P.Divecha, S.G.Fishman, and S.D.Karmarkar, "Silicon carbide reinforced aluminum - A formable composite" J. Metals, 33, 12-17, (9.1981).
8. H.L.Cox, "The elasticity and strength of paper and other fibrous materials" Br. J. Appl. Phys. 3, 72-79, (1952).

Chapter VIII. GENERAL CONCLUSIONS

1. Interface characterization

X-ray diffraction carried out on $(Al_2O_3)_p$ powders extracted from the composite showed that the chemical reaction product at the interface of $(Al_2O_3)_p$/Al composite was a layer containing single crystals of $MgAl_2O_4$ spinel, believed to have grown at the surface of $(Al_2O_3)_p$ by the reaction between $(Al_2O_3)_p$ and Mg in the matrix alloy.

Interfacial debonding has been observed to occur predominantly along $MgAl_2O_4$/Al phase boundary rather than $MgAl_2O_4/Al_2O_3$ phase boundary, indicating relatively weak bond between $MgAl_2O_4$ layer and Al alloy matrix. Such a feature is responsible for the inferior tensile properties of this composite as compared to those of SiC_p/Al composite that exhibits less significant interfacial debonding.

2. Failure behavior

Theoretical modeling carried out in this study has been successful in providing the reasons for low ductility exhibited by the particulate reinforced metal matrix composites. According to these analyses, the microcracks originate due to the stress concentrations in the matrix near the pole of the reinforcement and within the reinforcement, and eventually result in interfacial debonding and

particulate cracking causing substantial decrease in the ductility of the composite.

Since particulate cracking and interfacial debonding were observed to precede the matrix failure, such phenomena appear to be more responsible for the failure of this composite than a mechanism based on the matrix failure.

3. Material property variation

Rolling and annealing operation carried out on the composite results in significant microstructural changes, such as redistribution of $(Al_2O_3)_p$, grain size, particulate damage, texture, etc. In particular, most of the banded structure of $(Al_2O_3)_p$ clusters in the as-received extruded composite disappeared beyond 60-70 % of reduction in rolling as a result of the redistribution of $(Al_2O_3)_p$. Substantial particulate damage in the form of particulate cracking and interfacial debonding occurs due to rolling pressure.

These changes in the microstructure could be correlated with the observed variations in the elastic properties of the rolled composites. Disappearance of $(Al_2O_3)_p$ clusters and texture formation were found to increase the elastic modulus of the composite. Damage to $(Al_2O_3)_p$, however, decreases the elastic modulus, whereas change in the grain size does not have significant influence on the same properties. The combined effect of these parameters on the variations

in the elastic modulus (as a function of the reduction ratio) was found to have the form of

$E = E_o (1 + \alpha e^{\beta X} - \eta X)$.

The principal effects of cold and hot rolling on the strength and the fracture strain are that both rolling operations result in significant improvement in these properties along the transverse direction, whereas, along the longitudinal direction, the fracture strain remains almost the same regardless of the rolling conditions and the reduction ratio. However, the longitudinal strength of the cold rolled composite decreased with increasing reduction ratio. Such behaviors are believed to be mainly due to the redistribution of $(Al_2O_3)_p$. These increasing and decreasing tendencies could be explained using a simplified three dimensional composite model. The strength and the fracture strain of the hot rolled composites were found to be higher than those of the cold rolled composites, due to less significant particulate damage.

APPENDIX I.

EFFECT OF CERAMIC REINFORCEMENT ON THE MATERIAL PROPERTIES OF Al ALLOY COMPOSITES

Number of studies regarding the metal matrix composites reinforced with various ceramic particles have concentrated on the accumulation of some basic mechanical properties, such as strength, Young's modulus, ductility, fatigue, and fracture toughness. These properties are reviewed on the basis of the data reported in the literatures due to the importance in engineering design. The selected mechanical properties of aluminum alloy matrix composites reinfroced with various ceramic reinforcements are given in Table.1. The typical characteristics of various ceramic reinforcements are also given in Table.2.

A.I.1 Strength

Although the strength of metal matrix composites depends on the type [1-4], size [5,6], morphology [1,2,7], and the volume fraction [1-4] of the reinforcements, and the processing techniques [3,8], it predominantly depends on the strength of the matrix alloy and the heat treatments employed in the composites (Fig.1). Significant increase in the strength of the composites was observed, especially when the reinforcements are incorporated into low strength Al alloys (Fig.2). In case of high strength Al alloy (such as 7090 Al alloy) composites, the strengthening due to reinforcements is not as effective as that

for the low strength Al alloy [Fig.1(b)]. Such results are probably due to substantially high stress states both at the interface and within the reinforcement even under the identical stress concentration factor near the reinforcements, resulting in interfacial debonding and fracture of the reinforcements. The details regarding the failure mechanism and its effect on the tensile properties of the composites were discussed in CHAPTER II.

A.I.2 Young's modulus (Elastic modulus)

Young's modulus is one of the inherent material property of a material, which is related with interatomic bond energy of the material. Thus, unlike the other material properties, the Young's modulus of the material does not undergo significant change with respect to their microstructural changes. In case of commercial Al alloys, Young's moduli are ranged from 68 to 72 GPa. Substantial increase in the Young's modulus of aluminum alloys have been achieved by introducing ceramic reinforcements possessing considerably high Young's moduli (ranging from 400 to 600 GPa). As a result, the Young's moduli of metal matrix composites reinforced with ceramic particulates are predominantly dependent on the volume fraction of the reinforcements. On the other hand, the orientation, type, size, and morphology of the reinforcements, and the nature of the matrix material play insignificant roles in determining the modulus as can be seen in Figs.3(a) and 3(b). Various theoretical and empirical relationships to predict the Young's moduli of discontinuous reinforced composites are well reviewed elsewhere [9].

Table 1. Mechanical and physical properties of some ceramic reinforced aluminum alloy composites
(Materials are all T6 heat treated except 1100 Al composites.)

Material	E (GPa)	Y.S (MPa)	UTS (MPa)	ϵ (%)	Ref
0 % SiC_p/ 1100	-	63.4	98.6	41.0	1
10 % SiC_p	-	82.8	157.2	24.0	1
19 % SiC_p	-	109.7	199.3	16.0	1
31 % SiC_p	-	172.4	273.8	6.0	1
9 % SiC_w/ 1100	-	103.4	204.8	16.0	1
18 % SiC_w	-	183.4	324.1	5.0	1
28 % SiC_w	-	246.2	424.1	4.0	1
0 % B_4C_p/ 6061	68.9	276.0	310.0	20.0	3
10 % B_4C_p	-	311.0	342.8	5.9	1
20 % B_4C_p	-	395.9	464.1	4.7	1
30 % B_4C_p	-	426.2	503.4	2.4	1
15 % SiC_p/ 6061	96.5	399.9	455.1	7.5	2,4
20 % SiC_p	103.4	413.7	496.4	5.5	2
25 % SiC_p	113.8	427.5	517.1	4.5	2,4
30 % SiC_p	120.7	434.4	-	3.0	2,4
35 % SiC_p	134.4	455.1	551.2	2.7	2
40 % SiC_p	144.8	448.2	586.1	2.0	2
10 % $(Al_2O_3)_p$/ 6061	81.4	296.0	310.0	7.6	3
15 % $(Al_2O_3)_p$	87.6	317.0	359.0	5.4	3
20 % $(Al_2O_3)_p$	98.6	359.0	379.0	2.1	3

Table 1. (Continued)

Material	E (GPa)	Y.S (MPa)	UTS (MPa)	ϵ (%)	Ref
0 % SiC_p/ 2124	72.4	388.0	440.0	8.0	5
20 % SiC_p	103.4	399.9	551.6	7.0	2,4
25 % SiC_p	113.8	413.7	565.4	5.6	2
30 % SiC_p	120.7	441.3	592.9	4.5	2,4
40 % SiC_p	151.8	517.1	689.5	1.1	2,4
0 % SiC_p/ 7090	-	-	-	-	
20 % SiC_p	103.4	655.0	723.9	2.5	2
25 % SiC_p	115.1	675.7	792.9	2.0	2
30 % SiC_p	127.6	703.3	772.2	1.2	2
35 % SiC_p	131.0	710.2	723.9	0.9	2
40 % SiC_p	144.8	689.5	710.2	0.9	2

Table 2. Characteristics of some important ceramic reinforcements (Ref.7)

Material	shape	size	Density (g/cm^3)	UTS (GPa)	E (MPa)
Graphite	p	40-250 μm	1.6-2.2	20	910
SiC	p	15-340 μm	3.2	3	480
B_4C	p	40-340 μm	2.5	6.5	480
Al_2O_3	p	40-340 μm	3.97	8	460
SiC	Cyl.w	50 mm x 0.1 μm	3.2	3-14	400-700
SiC	Hex.w	50 mm x 0.2 μm	3.2	13	700
Al_2O_3	Cyl.w	100 mm x 2 μm	3.97	15	2275
Carbon T300	f	2.5 mm x 7.8 μm	1.75	3.45	230
SiC Nicalon	f	1-6 mm x 10 μm	2.55	3	195
Al_2O_3 FP	f	3-6 mm x 15 μm	3.96	1.7	380
Al_2O_3 Saffil	f	0.1-1 mm x 1-5 μm	3.3	2	300

Note: P = Particulate
w = Whisker
f = Fiber

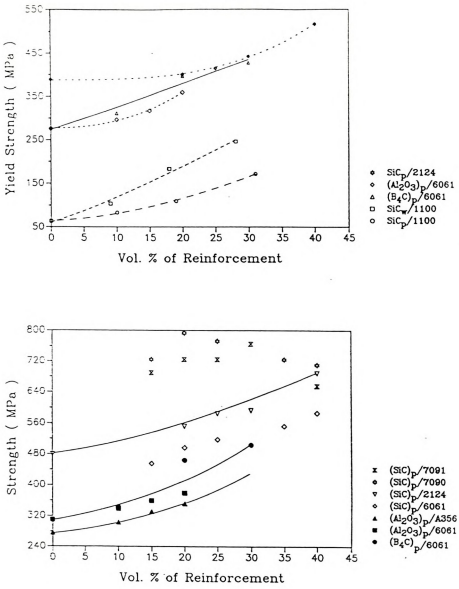

Fig.1 Plots showing the variations in the strength as a function of volume fraction of the reinforcements.

a) Yield strength vs. volume fraction

b) UTS vs. volume fraction.

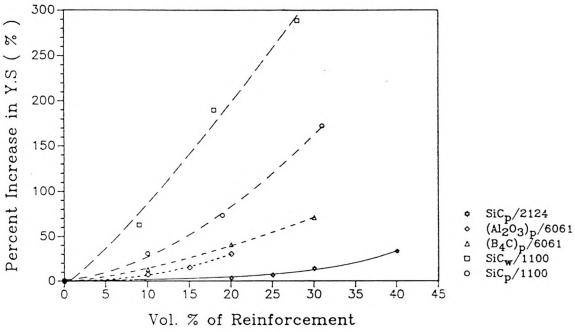

Fig.2 A plot showing percent increase in the yield strength as a function of volume fraction of the reinforcements. Notice that percent increase in yield strength is higher in case of low strength Al alloy.

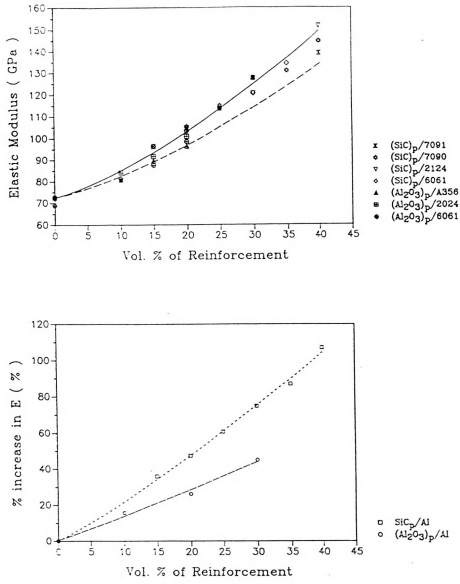

Fig.3 a) A plot showing the variations in the Young's modulus as a function of the volume fraction of the reinforcement.

b) A plot showing the percent increase in the Young's modulus as a function of volume fraction of the reinforcements.

A.I.3 Ductility

Although substantial increase in the strength and the Young's modulus can be obtained by introducing small or moderate amounts of ceramic reinforcements, such improvements are always associated with more than one order of magnitude decrease in the fracture strain (Fig.4). As expected from the low ductility exhibited by these composites, the observations of the fracture surface of the composites reveal (macroscopically) brittle nature, although very fine sized dimples can be seen in the matrix nearby the fractured reinforcements (Fig.5). Such a brittleness is believed to be due to various failure mechanisms operative in these types of composites. Detailed explanations concerning this feature were discussed in Chapter II.

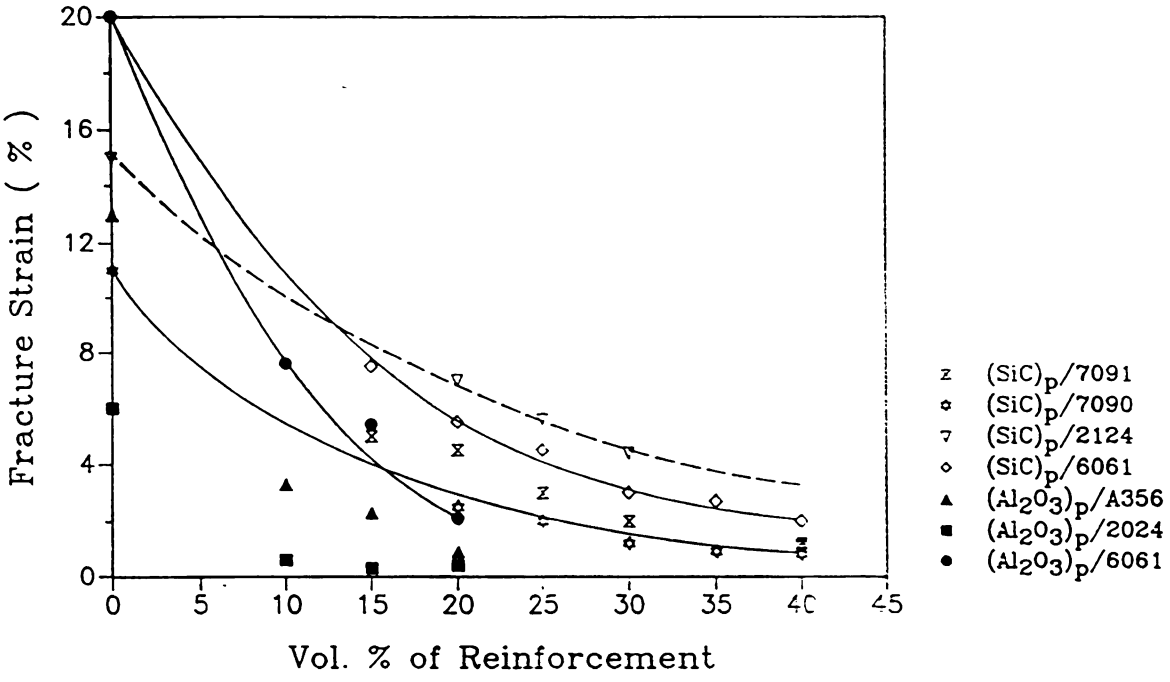

Fig.4 The variations in ductility as a function of the volume fraction of the reinforcements.

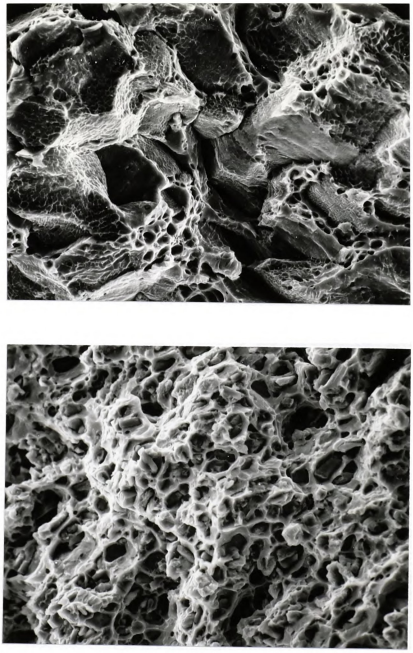

Fig.5 Typical fracture surface observable in a) 6061 Al alloy and b) $(Al_2O_3)_p$/Al composites

A.I.4. REFERENCES

1. T.G.Nieh and D.J.Chellman, "Modulus measurements in discontinuous reinforced aluminum composites", Scr. Metall., 18, 925-928, (1984).

2. DWA data in "Increasing focus on silicon carbide reinforced aluminum composites", Light Metal Age, 7-14, (June, 1986).

3. W.A.Hoover, "Commercialization of Duralcan aluminum composites", Proceedings of the fifth annual ASM/EDS advanced composites conference, Detroit, Michigan, Oct. 1989, 211-217, published by ASM International, Materials Park, Ohio, (1989).

4. W.C.Harrigan, Jr., Gaebler, E.Davis, and E.J.Levin, "the effect of hot rolling on the mechanical properties of SiC-reinforced 6061 Aluminum", Mechanical behavior of metal-matrix composites, Proceedings of a symposium sponsored by the Composite Materials Committee of the Metallurgical Society of AIME and the Materials Science Diviosion of American Society for Metals, held at the 111th AIME Annual Meeting, Dallas, Tx, 1982, 169-180, published by Metallurgical Society of AIME, Warrendale, Pa, (1983).

5. J.K.Shang, W.Yu, and R.O.Ritchie, "Role of silicon carbide particles in fatigue crack growth in SiC-particulate-reinforced aluminum alloy composites", Mat. Sci. Eng. A, 102, 181-192, (1988).

6. J.J.Stephenes, J.P,Lucas, and F.M.Hoskinng, "Cast Al-7Si composites: effect of particle type and size on mechaniical properties", Scr. Metall., 22, 1307-1312, (1988).

7. D.L.McDanels, "Analysis of stress-strain, fracture, and ductility behavior of aluminum matrix composites containing discontinuous silicon carbide reinforcement", Metall. Trans. A, 16, 1105-1115, (1985).

8. R.J.Arsenault and S.B.Wu, "A comparision of PM vs. Melted SiC/Al composite", Scr. Metall., 22, 767-772, (1988).

9. S.Ahmed and F.R.Jones, "A review of particulate reinforcement theories for polymer composites", J. Mat. Sci., 25, 4933-4942, (1990).

APPENDIX II.

MECHANISM OF STRENGTHENING DUE TO REINFORCEMENTS IN METAL MATRIX COMPOSITES

The addition of ceramic reinforcement in the forms of fibers, whiskers, and particulates into metal matrix can lead to significant increase in yield strength and Young's modulus, while there are some negative effects on the mechanical properties such as decrease in ductility.

Although the theories for the strengthening mechanism of Al alloy composites reinforced with ceramic particles, such as SiC_p, $(Al_2O_3)_p$, B_4C, etc., have not yet been completely established, some plausible strengthening mechanisms, such as Orowan strengthening due to impediment of dislocation motion, composite strengthening due to load transfer, thermal strain hardening due to enhanced dislocation density, can be considered to explain the strengthening of discontinuously reinforced metal matrix composites. Therefore the expected yield strength of such composites can be expressed as

$$\sigma_{cy} = \sigma_{my} + \Delta\sigma \qquad \text{A1)}$$

where σ_{cy} = yield strength of the composites

σ_{my} = yield strength of the matrix

$\Delta\sigma$ = increase in yield strength due to reinforcement

$= \Delta\sigma_{orowan} + \Delta\sigma_{comp} + \Delta\sigma_{disloc}$

$\Delta\sigma_{orowan}$ = increase in yield strength due to dislocation looping

$\Delta\sigma_{comp}$ = increase in yield strength due to load transfer

$\Delta\sigma_{disloc}$ = increase in yield strength due to the increased dislocation density.

A.II.1 Orowan strengthening

If the reinforcement exists as particles, Orowan strengthening mechanism is a possiblity. The Orowan-Ashby equation [1] for looping of precipitates by dislocation is given by

$$\Delta\tau = [0.81 \cdot \mu \cdot b]/[2\pi \cdot (1-\nu)^{2} \cdot D^{2}] \cdot \ln(2r_{o}/b) \qquad A2)$$

where $\Delta\tau$ = increase in resolved shear stress due to the precipitates

μ = shear modulus of the matrix (28 GPa for 6061 Al-T6)

ν = Poisson's ratio (0.33 for most Al alloy)

r_{o} = mean particulate radius

b = Burger's vector (2.86×10^{-8}cm for aluminum)

D = effective interparticulatespacing [1] $[(Lt/V_{p})^{1/2}]$

L = length of the reinforcement

t = thickness of the reinforcement, and

V_{p} = volume fraction of the reinforcement.

The increase in yield strength ($\Delta\sigma$) due to the increased shear strength can be expressed as

$$\Delta\sigma = M \cdot \Delta\tau \qquad A3)$$

where M is approximately equal to 2. The increase in yield strength ($\Delta\sigma$) calculated by using the appropriate values for SiC_p/Al composite in this model is only about 2 MPa, while the observed increase in yield strength for T6 treated composites is about 30-40MPa. Based on this analysis, Orowan strengthening mechanism contributes very little to the strengthening of Al alloy composites reinforced with ceramic particles. This is due to the fact that the interspacing between the reinforcements within the composites is usually too large for dislocations to be bowed between the reinforcement during deformation.

A.II.2 Composite Strengthening

$\Delta\sigma_{comp}$ arises due to the load transfer from the matrix to the reinforcement through the interface. The strengthening depends on the efficiency of the load transfer from the matrix to the reinforcement, which largely relies on the interfacial bonding strength, shape of the reinforcement.

In 1952, Cox [2] developed the shear lag model to predict the strength of fiber reinforced composites. The most important assumption in this model is that the load transfer occurs only between the fiber and matrix by means of shear stress at the fiber/matrix interface. This theory can be used successfully for predicting the yield strength of composites having reinforcement with large aspect ratio. However, underestimation in the strength is expected for whisker or particulate reinforced composites, since the normal load

transfer at the whisker and particulate ends was ignored in the shear lag theory.

In 1986, Nardone and Prewo [3] proposed a modified shear lag model to explain the strengthening of discontinuously reinforced composites having small aspect ratio reinforcements such as SiC_p and SiC_w. The modified shear lag theory for particulate reinforced composites gives the composites yield strength (σ_y) by the following equation [3]:

$$\sigma_y = \sigma_{my} \left[1 + (\ell+t)\cdot s/(4\ell)\right]\cdot V_p + \sigma_{my}\, V_m \qquad \text{A4)}$$

where σ_{my} = yield strength of the matrix (240-280 MPa for 6061 Al-T6)

ℓ = length of the particulate perpendicular to the applied stress

t = thickness of the reinforcement

V_p = volume fraction of the reinforcement

V_m = volume fraction of the matrix ($1-V_p$)

s = particulate shape factor (2L/t)

L = particulate length in the tensile direction.

If $\ell \approx t$,

$$\sigma_y \approx \sigma_{my} \left[1 + s/2\right]\cdot V_p + \sigma_{my}\, V_m \ . \qquad \text{A5)}$$

Therefore, the increases in yield strength due to composite strengthening ($\Delta\sigma_{comp}$) for particulate reinforcement is given by

$$\Delta\sigma_{comp} = \sigma_y - \sigma_{my}$$
$$= \sigma_{my} \left[(1+s/2)\cdot V_p + V_m - 1\right]$$
$$= \sigma_{my} \, (s/2) \, V_p \, . \qquad \text{A6)}$$

According to Eq (A6), if the morphology (i.e, shape factor) and the volume fraction of the reinforcement are fixed, the only contributing factor to the increase in composite yield strength is the yield strength of the matrix material. With appropriate values of 's' (equal to 4) and V_p (equal to 0.1) for SiC_p/Al composite, $\Delta\sigma_{comp}$ becomes equal to 47 MPa. (Experimentally observed increase in yield strength is about 30-40 MPa.)

Interparticulatespacing (D) can also affect the composite yield strength. Such an effect on the strength can be explained by considering the equation suggested by Arsenault and Shi [4]

$$\Delta\sigma = 7Gb \left[\left(\frac{V_p^{1/2}}{1 - V_p}\right) \cdot \frac{\Delta\epsilon}{Db} \right]^{1/2} \qquad \text{A7)}$$

where $\Delta\sigma$ = increase in the yield strength of the composite

G = shear modulus of the matrix

b = Burger's vector

$\Delta\epsilon$ = thermal strain mismatch between the particulate and the matrix.

Eq(A7) indicates that, for a fixed volume fraction of the reinforcement, the composite yield strength can be increased by using finer reinforcement which results shorter interparticulatespacing.

A.II.3 Thermal strain hardening

Arsenault and Fisher have proposed a strengthening mechanism based on the increased dislocation density in the matrix caused by the large difference (10:1) in the thermal expansion coefficient between the Al matrix and SiC_p in the composites [5]. A high dislocation density of 10^9-$10^{12}cm^{-2}$ was observed experimentally in the matrix region near the reinforcements during cooling down from the annealing temperature to the room temperature [6]. The increase in the shear stress ($\Delta\tau$) due to the presence of dislocations can be expressed as

$$\Delta\tau = \alpha' \cdot \mu \cdot b \cdot \sqrt{\rho} \qquad \text{A8)}$$

where $\alpha' \approx$ constant, approximately equal to 0.5

μ = shear modulus of matrix (28 GPa for 6061 Al-T6)

b = Burger's vector (2.86×10^{-8}cm for Aluminum), and

ρ = dislocation density of the matrix.

Therefore, the following equation may be used for estimating the increase in yield strength ($\Delta\sigma_{disloc}$) due to the increased dislocation density:

$$\Delta\sigma_{dislo} = \alpha \cdot \mu \cdot b \cdot (\sqrt{\rho} - \sqrt{\rho_o}) \qquad A9)$$

where α = 1.25 for Al [7]

ρ = dislocation density in the matrix in regions adjacent to reinforcement

ρ_o = dislocation density in the matrix in the absence of SiC_p ($\approx 10^6 cm^{-2}$ for annealed Al).

Since ρ is much larger than ρ_0, Eq(A9) can be reduced into

$$\Delta\sigma_{disloc} = \alpha \cdot \mu \cdot b \cdot \sqrt{\rho}$$
$$= 1.25\ \mu \cdot b \cdot \sqrt{\rho}\ . \qquad A10)$$

In 1986, Arsenault and Shi developed an equation for evaluating the dislocation density by using the model of "the prismatic punching of dislocations" [4]. From their analysis, the dislocation density in the matrix was found to be

$$\rho = [B \cdot V_p \cdot \Delta\epsilon]/[(1-V_p) \cdot b \cdot d] \qquad A11)$$

where B = a geometric constant with a value between 4 and 12 (8 for particulate reinforcement)

V_p = volume fraction of reinforcement

$\Delta\epsilon$ = misfit strain due to the difference in the thermal expansion coefficient (equal to $\Delta\alpha \cdot \Delta T$)

b = Burger's vector

d = the smallest dimension of the particulate

Substitution of Eq(A11) into Eq(A10) results in the final expression for the increases in yield strength due to the increased dislocation density as

$$\Delta\sigma_{disloc} = 3.54\ \mu \cdot b \cdot [\ (V_p \cdot \Delta\alpha \cdot \Delta T)/((1-V_p) \cdot b \cdot d)\ ]^{1/2}. \qquad A12)$$

For a fixed volume fraction of reinforcement, significant increase in $\Delta\sigma_{disloc}$ is expected by incorporating the smaller size of reinforcement. For $V_p = 0.1$ and $d = 10\ \mu m$, 22 MPa increase in yield strength is expected due to the enhanced dislocation density in SiC_p/Al composite. However, such an increase in the yield strength of the composite is believed to be overestimated, since the enhanced dislocation density due to thermal expansion coefficient mismatch is localized just in the vicinity of the reinforcement only.

All these parameters contribute the strengthening of such composites. According to the discussions made so far, approximately 70 MPa of theoretical increase in yield strength is expected by incorporating 10% of SiC_p into Al alloy matrix. (However, the observed increased in yield strength was only about 30-40 MPa.)

A.II.4 REFERENCES

1. J.H.Beatty and G.J.Shiflet, "Orowan strengthening by MO_2C fibers and needle interphase precipitates in Fe-C-Mo dual-phase steel", Metall. Trans. A, 19, 1677-1620, (1988).

2. H.L.Cox, "The elasticity and strength of paper and other fibrous materials", Br. J. Appl. Phys., 3, 72-79, (1952).

3. V.C.Nardone and K.M.Prewo, "On the strength of discontinuous silicon carbide reinforced aluminium composites", Scr. Metall., 20, 43-48, (1986).

4. R.J.Arsenault and N.Shi, "Dislocation generation due to difference between the coefficients of thermal expansion", Mat. Sci. Eng. 81, 175-187, (1986).

5. R.J.Arsenault and P.H.Fisher, "Microstructure of fiber and particulate SiC in 6061 Al composites", Scr. Metall. 17, 67-71, (1983).

6. M.Vogelsang, R.J.Arsenault and P.M.Fisher, "An in situ HEVM study of dislocation generation at Al/SiC interface in metal matrix composites", Metall. Trans. A, 17, 379-389, (1986).

7. N.Hansen, "The effect of grain size and strain on the tensile flow stress of aluminium at room temperature", Acta Metall., 25, 863-869, (1977).

APPENDIX III.

DERIVATION OF STRESS STATES ON A LARGE THIN PLATE HAVING A CIRCULAR INCLUSION

Consider a large thin plate having a circular inclusion, whose elastic constants and thermal expansion coefficient are different from those of the matrix. Uniform uniaxial loading is applied at infinity on the composite system as shown in Fig.5(a) in Chapter.II. One can solve this problem by superposing the stress function due to uniaxial loading and stress function due to the inelastic strain caused by thermal expansion mismatch as in Fig.5(b) in Chapter II.

A.III.1 Large plate having a circular inclusion with different elastic constants subjected to uniaxial tension.

A.III.1.1. State of stress at infinity due to applied loading

When a large plate is subjected to uniaxial loading along x-axis, the stress components at infinity ($x = \infty$) are given by

$$\sigma_{xx} = \sigma_0 \qquad \text{A1)}$$

$$\sigma_{xy} = \sigma_{yy} = 0 \qquad \text{A2)}$$

,where σ_0 is the applied stress and θ is the angle measured from the tensile direction.

Since $\sigma_{xx} = \partial^2\Phi/\partial y^2$, the Airy stress function (Φ) which describes the uniaxial loading at infinity, is

$$\Phi(x,y) = (\sigma_0 \, y^2)/2. \qquad \text{A3}$$

$\Phi(x,y)$ in Eq A3) can be rewritten in polar coordinate as

$$\begin{aligned} \Phi(r,\theta) &= \sigma_0 \, r^2 \, \sin^2\theta \, /2 \\ &= \sigma_0 (\, r^2 - r^2 \cos 2\theta \,)/4. \end{aligned} \qquad \text{A4}$$

Once the stress function is determined, the corresponding stress components can be evaluated in polar coordinate using the following relations:

$$\sigma_{rr}(r,\theta) = \left(\frac{1}{r} \frac{\partial \Phi}{\partial r} \right) + \left(\frac{1}{r^2} \frac{\partial^2 \Phi}{\partial \theta^2} \right) + V \qquad \text{A5.a}$$

$$\sigma_{r\theta}(r,\theta) = - \frac{\partial}{\partial r} \left(\frac{1}{r} \frac{\partial \Phi}{\partial \theta} \right) \qquad \text{A5.b}$$

$$\sigma_{\theta\theta}(r,\theta) = \left(\frac{\partial^2 \Phi}{\partial r^2} \right) + V \qquad \text{A5.c}$$

,where V is the body force.

Thus, assuming no body force, the stress components at infinity solved for Eq A4) are;

$$\sigma_{rr}(\infty,\theta) = \sigma_0 \, (1+\cos 2\theta)/2 \qquad \text{A6.a}$$

$$\sigma_{r\theta}(\infty,\theta) = -\sigma_0 \, \sin 2\theta/2 \qquad \text{A6.b}$$

$$\sigma_{\theta\theta}(\infty,\theta) = \sigma_0 \, (\, 1-\cos 2\theta \,)/2. \qquad \text{A6.c}$$

A.III.1.2. State of stress in a large plate with an inclusion

Consider a plate having a small circular elastic inclusion of radius 'a', which is subjected to uniaxial tension. As illustrated in Eq A4), the Airy stress function under such a condition can be given as a linear combination of the function of polar coordinates r and θ. Thus, the possible selections in Φ can be;

$$\Phi^{1}(r,\theta) = L\{\ r^2,\ \log r,\ r^2\log r,\ r^2\cos 2\theta,\ \cos 2\theta/r^2,\ r^4\cos 2\theta,\ \cos 2\theta\ \}.$$

,where Φ^{1} is the Airy stress function due to remote uniaxial tension. By considering the stress components obtained using Eq A5), the stress functions for the matrix and the inclusion can be determined. Matrix part of this function, Φ^{m1} is

$$\Phi^{m1}(r,\theta) = A'r^2 + B'r^2\cos 2\theta + C'\log r + D'\cos 2\theta + E'\cos 2\theta/r^2 \qquad \text{A7.a)}$$

The constants A' and B' are determined as $A' = \sigma_0/4$ and $B' = \sigma_0$ from the boundary conditions at infinity given in Eq A6). Hence, Φ^{m1} can be reduced into

$$\Phi^{m1}(r,\theta) = \frac{\sigma_0}{4} r^2(\ 1-\cos 2\theta\ ) + \frac{\sigma_0}{4}\left[\ Aa^2\log r + Ba^2\cos 2\theta + Ca^4\frac{\cos 2\theta}{r^2}\ \right] \qquad \text{A7.b)}$$

One can notice that the first term in Eq A7.b) describes the undisturbed field (when there in no inclusion in the matrix), and the last three terms describe the local disturbance due to the discontinuity (i,e inclusion) in the elastic medium. However, according to the Saint

Venant's principle, the disturbance caused by discontinuity will be negligible at distances which are larger compared to the radius of the discontinuity.

The Airy stress function for the inclusion (Φ^{i1}) can be obtained using same method.

$$\Phi^{i1}(r,\theta) = \frac{\sigma_0}{4}\left(Dr^2 + Er^2\cos 2\theta + \frac{F}{a^2} r^4\cos 2\theta \right) \qquad \text{A8)}$$

,where D, E, and F are constants.

Once Φ^{m1} and Φ^{i1} were obtained, the stress components (σ_{ij}) can be obtained using Eq A5) and the displacement components (u_i) can also be determined using the Hooke's law and strain-displacement relationships: The Hooke's law for plane elasticity is

$$e_{\alpha\beta} = \frac{1}{2\mu}\left(\sigma_{\alpha\beta} - \frac{(3-\kappa)}{4}\sigma_{\gamma\gamma}\delta_{\alpha\beta} \right) + e^*_{\alpha\beta} + \eta\, e^*_{zz}\delta_{\alpha\beta} \qquad \text{A9)}$$

where $\kappa = 3 - 4\nu$ for plane strain condition

$= (3-\nu)/(1+\nu)$ for plane stress condition

ν = Poisson's ratio

δ = Kroneker delta

α,β,γ = r and θ

μ = shear modulus

$(e^*_{\alpha\beta} + \eta\, e^*_{zz}\delta_{\alpha\beta})$ = inelastic strain

$\eta = \nu$ for plane strain

$= 0$ for plane stress

and the strain-displacement relationships in polar coordinate are

$$e_{rr} = \frac{\partial u_r}{\partial r} \qquad \text{A10.a)}$$

$$e_{r\theta} = \frac{1}{2}\left[r\frac{\partial}{\partial r}\left(\frac{u_\theta}{r}\right) + \frac{1}{r}\frac{\partial u_r}{\partial \theta} \right] \qquad \text{A10.b)}$$

$$e_{\theta\theta} = \frac{1}{r}\left[\frac{\partial u_\theta}{\partial \theta} + u_r \right] \qquad \text{A10.c)}$$

.

Thus, the stresses and displacements in the matrix and the inclusion are

$$\sigma^{m1}_{rr} = (\sigma_0/2)[\ 1 + Aa^2/r^2 + (\ 1-2Ba^2/r^2-3Ca^4r^4\ )\cos2\theta\ ] \qquad \text{A11.a)}$$

$$\sigma^{m1}_{r\theta} = (-\sigma_0/2)[\ 1 + Ba^2/r^2 + 3Ca^4/r^4\ ]\sin2\theta \qquad \text{A11.b)}$$

$$\sigma^{m1}_{\theta\theta} = (\sigma_0/2)[\ 1 - Aa^2/r^2 - (\ 1-3Ca^4/r^4)\cos2\theta\ ] \qquad \text{A11.c)}$$

$$u^{m1}_r = (\sigma_0/8\mu^m)[\ (\kappa^m-1)r - 2Aa^2/r + \{\ 2r + B(\kappa^m+1)a^2/r + 2Ca^4/r^3\ \}\cos2\theta\ ] \qquad \text{A11.d)}$$

$$u^{m1}_\theta = (\sigma_0/8\mu^m)[\ -2r - B(\kappa^m-1)a^2/r + 2Ca^4/r^3\ ]\sin2\theta \qquad \text{A11.e)}$$

$$\sigma^{i1}_{rr} = (\sigma_0/2)[\ D - E\cos2\theta\ ] \qquad \text{A11.f)}$$

$$\sigma^{i1}_{r\theta} = (\sigma_0/2)[\ E + 3Fr^2/a^2\ ]\sin2\theta \qquad \text{A11.g)}$$

$$\sigma_{\theta\theta}^{i^1} = (\sigma_0/2)[\ D + (\ E + 6Fr^2/a^2\ )\cos 2\theta\ ] \qquad \text{A11.h)}$$

$$u_r^{i^1} = (\sigma_0/8\mu^i)[\ D(\kappa^i-1)r - \{\ 2Er - F(\kappa^i-3)r^3/a^2\ \}\cos 2\theta\ ] \qquad \text{A11.i)}$$

$$u_\theta^{i^1} = (\sigma_0/8\mu^i)[\ 2Er + F(\kappa^i+3)r^3/a^2\ ]\sin 2\theta. \qquad \text{A11.j)}$$

In order to determine the constants in Eq A11), appropriate boundary conditions for the composite system should be set up at the interface, assuming perfect interfacial bonding. Since the stresses an the displacements have to be continuous at the interface, the boundary conditions at matrix-inclusion interface (r=a) are

$$\sigma_{rr}^{m^1}(a,\theta) = \sigma_{rr}^{i^1}(a,\theta) \qquad \text{A12.a)}$$

$$\sigma_{r\theta}^{m^1}(a,\theta) = \sigma_{r\theta}^{i^1}(a,\theta) \qquad \text{A12.b)}$$

$$u_r^{m^1}(a,\theta) = u_r^{i^1}(a,\theta) \qquad \text{A12.c)}$$

$$u_\theta^{m^1}(a,\theta) = u_\theta^{i^1}(a,\theta) \qquad \text{A12.d)}$$

where the superscript 'm^1' and 'i^1' denote matrix and inclusion under applied uniaxial loading, respectively. From Eq A11) and A12), the following equations, which have to be solved for unknown constants, are obtained:

i) $\sigma_{rr}^{m1}(a,\theta) = \sigma_{rr}^{i1}(a,\theta)$;

$$1 + A - D = 0 \qquad \text{A13.a)}$$

$$1 - 2B - 3C + E = 0 \qquad \text{A13.b)}$$

ii) $\sigma_{r\theta}^{m1}(a,\theta) = \sigma_{r\theta}^{i1}(a,\theta)$;

$$1 + B + 3C + E + 3F = 0 \qquad \text{A13.c)}$$

iii) $u_r^{m1}(a,\theta) = u_r^{i1}(a,\theta)$;

$$(\kappa^m-1) - 2A - \delta D(\kappa^i-1) = 0 \qquad \text{A13.d)}$$

$$2 + B(\kappa^m+1) + 2C + \delta[\ 2E+F(3-\kappa^i)\ ] = 0 \qquad \text{A13.e)}$$

iv) $u_\theta^{m1}(a,\theta) = u_\theta^{i1}(a,\theta)$;

$$-2 - B(\kappa^m-1) + 2C - \delta[\ 2E+F(3-\kappa^i)\ ] = 0 \qquad \text{A13.f)}$$

where $\delta = \mu^m/\mu^i$.

The unknown constants are determined as

$$\left.\begin{aligned} A &= [\ (\kappa^m-1)-\delta(\kappa^i-1)\ ]/[\ \delta(\kappa^i-1)+2\ ] \\ B &= 2\ (\ \delta-1\ )/(\ \delta+\kappa^m\ ) \\ C &= (\ 1-\delta\ )/(\ \delta+\kappa^m\ ) \\ D &= [\ \kappa^m+1\ ]/[\ \delta(\kappa^i-1)+2\ ] \\ E &= -(\ \kappa^m+1\ )/(\ \delta+\kappa^m\ ) \\ F &= 0. \end{aligned}\right\} \qquad \text{A14)}$$

A.III.2 Large plate having a circular inclusion with different thermal expansion coefficient

If the system involves inelastic strain caused by thermal expansion coefficient mismatch, it will produce inelastic stress on the body. Since such a situation is axisymmetric, the Airy stress function should be a linear function of the polar coordinate of r;

$$\Phi^2 = L\{ r^2, \log r, r^2 \log r \}$$
$$= Gr^2 + H\log r + Ir^2 \log r \qquad \text{A15)}$$

,where Φ^2 is the Airy stress function due to thermal expansion coefficient mismatch. By considering the stress components evaluated from Eq A5), the stress function for the matrix (Φ^{m2}) and the inclusion (Φ^{i2}) can be determined as:

$$\Phi^{m2}(r,\theta) = H\log r \qquad \text{A16)}$$

$$\Phi^{i2}(r,\theta) = Gr^2. \qquad \text{A17)}$$

Using Eq A5), A9), and A10), the corresponding stress and displacement components for Eqs A16) and A17) can be obtained as:

$$\sigma_{rr}^{m2} = -\sigma_{\theta\theta}^{m2} = H/r^2 \qquad \text{A18.a)}$$

$$\sigma_{rr}^{i2} = \sigma_{\theta\theta}^{i2} = 2G \qquad \text{A18.b)}$$

$$u_r^{m2} = -H/(2\mu^m r) \qquad \text{A18.c)}$$

$$u_r^{i2} = u_r^2 + G(\kappa^i - 1)r/2\mu^i \qquad \text{A18.d)}$$

,where u_r^{m2} and u_r^{i2} are the radial displacements of the matrix and the inclusion caused by inelastic strain due to thermal expansion coefficient mismatch. Each displacement components can be evaluated from the Hooke's law given in Eq A9). Since the normal strain due to thermal expansion, $e_{rr}^* = e_{\theta\theta}^* = e_{zz}^* = e$ and shear components (e_{ij}^*) are 0, the stresses under free thermal expansion condition will also be 0. Thus, the Hooke's law can be reduced into

$$e_{rr} = \frac{1}{2\mu}\left[\sigma_{rr} - \frac{(3-\kappa)}{4}(\sigma_{rr} + \sigma_{\theta\theta}) \right] + e_{rr}^* + \eta e_{zz}^*$$

$$= e_{rr}^* + \eta e_{zz}^*$$

$$= (1+\eta)e = e^*. \qquad \text{A19.a)}$$

,where η is ν for plane strain and η is zero for plane stress.
Thus, the radial displacement, u_r^2, due to free thermal expansion becomes

$$u_r^2 = ae^*$$
$$= a(1+\eta)e$$
$$= a(1+\eta)\Delta\alpha\Delta T$$
$$= a(1+\eta)(\alpha^i-\alpha^m)(T_f-T_i) \qquad \text{A19.b)}$$

,where a = distance from the center of the circular inclusion

α^i, α^m = thermal expansion coefficient of the inclusion and matrix, respectively, and

T_f, T_i = final and initial temperature, respectively.

In order to determine the unknown constant in Φ^{m2} and Φ^{i2}, appropriate boundary conditions should be set up. From the continuity of stress and displacement at the matrix/inclusion interface,

$$\sigma_{rr}^{m2}(a,\theta) = \sigma_{rr}^{i2}(a,\theta) \qquad \text{A20.a)}$$

$$u_r^{m2}(a,\theta) = u_r^{i2}(a,\theta). \qquad \text{A20.b)}$$

Solving Eq A20.a) for the unknown constants in Φ^2 will give

$$G = -P/2 \qquad \text{A21.a)}$$

$$H = -Pa^2 \qquad \text{A21.b)}$$

,where -P is the compressive stress, caused by thermal expansion mismatch, acting on the matrix/inclusion interface. Thus, Eqs A18.c) and A18.d) become

$$u_r^{m2}(a,\theta) = \text{expansion due to } -P$$

$$= -Pa^2(-1/a)/2\mu^m \qquad \text{A22.a)}$$

$$u_r^{i2}(a,\theta) = (\text{thermal expansion}) + (\text{shrink due to } -P)$$

$$= ae^* - P(\kappa^i-1)a/4\mu^i. \qquad \text{A22.b)}$$

Solving Eq A19.b) for P using Eq A21):

$$P = [\ 4\mu^m\mu^i(1+\eta)\Delta\alpha\Delta T\ ]/[\ 2\mu^i+(\kappa^i-1)\mu^m\ ]. \qquad \text{A23)}$$

Since the exact stress function Φ^{m2} and Φ^{i2} are obtained by substituting Eq A21) to Eq A16) and A17), stress and displacement components for the matrix and inclusion can also be determined:

$$\sigma_{rr}^{m2}(r,\theta) = -Pa^2/r^2 \qquad \text{A24.a)}$$

$$\sigma_{\theta\theta}^{m2}(r,\theta) = Pa^2/r^2 \qquad \text{A24.b)}$$

$$\sigma_{r\theta}^{m2}(r,\theta) = 0 \qquad \text{A24.c)}$$

$$u_r^{m2}(r,\theta) = Pa^2/(2\mu^m r) \qquad \text{A24.d)}$$

$$u_\theta^{m2}(r,\theta) = 0 \qquad \text{A24.e)}$$

$$\sigma_{rr}^{i2}(r,\theta) = -P \qquad \text{A24.f)}$$

$$\sigma_{\theta\theta}^{i2}(r,\theta) = -P \qquad \text{A24.g)}$$

$$\sigma_{r\theta}^{i2}(r,\theta) = 0 \qquad \text{A24.h)}$$

$$u_r^{i2}(r,\theta) = \{\ -P(\kappa^i-1)r/4\mu^i\ \} + \{\ r(1+\eta)\Delta\alpha\Delta T\ \} \qquad \text{A24.i)}$$

$$u_\theta^{i2}(r,\theta) = 0. \qquad \text{A24.j)}$$

APPENDIX IV.

EFFECT OF COLD ROLLING AND ANNEALING ON THE ANNEALING TEXTURES AND ITS INFLUENCES ON THE YOUNG'S MODULUS OF Al ALLOYS

The crystallographic orientations on the rolling plane can be described using the inverse pole figures obtained by the X-ray diffraction.

A) Textures on the rolling plane along the longitudinal direction

X-ray diffraction carried out on the rolling surface of the as-extruded composite showed strong <100> and less strong <331> textures along the extruded (longitudinal) direction. However, with increasing reduction in cold rolling, <331> in the as-extruded composite was found to shift to <110>, while <100> remains almost the same. As a result, in case of the cold rolled and T6 treated composites, relatively strong <110>, as well as strong <331>, was observed on the rolling plane along the longitudinal direction as shown in Fig.1.

B) Textures on the rolling plane along the transverse direction

In case of the as-extruded composite, strong <100> and less strong <221> textures were observed along the transverse direction. With increasing reduction in cold rolling, <221> observed in the as-extruded composite was found to shift into <111>, while <100> remains almost the same. As a result, In case of the cold rolled and T6 treated composites, relatively strong <111> in addition to strong <110> was

observed on the rolling plane along the transverse direction as shown in Fig.1.

Similar texture patterns were observed from the hot rolled composites, although the intensities of the textures in the hot rolled composite are slightly weaker than those of the cold rolled one.

The significance of the appearance of <110> and <111> textures can be understood by considering the differences in the Young's moduli of an Al single crystal along these directions as shown in the Table, indicating that the Young's moduli measured along <110> and <111> are larger that those along <100>.

As an example, the effect of the appearance of <110> texture on the variations in the Young's modulus is illustrated in Fig.2, showing the increase in the Young's modulus of the cold rolled and T6 treated 6061 Al alloy (along the longitudinal direction) as a function of reduction ratio. From the result of the non-linear regression carried on the data points, the variation of the modulus as a function of the reduction ratio has the form of $y = \alpha e^{\beta X} + \eta$, where α, β, and η are the experimental constants.

Table 1. Young's modulus of Al single crystal along various crystallographic directions.

Crystallographic direction	<100>	<110>	<111>
Young's modulus (GPa)	63.7	72.6	76.1
Nomalized modulus	1.00	1.14	1.195

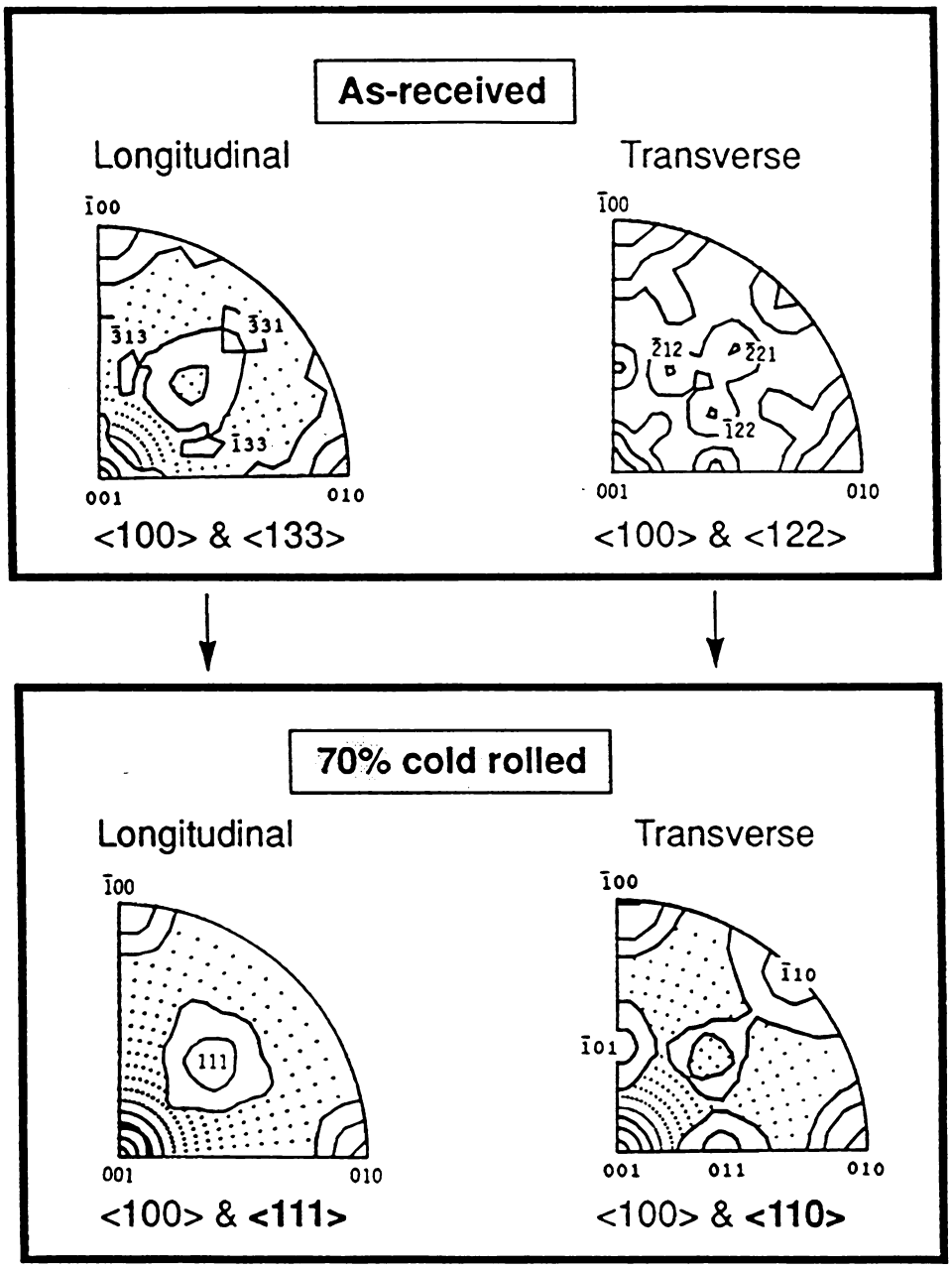

Fig.1 Inverse pole figures of the as-reveived composite and the 70% cold rolled and T6 treated composite along the longiudinal and the transverse directions.

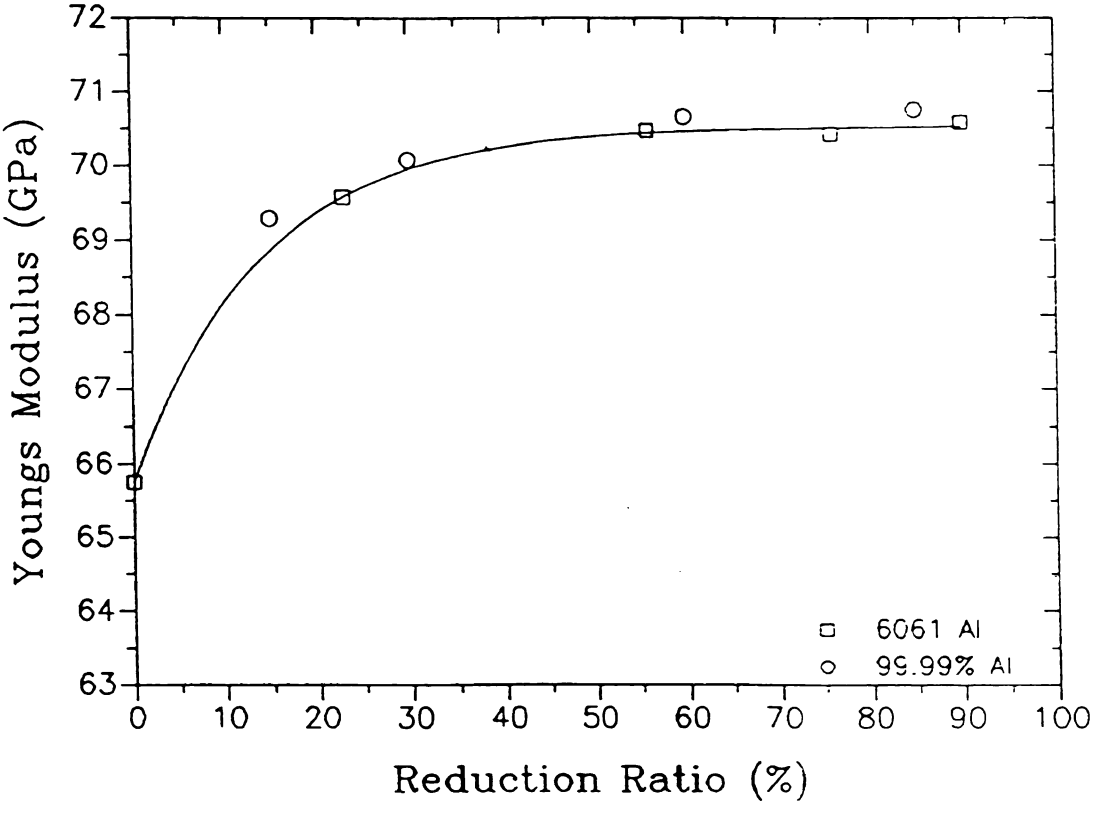

Fig.2 Variations in the Young's modulus of the cold rolled and annealed a) pure Al (Kosta, 1938) and b) 6061 Al alloy as a function of the reduction ratio.

APPENDIX V.

THE MAXIMUM FIBER STRESS AS A FUNCTION OF FIBER DIMENSIONS

In short fiber reinforced composite, external load applied to the composite is transferred to the fibers through the fiber ends as well as the side surface of the fiber. As a result, the end effects, which normally can be neglected in case of continuous fiber reinforced composites, cannot be ignored since the stress along the fiber length is a function of location and the fiber dimensions. The maximum stress $[\sigma_f(\ell/2)]$ along the length of a fiber occurs at half the fiber length upon a longitudinal loading. $\sigma_f(\ell/2)$ can be obtained by considering the equilibrium of forces acting on an element of the fiber as shown in Fig.1. The derivations used in this paper is analogous to the earlier study by Dow [11].

In case of the longitudinal loading, the force equilibrium of an infinitesimal length, dy, requires

$$(\sigma_f + d\sigma_f)\ t\omega = \sigma_f\ t\omega + \tau\ (\ 2t\ dy + 2\omega\ dy\ ) \qquad (A1)$$

$$\text{or} \quad \frac{d\sigma_f}{dy} = \frac{2\tau\ (\ t + \omega\ )}{t\omega} \qquad (A2)$$

where σ_f is the fiber stress along the length, τ is the shear stress acting on the fiber/matrix interface, ω is the width of the fiber perpendicular to the longitudinal loading, and t is the thickness

perpendicular to the rolling direction. Integration of Eq(A2) from the fiber end (ℓ=0) to the middle of the fiber (ℓ/2) yields

$$\sigma_f(\frac{\ell}{2}) = \sigma_f(0) + \frac{2\ (\ t + \omega\ )}{t\omega} \int_0^{(\ell/2)} \tau\ dy \qquad \text{(A3)}$$

where $\sigma_f(0)$ is the stress at the fiber end, which is usually taken to be zero. Assuming 2τ to be the matrix yield strength(σ_m), Eq(A3) can be rewritten as

$$\sigma_f(\max) = \sigma_f(\frac{\ell}{2}) = \frac{\ell}{2}\ (\ \frac{1}{\omega} + \frac{1}{t}\ )\ \sigma_m. \qquad \text{(A4)}$$

Similarly, for the transverse loading, the force equilibrium of an infinitesimal width, dx, requires

$$(\ \sigma_f + d\sigma_f)\ t\ell = \sigma_f\ t\ell + \tau\ (\ 2t\ dx + 2\ell\ dx\ ) \qquad \text{(A5)}$$

$$\text{or} \quad \frac{d\sigma_f}{dx} = \frac{2\tau\ (\ t + \ell\ )}{t\ell}\ . \qquad \text{(A6)}$$

where σ_f is the fiber stress along the width. Using analogous assumptions and procedures, the maximum stress along the width can be obtained as

$$\sigma_f(\max) = \sigma_f(\frac{\omega}{2}) = \frac{\omega}{2}\ (\ \frac{1}{\ell} + \frac{1}{t}\ )\ \sigma_m\ . \qquad \text{(A7)}$$

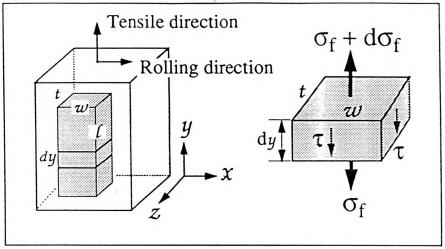

(a)

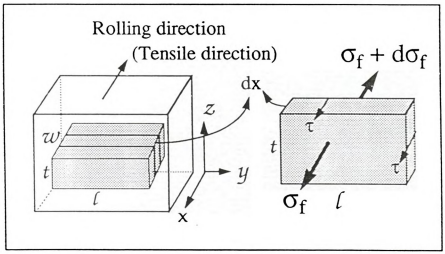

(b)

Fig.1 Schematics illustrating the composite loaded along a) the longitudinal and b) the transverse directions.